

ISSN en trámite



# Geofísica Internacional

Revista Trimestral Publicada por el Instituto de Geofísica de la  
Universidad Nacional Autónoma de México



México

Volume 54 Number 2  
April - June  
2015

# — Geofísica Internacional —

Dr. Arturo Iglesias Mendoza  
**Director of Instituto de Geofísica**

Dra. Tereza Cavazos  
**President of Unión Geofísica Mexicana**

## Editor Chief

Dr. Servando De la Cruz-Reyna  
Instituto de Geofísica, UNAM  
[sdelacrr@geofisica.unam.mx](mailto:sdelacrr@geofisica.unam.mx)

## Technical Editor

Mtra. Andrea Rostan Robledo  
Instituto de Geofísica, UNAM  
[arostan@igeofisica.unam.mx](mailto:arostan@igeofisica.unam.mx)

## Editorial Board

Donald Bruce Dingwell  
Earth and Environment  
Ludwig Maximilian University of Munich,  
Germany

Eric Desmond Barton  
Departamento de Oceanografía  
Instituto de Investigaciones Marinas, Spain

Jorge Clavero  
Amawta Consultores, Chile

Gerhardt Jentzsch  
Institut für Geowissenschaften  
Friedrich-Schiller-Universität Jena, Germany

Peter Malischewsky  
Institut für Geowissenschaften  
Friedrich-Schiller-Universität Jena, Germany

François Michaud  
Géosciences Azur  
Université Pierre et Marie Curie, France

Olga Borisovna Popovicheva  
Scobeltzine Institute of Nuclear Physics  
Moscow State University, Rusia

Jaime Pous  
Facultad de Geología  
Universidad de Barcelona, Spain

Joaquín Rui  
UA Science  
University of Arizona, United States

Angelos Vourlidas  
Solar Physics Branch  
NASA Goddard Space Flight Center, United States

Théophile Ndougsa Mbarga  
Department of Physics  
University of Yaounde I, Cameroon

Associate Editors  
José Agustín García Reynoso  
Atmospheric Science Centro de Ciencias de la  
Atmósfera UNAM, Mexico

Tereza Cavazos  
Atmospheric Science  
Departamento de Oceanografía Física CICESE,  
Mexico

Dante Jaime Morán-Zenteno  
Geochemistry  
Instituto de Geología, UNAM, Mexico

Margarita López  
Geochemistry  
Instituto de Geología UNAM, Mexico

Avto Gogichaisvili  
Geomagnetism And Paleomagnetism  
Instituto de Geofísica UNAM, Mexico

Jaime Urrutia-Fucugauchi  
Geomagnetism And Paleomagnetism  
Instituto de Geofísica, UNAM, Mexico

Felipe I. Arreguín Cortés  
Hydrology  
Instituto Mexicano de Tecnología del Agua IMTA,  
Mexico

William Lee Bandy  
Marine Geology And Geophysics  
Instituto de Geofísica UNAM, Mexico

Fabian García-Nocetti  
Mathematical And Computational  
Modeling  
Instituto de Investigaciones en Matemáticas  
Aplicadas y en Sistemas UNAM, Mexico

Graciela Herrera-Zamarrón  
Mathematical Modeling  
Instituto de Geofísica, UNAM, Mexico

Ismael Herrera Revilla  
Mathematical And Computational  
Modeling  
Instituto de Geofísica UNAM, Mexico

Rene Chávez Segura  
Near-Surface Geophysics  
Instituto de Geofísica UNAM, Mexico

Juan García-Abdeslem  
Near-Surface Geophysics  
División de Ciencias de la Tierra CICESE, Mexico

Alec Torres-Freyermuth  
Oceanography  
Instituto de Ingeniería, UNAM, Mexico

Jorge Zavala Hidalgo  
Oceanography  
Centro de Ciencias de la Atmósfera UNAM,  
Mexico

Shri Krishna Singh  
Seismology  
Instituto de Geofísica, UNAM, Mexico

Xyoli Pérez-Campos  
Seismology  
Servicio Sismológico Nacional, UNAM, Mexico

Blanca Mendoza Ortega  
Space Physics  
Centro de Ciencias de la Atmósfera, UNAM,  
Mexico

Inez Staciari Batista  
Space Physics  
Pesquisador Senior Instituto Nacional de Pesquisas  
Espaciais, Brazil

Roberto Carniel  
Volcanology  
Laboratorio di misure e trattamento dei segnali  
DPIA - Università di Udine, Italy

Miguel Moctezuma-Flores  
Satellite Geophysics  
Facultad de Ingeniería, UNAM, Mexico

## Assistance

Elizabeth Morales Hernández,  
Management  
[eliedit@igeofisica.unam.mx](mailto:eliedit@igeofisica.unam.mx)



**GEOFÍSICA INTERNACIONAL**, Año 54, Vol. 54, Núm. 2, abril - junio de 2015 es una publicación trimestral, editada por la Universidad Nacional Autónoma de México, Ciudad Universitaria, Alcaldía Coyoacán, C.P. 04150, Ciudad de México, a través del Instituto de Geofísica, Circuito de la Investigación Científica s/n, Ciudad Universitaria, Alcaldía Coyoacán, C.P. 04150, Ciudad de México, Tel. (55)56 22 41 15. URL: <http://revistagi.geofisica.unam.mx>, correo electrónico: [revistagi@igeofisica.unam.mx](mailto:revistagi@igeofisica.unam.mx). Editora responsable: Andrea Rostan Robledo. Certificado de Reserva de Derechos al uso Exclusivo del Título: 04-2022-081610251200-102, ISSN: en trámite, otorgados por el Instituto Nacional del Derecho de Autor (INDAUTOR). Responsable de la última actualización Saúl Armendáriz Sánchez, Editor Técnico. Fecha de la última modificación: 31 de marzo 2015, Circuito de la Investigación Científica s/n, Ciudad Universitaria, Alcaldía Coyoacán, C.P. 04150, Ciudad de México.

El contenido de los artículos es responsabilidad de los autores y no refleja el punto de vista de los árbitros, del Editor o de la UNAM. Se autoriza la reproducción total o parcial de los textos siempre y cuando se cite la fuente completa y la dirección electrónica de la publicación.



Esta obra está bajo una Licencia Creative Commons Atribución-NoComercial-SinDerivadas 4.0 Internacional.

## Contents

Reconstruction of glacier area on Citlaltépetl volcano, 1958 and implications for Mexico's deglaciation rates.

**Jorge Cortés-Ramos, Hugo Delgado-Granados**

111

New Paleomagnetic results and evidence for a geomagnetic field excursion during the pleistocene-holocene transition at Pichincha province, Ecuador.

**Hugo G. Nami**

127

Source Model of the October 9, 1995 Jalisco-Colima Tsunami as constrained by field survey reports, and on the numerical simulation of the tsunami.

**Elizabeth Trejo-Gómez, Modesto Ortiz, Francisco Javier Núñez-Cornú**

149

The Chromospheric Solar Millimeter-wave Cavity; a Common Property in the Semi-empirical Models.

**Víctor de la Luz, Miguel Chavez, Emanuele Bertone**

161

Paleomagnetic Pole Positions and Geomagnetic Secular Variation from the Cretaceous Ponta Grossa Dike Swarm (Brazil).

**Miguel Cervantes Solano, Avto Goguitchaichvili, Mabel Mena, Luis Alva-Valdivia, Juan Morales Contreras, Ruben Cejudo Ruiz, Héctor López Loera, Ana María Soler, Jaime Urrutia-Fucugauchi**

167

Modeling sea-level change, inundation scenarios, and their effect on the Colola Beach Reserve - a nesting-habitat of the black sea turtle, Michoacán, Mexico.

**Yuritzi Calvillo García, María Teresa Ramírez-Herrera, Carlos Delgado-Trejo, Gabriel Legorreta-Paulin, Néstor Corona**

179

Early warning from seismic ionospheric anomaly of the 24 May 2014,  $M_w = 6.4$  Aegean-Sea earthquake: two-dimensional principal component analysis (2DPCA).

**Jyh-Woei lin**

## Reconstruction of glacier area on Citlaltépetl volcano, 1958 and implications for Mexico's deglaciation rates

Jorge Cortés-Ramos\* and Hugo Delgado-Granados

Received: June 27, 2013; accepted: August 12, 2014; published on line: March 31, 2015

### Resumen

En este trabajo se llevó a cabo un análisis detallado de las mediciones hechas en el Glaciar Norte del volcán Citlaltépetl en 1958 y documentadas en el trabajo de Lorenzo de 1964. Se encontraron una serie de inconsistencias en la cartografía de los glaciares del Citlaltépetl, las cuales son más evidentes al observar los resultados reportados en la misma publicación para los volcanes Popocatepetl e Iztaccíhuatl. A partir de estas inconsistencias se concluyó que la delimitación hecha para los glaciares del Citlaltépetl era cartográficamente incorrecta y, por tanto, los resultados exageraban las verdaderas dimensiones de estos glaciares para el año 1958. En este trabajo se describe la metodología seguida para la reconstrucción del Glaciar Norte de 1958. Así, se obtuvo un nuevo valor para el área glacial total del Citlaltépetl. Esta reconstrucción respeta los límites del frente glacial medidos por Lorenzo (1964), tal como se detalla de forma precisa en la narración de su trabajo de campo. Finalmente, se discute acerca del retroceso glacial en el volcán Citlaltépetl con base en el nuevo valor obtenido para el área del Glaciar Norte (2.04 km<sup>2</sup>). El retroceso glacial resultó ser comparable con las áreas medidas por Lorenzo (1964) en los volcanes Iztaccíhuatl y Popocatepetl, las cuales ya han sido corroboradas en la literatura.

Palabras clave: Citlaltépetl, glaciar, cartografía, fotogrametría, ortofotos, corrección geográfica.

### Abstract

In this study, a detailed analysis of the measurements made on Glaciar Norte of Citlaltépetl volcano in 1958 by Lorenzo (1964) is conducted. A series of inconsistencies are evident when comparing the dimensions of Citlaltépetl volcano's glaciers and those of the glaciers on Popocatepetl and Iztaccíhuatl volcanoes. From these inconsistencies it was concluded that the delimitation of Citlaltépetl's glaciers was wrong and the values exaggerated the true conditions of these ice bodies for 1958. In this paper we explain the methodology applied for the reconstruction of Glaciar Norte in 1958. From this reconstruction, a new more realistic value for the glaciated area on Citlaltépetl was obtained. The reconstruction respects the glacier front boundaries reported by Lorenzo (1964), which are precisely detailed at the narrative of his fieldwork. Finally, this paper discusses the glacial shrinkage on Citlaltépetl volcano based on the new value obtained for the area of Glaciar Norte (2.04 km<sup>2</sup>). This value is of a magnitude comparable to the glacial areas of Iztaccíhuatl and Popocatepetl volcanoes that were also measured and reported by Lorenzo (1964) and confirmed in the literature.

Key words: Citlaltépetl, glacier, cartography, photogrammetry, ortho-photos, geographic correction.

---

J. Cortés-Ramos\*  
H. Delgado-Granados  
Departamento de Vulcanología  
Instituto de Geofísica  
Universidad Nacional Autónoma de México  
Ciudad Universitaria  
Delegación Coyoacán, 04510  
México D.F., México  
\*Corresponding author: [jorge@geofisica.unam.mx](mailto:jorge@geofisica.unam.mx)

## Introduction

In mid-XXth century, Mexican glaciers were located on top of the three highest mountains of the country: Citlaltépetl or Pico de Orizaba at 5,675 m (meters above sea level; 9 glaciers); Iztaccíhuatl at 5,230 m (12 glaciers) and Popocatepetl at 5,465 m (3 glaciers) (Lorenzo, 1964). The climatic conditions in central Mexico through the year above 4500 m allowed the existence of these glaciers. However, in 2001 the glacial system on Popocatepetl volcano was considered extinct as a result of the eruptive activity that began on 1994 (Julio Miranda and Delgado Granados, 2003; Delgado Granados *et al.*, 2007). The glaciers on Iztaccíhuatl and Citlaltépetl volcanoes have also been retreating and some of them already disappeared (Schneider *et al.*, 2008).

Lorenzo (1964) made the first report on all Mexican glacial systems for the International Geophysical Year (IGY). He mapped and made a detailed description of the geometry of the limits and area of those glaciers. The existing circumstances in 1958 (execution year of these studies) represented a real challenge to obtaining the glacial geometry and dimensions of the 24 glaciers in Mexico. This pioneering work is considered a landmark in Mexican glaciology, due to the report of: geographic position, elevation, name, approximate area, photographic catalogue, and glaciological and meteorological data. This glaciological inventory was accomplished in a short time and the best possible way taking into account the limited experience for carrying out such studies, the limited availability of equipment and the shortage of funds (Lorenzo, 1964). Also, it is important to notice that meteorological conditions on 1958 delayed and difficult the fieldwork.

The glaciated areas reported by Lorenzo (1964) for Citlaltépetl, Popocatepetl and Iztaccíhuatl volcanoes made in 1958, were the bases for estimating glacier shrinkage.

In this study, the methodology employed by Lorenzo (1964) is reviewed. This revision was mandatory after finding inconsistencies in the measured dimensions of Citlaltépetl volcano's glaciers. The dimensions of glaciers obtained by Lorenzo (1964) during contemporaneous glaciological work at Iztaccíhuatl and Popocatepetl volcanoes suggested that the map of Citlaltépetl volcano's glaciers was not accurate. From this revision it was possible to correct his maps and reconstruct the glaciated area on Citlaltépetl. This reconstruction was based on a 1975 aerial photo of Citlaltépetl

(INEGI, 1975), orthorectified for this work; a 1:20,000 DEM from SIGSA (2006), and the photographic catalogue published by Lorenzo (1964).

## The 1958 glaciological campaign

### *The inventory of Citlaltépetl's glaciers*

Citlaltépetl is located in the eastern part of the Trans-Mexican volcanic belt, 100 km from the coast of the Gulf of Mexico, 200 km from Mexico City (Figure 1).

From Lorenzo's work in 1958, glaciers on Citlaltépetl volcano were recognized as the largest glacial system in Mexico. Lorenzo (1964) described Glaciar Norte at the top of the volcano comprising 7 glacier tongues facing north, northwest and west. On the eastern flank described another glacial system called Glaciar Oriental, an independent system, which is still present today.

The methodology followed in 1958 was based on the use of cartographic material, aerial photographs, topographic maps, altimetry data, thermometers, and a Brunton compass (Lorenzo, 1964). The cartography consisted in a map at a scale of 1:50,000 made by Estudios y Proyectos, A.C. and for this site, aerial photographs were acquired by the Papaloapan Commission in 1955. The altimetry was determined with Thommen pocket altimeters with a range up to 6000 m and divisions every 10 m. These altimeters were used together with tables of corrections as established by the Mexican Meteorological Service (Lorenzo, 1964). Temperature corrections for altitude were made with a thermometer graduated to the nearest degree centigrade. All readings were taken at the same points during the campaign, in order to ensure the correctness within the limits of the instruments (Lorenzo, 1964).

Regarding the aerial photographs, Lorenzo (1964, page 92) stated: "*the photographs were not of first importance, due to their age, but they were used as a guide rather than as direct evidence.*" It is assumed that photogrammetry was not the main tool used by Lorenzo (1964) to map the glacier. After identification of glaciated areas on the aerial photographs, the altitude of the glaciers and compass directions of their boundaries were measured in the field. The ice limits were annotated and sketched by Lorenzo (1964, page 92) mentioning: "*It is our belief that in spite of the scarcity of technical aid, the errors will not be found too great.*"

The main body of Glaciar Norte (beginning at 5,650 m and ending 4,640 m) resulted with an area of ca. 9 km<sup>2</sup>, divided into different glacial tongues (Figure 2). Lorenzo (1964) used the term glacier to distinguish every tongue of Glaciar Norte, a fact that sometimes derived in confusion. The identified glaciers and the altitude of their lowest limits are enlisted following the published nomenclature:

Chichimeco glacier, 4,740 m.  
 Jamapa glacier, 4,640 m.  
 Toro glacier, 4,930 m.  
 Barba glacier, 5,090 m.  
 Noroccidental glacier, 4,920 m.  
 Occidental glacier, 4,980 m.  
 Suroccidental glacier, 4,980 m.  
 Oriental glacier, 5,070 m (separated from Glaciar Norte with ca. 420,000 m<sup>2</sup>).

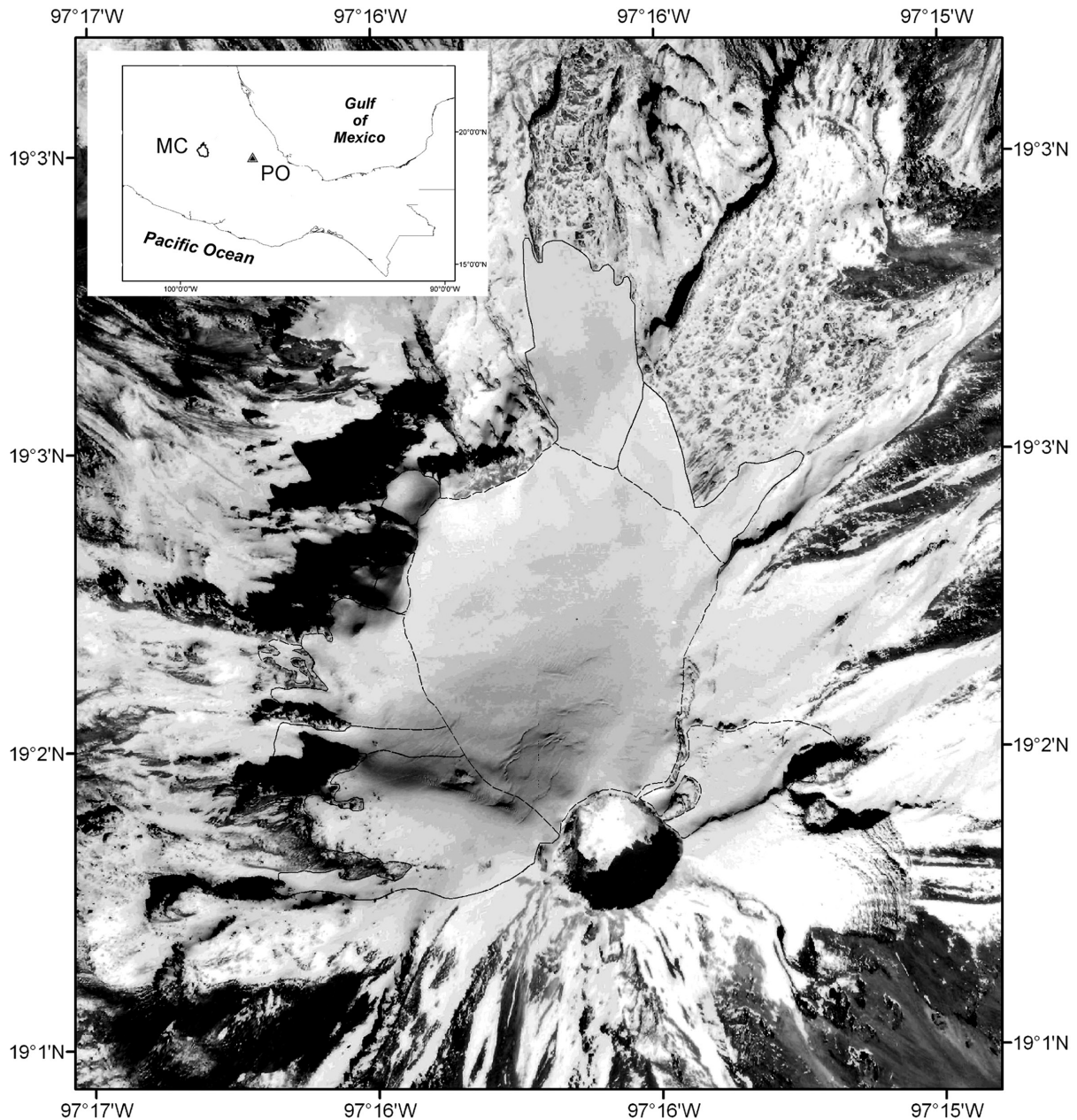


**Figure 1.** Location of Citlaltépetl volcano (PO) and Mexico City (MC). The orthophoto was obtained from an aerial-photograph of INEGI (1975).

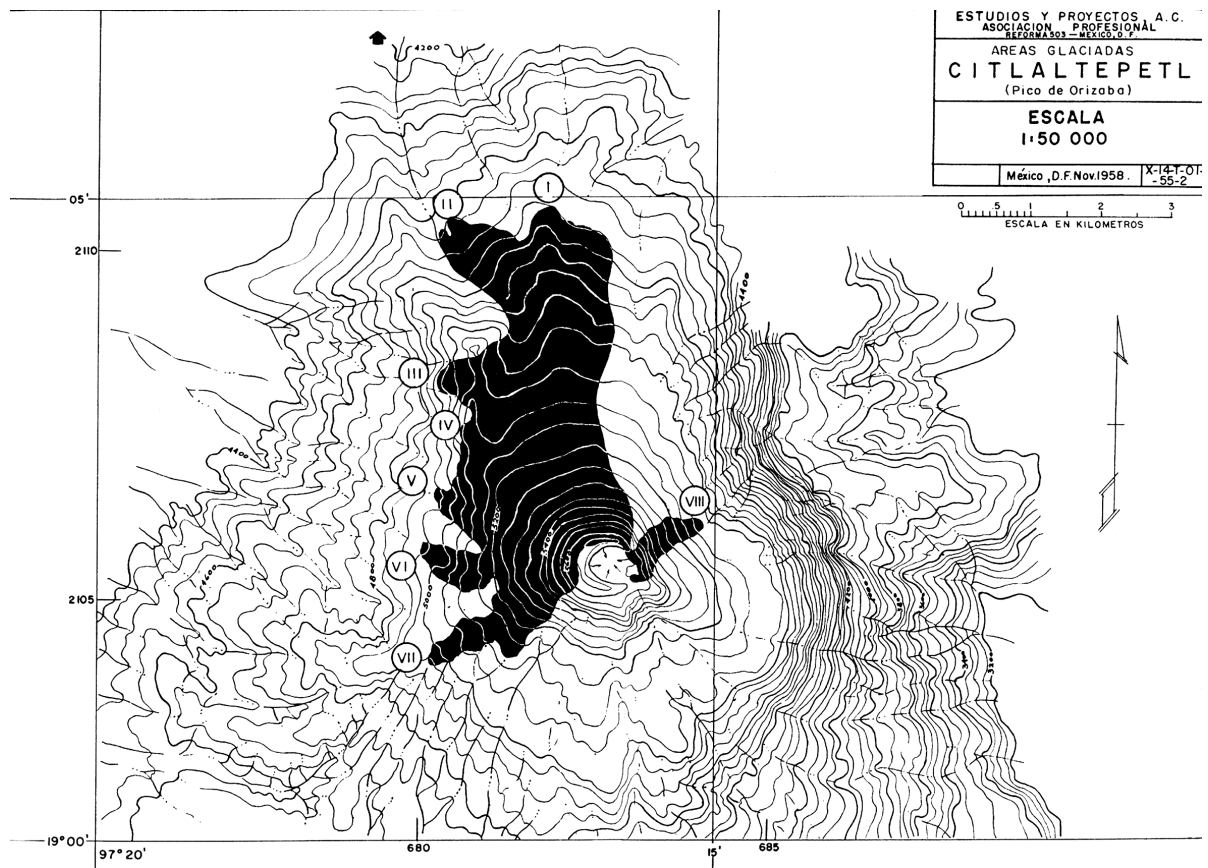


**Figure 2.** Topographic map of Citlaltépetl volcano's glaciers in 1958 (taken from Lorenzo, 1964). Roman letters indicate the glacial tongues of Glaciar Norte and a separate glacier: I) Chichimeco; II) Jamapa; III) Toro; IV) Barba; V) Noroccidental; VI) Occidental; VII) Suroccidental; and Glaciar Oriental (VIII) on the eastern flank of the volcano.

From these data, the glacial area of Citlaltépetl was considered the largest in the tropical zone of the northern hemisphere.

*Glacial inventories of Popocatépetl and Iztaccíhuatl volcanoes.*

In order to test the reported cartographic work at Citlaltépetl volcano for inconsistencies, it is relevant to review the work made on these two volcanoes too.

These mountains are located ~50 km (Popocatépetl) and ~35 km (Iztaccíhuatl) southeast and east of Mexico City. White (1954; 1956) conducted the first studies about the glaciers on those volcanoes. His studies, together with aerial photographs, were the main source of information for Lorenzo to develop the glacial inventory of these mountains, since the fieldwork was delayed due to bad weather at that time. Lorenzo (1964) accepted that the data must therefore had a "certain margin of error".

Cartographic material employed by Lorenzo (1964) included: aerial photographs obtained in 1945 by the Compañía Mexicana de Aerofoto, S.A., and two topographic maps (1:20,000) made by the Compañía Hidroeléctrica de los Volcanes. The altimetry, compass directions and temperature measurements were the same as described above.

At Popocatépetl, Lorenzo (1964) described Ventorrillo, Noroccidental and Norte glaciers on the north flank of the volcano. In spite of difficulties, the altitude measurements of the glacier boundaries were accurate enough for that work ( $\pm 20$  m). Ventorrillo glacier resulted with an extension of ca. 435,000 m<sup>2</sup> and its lowest front at 4,690 m. The Noroccidental glacier was west of Ventorrillo glacier, separated from it at 5,300 m, with an area of ~95,000 m<sup>2</sup> and front at 5,015 m. Norte glacier was east of Ventorrillo with an area of ~190,000 m<sup>2</sup> and a front at 4,840 m. The total glaciated area at Popocatépetl volcano in 1954 was of ~720,000 m<sup>2</sup>.

The glaciers on Iztaccíhuatl and their areas were described follows (Lorenzo, 1964): Cuello (ca. 20,000 m<sup>2</sup>); Ayolotepito (ca. 300,000 m<sup>2</sup>); Nororiental (ca. 110,000 m<sup>2</sup>); Pecho (ca. 75,000 m<sup>2</sup>); Centro-oriente (ca. 140,000 m<sup>2</sup>); Ayoloco (ca. 285,000 m<sup>2</sup>); Suroriental (ca. 80,000 m<sup>2</sup>); Atzintli (ca. 120,000 m<sup>2</sup>) and San Agustín (ca. 30,000 m<sup>2</sup>). All of these glaciers covered an area of ca. 1.2 km<sup>2</sup>. The lowest glacial front determined for those glaciers was measured at Ayoloco glacier at an altitude of 4,668 m in 1958.

It is noteworthy to mention that the mean glacial area for these two volcanoes was ~1 km<sup>2</sup> for 1954 with a mean minimal altitude of 4,680 m.

*Inconsistencies of reported glaciated areas of Citlaltépetl Volcano.*

A series of inconsistencies are found when comparing the shrinkage at the three glacial systems. Taking into account the studies made by Delgado Granados *et al.* (2007) and Schneider *et al.* (2008), the glaciated areas on Popocatépetl and Iztaccíhuatl in 1982 were 0.559 km<sup>2</sup> and 0.863 km<sup>2</sup>, respectively (see Table 1). These values represent a glacial shrinkage of 22% on Popocatépetl and 28% on Iztaccíhuatl as compared with the areas reported by Lorenzo (1964). This represents a similar glacial shrinkage on both glacier systems between 1958 and 1982 (24 years). In contrast, between 1958 and 2001 the glaciers on Citlaltépetl retreated about 90% in 43 years (Cortés Ramos and Delgado Granados, 2013); this is also considering the area reported by Lorenzo (1964). This value led to think about the differences between the glacial shrinkage on Popocatépetl and Iztaccíhuatl in comparison with Citlaltépetl. Are the glaciers on Citlaltépetl unique? Or, is the glaciated area reported by Lorenzo (1964) wrong? The first question lead to assume that climate on Citlaltépetl is completely different than climate dominating on Popocatépetl and Iztaccíhuatl, or that the weather conditions in the vicinity of Citlaltépetl have changed more strongly in the same period of time from the conditions at the Popocatépetl-Iztaccíhuatl system.

In order to answer those questions, a careful review of the maps published by Lorenzo (1964) was needed. Cartographic inconsistencies directly affect the size of the reported glaciated areas for Citlaltépetl and interpretation thereof. Sketch III of Lorenzo (1964) shows two different scales for the same

map. One is an indicated scale of 1:50,000 and a graphic scale of 1:62,500 (see Figure 2). Hence, there must be differences between the distances between two points measured on that sketch and on a topographic map at the same scale (for instance INEGI, 2002). Examples of these inconsistencies are:

The distance from the mountain hut "Piedra Grande" to the center of the crater on the Sketch III of Lorenzo (1964; Figure 2) is 132 mm (on the map) or 8,250 m (according to the graphic scale) or 6,600 m (according to the indicated scale). The same distance on the INEGI (2002) topographic map is 62 mm (on the map) or 3,100 m (according to the indicated scale).

Distance from Sarcófago Peak to the center of the crater on the sketch III of Lorenzo (1964) is 59 mm (on the map) or 3,687.5 m (according to the graphic scale) or 2,950 m (according to the indicated scale). The same distance on the INEGI (2002) topographic map is 25 mm (on the map) or 1,250 m (according to the indicated scale).

The measurements extracted from sketch III of Lorenzo (1964; Figure 2) are slightly more than two-fold the distances measured on the INEGI (2002) topographic map. Similar problems are present on Sketch IV of Lorenzo (1964). The length of Jamapa glacier is reported to be ca. 5,600 m long, an impossible distance considering that the distance from the summit to the mountain hut is only 3100 m. If this distance was true, the glacier's front altitude should be lower than the hut's altitude. However, the data measured and reported for the glacial front (Lorenzo, 1964) is consistent with the INEGI (2002) topographic map and not with the Sketch III. Other cartographic elements provide further evidence supporting the inconsistencies listed above. From the topography shown in a Digital Elevation Model's (DEM) hillshade (SIGSA, 2006) and the aerial photo of 1975 (INEGI, 1975), it is evident that the shape of Glaciar Norte in 1958 was different from that reported by Lorenzo (1964).

The next sections focus on the correction of the Citlaltépetl's glaciated area. Also, a corrected contouring of the glacier is proposed based on the description of Lorenzo (1964) and all the available material. Namely, it was necessary to adjust the glacier geometry (as much as possible) to the topography depicted in a current Digital Elevation Model (DEM) and the 1975 aerial photo from INEGI (1975).

*Recalculation of the areal extent of Citlaltépetl volcano's glaciers.*

A methodology was established in order to recalculate the glacial extent of Glaciar Norte in 1958. This methodology needed to re-shape the glaciers' boundaries based on digital cartography, photogrammetry and terrain's visual observations. It first transports the outline of Glaciar Norte as reported by Lorenzo onto the level lines of the INEGI (2002) topographic map, re-scaling the dimensions of this outline. Thereafter, a new outline is established based on the glacier's outline in 1975 (mapped in this work) and the photographs reported by Lorenzo (1964). These two simple steps are further detailed below.

*Cartographic data*

For geographic correction and re-scaling of Glaciar Norte mapped by Lorenzo in 1958,

Sketch III (Lorenzo, 1964) and INEGI's (2002) topographic map (Coscomatepec sheet) were scanned and digitized at a resolution of 500 dpi pixel using a flat scanner Epson 836-XL. Additionally, a 10 meters resolution DEM (SIGSA, 2006) was used to rectify the scale and dephasing of Lorenzo's map (1964).

A set of aerial photographs from Lorenzo's work was used to display and identify the limits and morphology of the glacial cover in 1958. These photographs were also compared with a 1975 orthophoto of Citlaltépetl area (INEGI, 1975)

Every photograph was scanned with a flatbed scanner at a sampling resolution of 600 dpi. Then, the digitalized photograph was orthorectified using the Orthoengine module of PCI Geomatica® 10.0. This is a photogrammetry module useful to correct lens distortion, refraction, camera tilt, and terrain

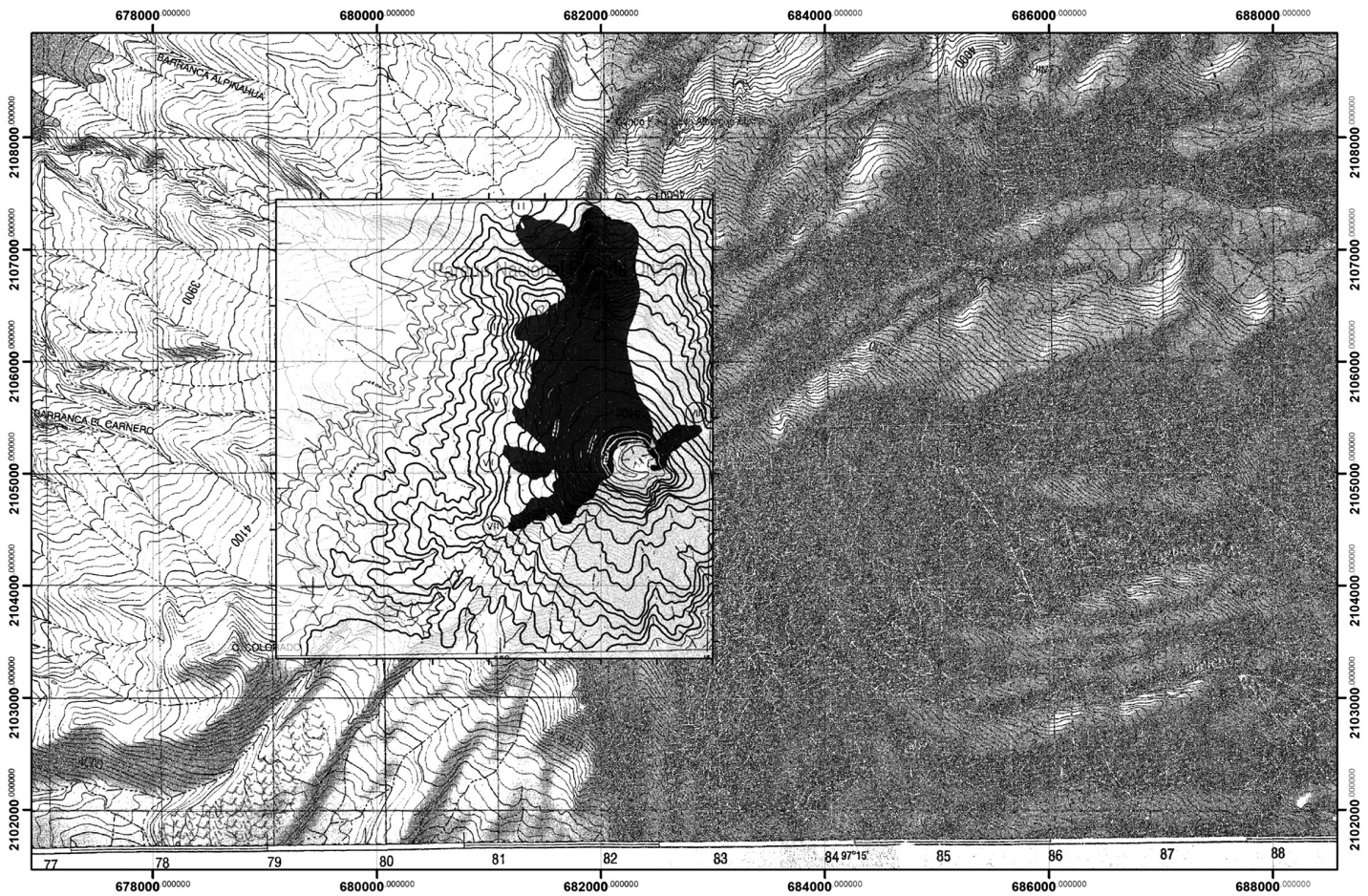


**Figure 3.** Adjustment of the map of Glaciar Norte with the topographic map according to the level contours of both maps.

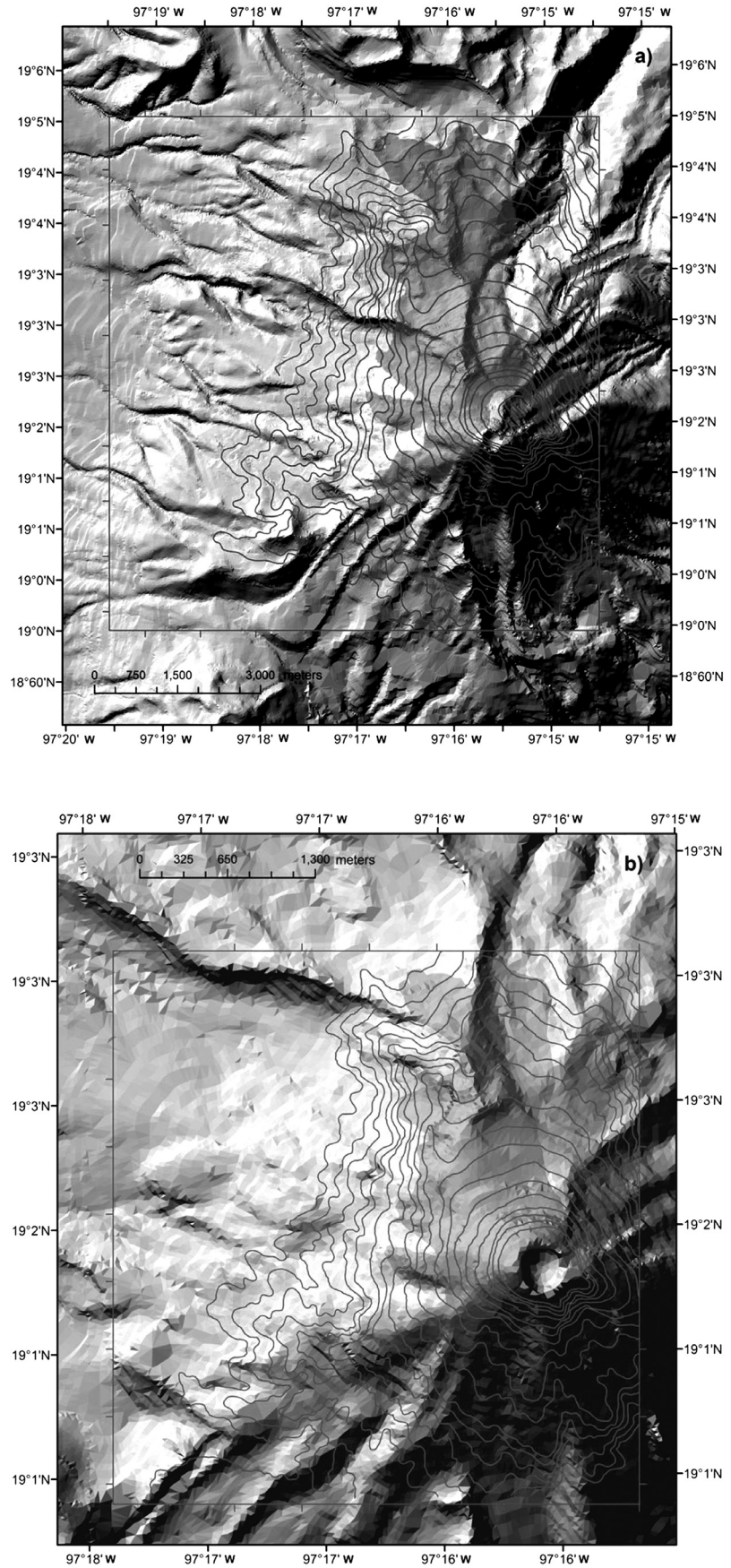


**Figure 4.** Geometric differences between a) the digitized and georeferenced map of Lorenzo (1964) and b) the cartographic correction made in this study. The hill-shade underneath is from a 2 m pixel resolution DEM.

relief affecting the geometry of the scene (Welch and Jordan 1996). The software uses the focal length of the camera and the fiducial marks (printed on the photos) to calculate the lens distortion, refraction and camera tilt.

In order to correct the geometry, and project the aerial photograph into a cartographic space, it was necessary to locate a series of Ground Control Points (GCP) which were obtained from published ground surveys like maps, georeferenced satellite images and GPS points measured in the field. For this work we got a set of GCPs through a comparison image to image between the aerial photo and a georeferenced panchromatic Landsat image for the December 9, 1999. This Landsat image was obtained on-line from the USGS catalogue via the USGS Global Visualization Viewer in 2006 (<http://glovis.usgs.gov/> last access: June 2013), and helped to find geographic features with a known location, recognizable on both images.

The outline of 1975 was mapped from an aerial photograph of INEGI (1975) taken in August 1975. The terrain relief effect was corrected using a set of GCPs and a 1:20,000 DEM. Using both, the software corrects the geometry of the scene and assigns a geographic projection. Then we obtained an orthophoto of Citlaltépetl volcano for 1975 where we visual and manually mapped the glacier extend for that year (Figures 5e and 7), clearly recognized on the photo.

#### *Georeferencing correction*

Digitized maps were georeferenced using the marks and projections established at every map. INEGI (2002) map was re-projected using UTM coordinates with the datum WGS-84 zone 14Q. This datum replaces the original datum ITRF-92. The map developed by Lorenzo (1964) was georeferenced using also UTM coordinates and the datum WGS-84. Both digital images were processed through the georeferencing modules of ENVI 4.3. Once georeferenced, the maps were corrected using a Geographic Information Systems (GIS), dephasing and re-sizing the map by Lorenzo (1964). The GIS interface used was ArcGIS 10.0.

The georeferenced and re-projected topographic map was overlaid with the georeferenced map of Lorenzo (1964) using the GIS interface. Then, they were fixed splicing similar features of the level lines in both maps (Figure 3). The adjustment of the maps was made following similar contour lines in both maps. For that adjustment it was necessary

to correct position and size of Glaciar Norte, which presented a slight dephasing according to the topography of the volcano (Figure 4a). At this step, the glacial area represented on the map had an extension of  $\sim 12 \text{ km}^2$  (Figure 4a) which is even larger than the area reported by Lorenzo (1964). Since most of the contour lines drawn in 1958 are completely different to the level lines in the topographic map, the main criterion to splice and correct this map was the flow of the contours which had some similar features at both maps. This resulted in a more consistent map with a new scale representing the 1958 glacial extent (Figure 4b). Here, it is necessary to mention the implicit error in this process, attributed to the appreciation of the contours and features when the maps were adjusted visually.

#### *Re-shape of Glaciar Norte, 1958*

Looking carefully the area covered by this glacier (Figure 4b), a part of it is over the Sarcófago Peak and other well-defined topographic ridges. This feature is wrong because at the time, the ice body occupied the topography within these ridges not covering them. Also, Lorenzo (1964) stated that Jamapa tongue fell down to the right side of Sarcófago Peak as he could see during his field campaign. Since the digitized and georeferenced outline, showed on Figure 4, did not fit correctly the topography, the Glaciar Norte's outline was reconstructed based on photographic material, DEM and GIS interface. The main step for this reconstruction was the recognition of the most characteristic features of the terrain where the ice body was. The descriptions made by Lorenzo (1964) for all the glacial tongues were followed in order to find the outlines, direction and flow of this glacier.

#### *Photographic catalogue analysis*

Figure 5 shows some characteristic terrain features: lava flows, moraines, cliffs, and the general geomorphology. These auxiliary features indicate the position of Citlaltépetl's glaciers. Other representative features were also considered like Sarcófago Peak, the crater, the eastern flank of Sarcófago where Jamapa glacier flows down, and the knowledge of the authors about this mountain.

The outline of the glacier depicted by Lorenzo (1964) was useful to clearly identify all the glacial tongues and their position. Lorenzo (1964, page 95) stated: "*We found that the entire northern side is covered in ice, down to varying altitudes, the lowest being that of the two tongues into which Jamapa glacier divides,*

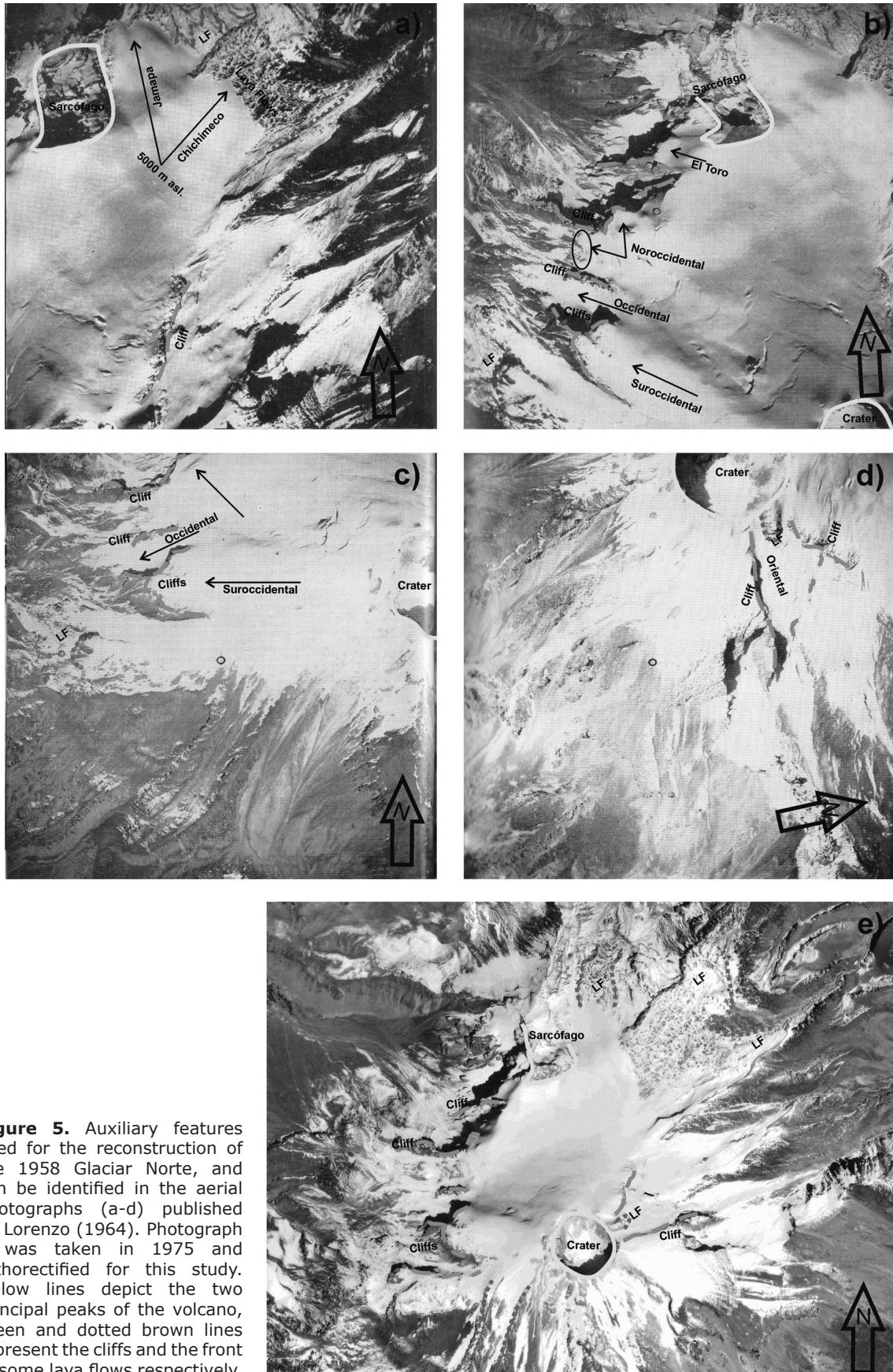


**Figure 5.** Auxiliary features used for the reconstruction of the 1958 Glaciar Norte, and can be identified in the aerial photographs (a-d) published by Lorenzo (1964). Photograph e was taken in 1975 and orthorectified for this study. Yellow lines depict the two principal peaks of the volcano, green and dotted brown lines represent the cliffs and the front of some lava flows respectively.

and believed, as it was later confirmed, that we had before us the greatest glacier formation of Mexico" (see Figure 5a). Additionally, Chichimeco tongue was identified north to the crater and it was described as a wide glacial tongue poorly developed longitudinally. This tongue also comes from an altitude of ca. 5000 m and the front gets as low as 4,740 m (Figure 5a).

On the western flank of the volcano there are remains of glacial tongues coming from Glaciar Norte. Most of them were hanging glaciers. Starting at the southwestern flank of Sarcófago Peak, El Toro glacier flowed down as an icefall following a step-like topography, stopping at 4,930 m. Something similar happened to La Barba glacier, south of El Toro but whose front reached down an altitude of 5,090 m (Figure 5b). At the western part of Glaciar Norte and south of the big walls of the cliffs there is a poorly recognized glacial tongue called Noroccidental. This glacier descends to 4920 m and is located north of Occidental glacier, which at the same time descends to an altitude of 4980 m from an altitude of 5200 m (Figures 5b and 5c). Finally, Suroccidental glacier represents the ice mass that follows a Southwest direction from the top of Glaciar Norte, with a low altitude of 4980 m (Figure 5c).

Glaciar Oriental is east of Glaciar Norte and separated from it. This is a niche glacier on to the eastern flank (Figure 5d). It has a maximum and minimum altitudes of 5,500 m and 5,070 m, respectively. Figure 5e shows the entire glaciated area as observed at the orthorectified airphoto of 1975. By this time the glacier system receded and the bedrock of the 1958 glacial cover was exposed.

Finally, using this orthophoto and the analysis made above, the Glaciar Norte outline for 1958 was delimited and reconstructed. This reconstruction is shown at Figure 6 over a 1998 orthophoto (scale 1:25,000) obtained from SCT (1998).

From this picture it is clear to see the distortion of the glacier outline made by Lorenzo (1964; Figure 2). However, the idea that he had about the glacial area on Citlaltépetl clearly describes the main features of that glacier as we can compare from Figure 6.

#### *Error estimation*

Errors involved in the geographic correction and the reconstruction of Glaciar Norte are considered independent each other

because each process of this methodology is independent. Then, errors considered here are attributed to digitization and georeferentiation processes and to the DEM for the calculation of elevations.

#### *Digitization process*

The aerial photograph of 1975 was digitalized in a flatbed scanner Epson Expressions 836-XL with a resolution of 600 dpi, equivalent to 42.3  $\mu\text{m}$  of pixel size. Then, the error assigned here was 2.116 m. Further details on error calculation can be found in Linder (2009).

#### *Georeferentiation process*

The error after the georeferencing process was estimated in 7m. For georeferentiation of the 1975 photograph we used PCI Geomatica® 10.0 software with a DEM resolution of  $\pm 3$  m horizontal and  $\pm 5$  m vertical.

The final horizontal error for this image is  $\pm 9$  m. This is the sum of digitization and georeferencing error. This error is fairly good considering the magnitude of the areas calculated in this study.

#### *DEM error*

A 2 m pixel resolution DEM was used for calculation of glacier front elevations. DEM was interpolated from a set of contour lines at 10 m intervals. Due to the vertical error of  $\pm 5$  m of the DEM and considering the horizontal error attributed to the orthophoto, the total vertical error is estimated in  $\pm 10$  m.

## **Results**

After geographic correction of the 1958 glacier outline mapped by Lorenzo (1964), a new outline of Glaciar Norte digitized and geographically corrected was obtained (Figure 6). This corrected outline had the same geometry determined by Lorenzo (1964) as seen at his Sketch III (Figures 2, 4b, and 6 this study). The outlines were handled as a shape file into a GIS interface obtaining an area of 2.24  $\text{km}^2$  (Oriental glacier included) and a minimal altitude for the Jamapa glacier front at 4,670 m. This areal value is very different from that reported by Lorenzo (1964) where he mentioned an area of  $\sim 9.5$   $\text{km}^2$  and a minimal altitude for the Jamapa glacier front of 4,640 m. In spite of the huge difference, with this corrected value the glacier system of Citlaltépetl still represents the largest glacial area in Mexico for 1958, as compared to the total glacial area of Iztaccíhuatl and Popocatépetl ( $\sim 1.93$   $\text{km}^2$ ). The reconstructed area of Glaciar Norte shown

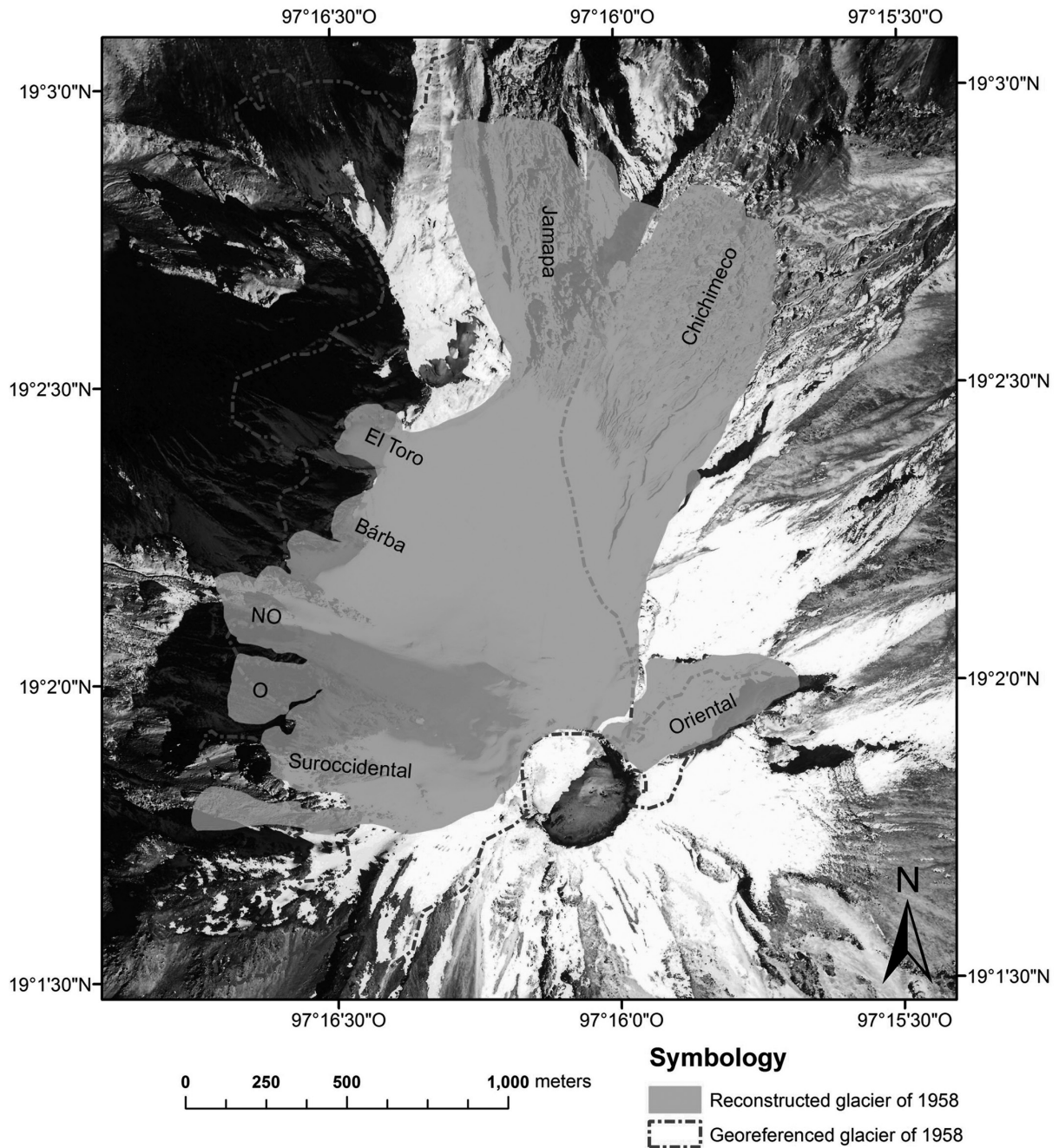


**Figure 6.** Reconstructed Glaciar Norte for 1958 vs. the geographically corrected Glaciar Norte mapped by Lorenzo in 1958. Orthophoto was made from an aerial photograph taken in December 1998.

here is of 2.16 km<sup>2</sup> (solid outline in Figure 6) where the area of Oriental glacier is of 0.118 km<sup>2</sup>. We consider the new outline as a more realistic representation of Glaciar Norte glacier in 1958.

Comparing the resultant outline with that determined in this study for 1975, Chichimeco glacier retracted considerably since 1958. This is not true for the rest of the glaciers, which

are still similar. Jamapa glacier also retreated but less than Chichimeco glacier (Figure 7). From this, it is possible to think that retraction of Glaciar Norte from 1958 to 1975 (480,000 m<sup>2</sup> or 24%) was caused by the same order-of-magnitude climate effect as in the case of the other two mountains in Mexico, and not by an intense and unique climate change where glacier area lost would be of ca. 8 km<sup>2</sup> which means a loss of 84%.

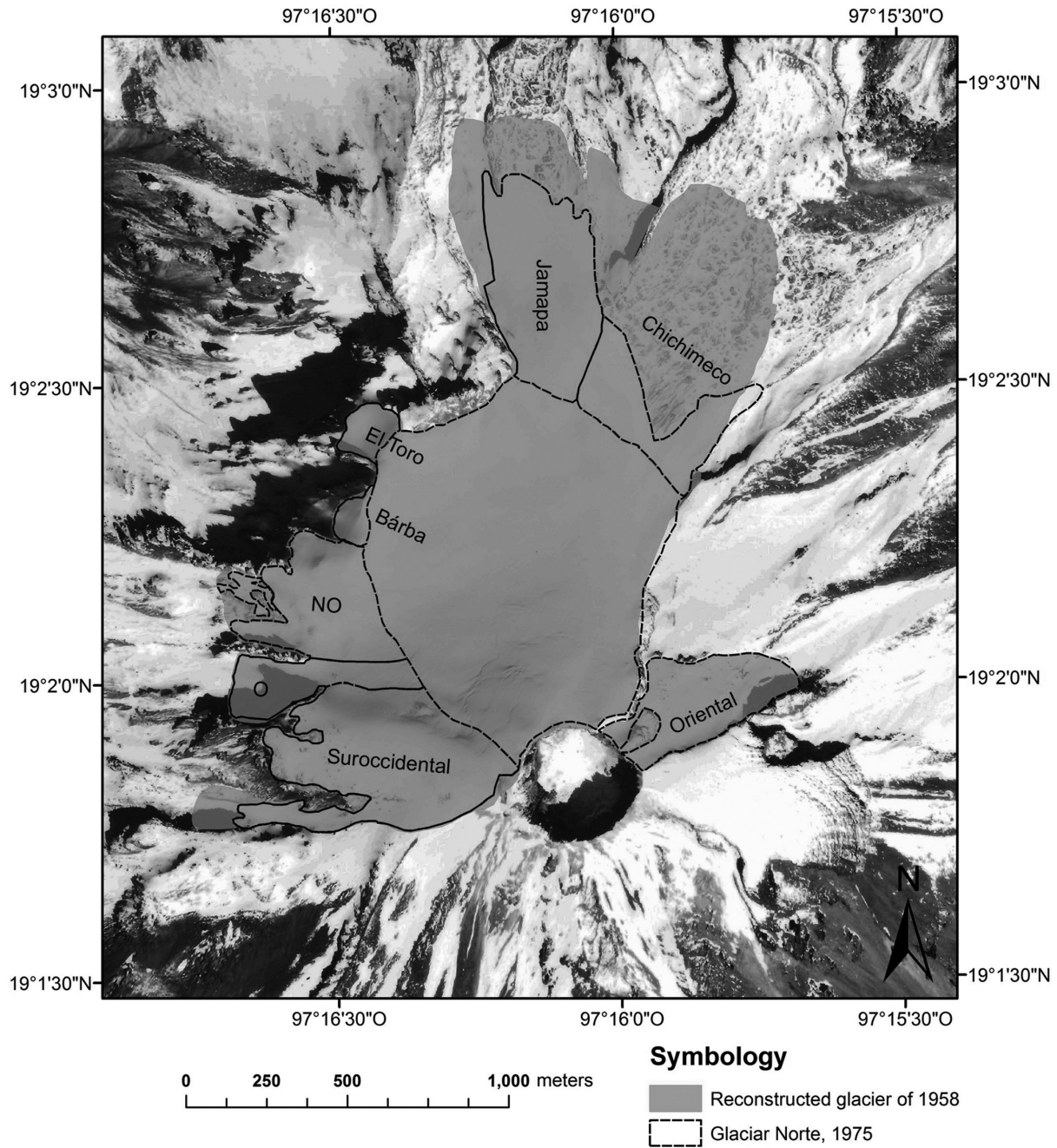


**Figure 7.** Glacier boundaries in 1958 and 1975 using the reconstructed 1958 area of Glaciar Norte. The orthophoto was made from an aerial photograph taken in August 1975 at a scale 1:50,000.

**Discussion**

After Lorenzo’s 1958 glacial inventory, new studies have been done on Citlaltépetl’s glaciers in order to understand their dynamics and climate behavior. One purpose of those studies was the evaluation of glacial shrinkage in Mexico, considering the end of the Little Ice Age (LIA) as starting point (e.g. Palacios and

Vázquez-Selem, 1996; Álvarez and Delgado-Granados, 2002). Recently, Ontiveros-González *et al.* (submitted) tackle the study of glacial shrinkage in Mexico showing the relationship between the surface energy balance and the retreat of glacierized areas. It is important to notice that most of those studies considered the area and outlines of Glaciar Norte reported by Lorenzo (1964). Caution should be taken

because it overestimates the climate effect on the glacial shrinkage in Mexico.

Using the results mentioned above, the evaluation of the glacial retreat on Citlaltépetl can be tackled. Also, a comparison with the retreat at other mountain glaciers around the world (Zemp *et al.* 2006) can be attempted. Considering the glacial shrinkage in Mexico starting at the end of the LIA, the Jamapa glacier retreated vertically a little more than 200 m in *ca.* 108 years considering that the minimal altitude of its front was at *ca.* 4,395 m (Palacios and Vázquez-Selem, 1996). From 1958 to 2001 the front of Glaciar Norte retreated more than 300 m causing the total disappearance of Jamapa glacial tongue (see Table 1). The last value represents a rapid retreat of the ice body in only 43 years. Then, this could mean a strong direct climatic effect since volcanic activity (diffuse degassing, localized thermal activity of  $<60^{\circ}\text{C}$ ) is negligible for this volcano.

This interpretation could be misleading because the change only represents the retraction of one glacial tongue. If we consider the areal change of the glaciated area from 1958 to 1975 (Table 1), the glaciated area lost at Citlaltépetl was 24% of the 1958 total area. On the other hand, the ice lost from 1958 to 2001 represented 52% of the 1958 total area that means a retreat rate of 25,000  $\text{m}^2/\text{yr}$ . In spite of this difference, we can see that between 1958 and 1975 the retreat rate is of the same order-of-magnitude as from 1958 to 2001 (28,000  $\text{m}^2/\text{yr}$ ). This means that the effect of climate on Glaciar Norte is more or less constant in the short- and long-term; even the glacier front retreats fast (see Delgado Granados, 2007). This is because there are zones prone to retraction due to the

slope, aspect and insolation (Cortés-Ramos and Delgado Granados, 2012).

In contrast, considering the value reported by Lorenzo (1964), the 1958-2001 glacial retreat represents a 90% ice loss of the 1958 glaciated area. Then, this dramatic mass loss in just 43 years had to be reflected in the ecosystems and populated areas in the vicinity, something that has not been documented so far. The dramatic shrinkage this data represents, implies an effect of strong climatic changes around the glacial surface characterized by a series of high temperatures, strong radiation and deficits of precipitation. However, there are no references in the literature reporting extreme conditions that produce  $\sim 8 \text{ km}^2$  of glaciated area disappearance. Furthermore, it is hard to imagine that a large ice mass melt fast along 43 years without a hydrological report of anomalous floods associated to this retreat at the related irrigation system.

Citlaltépetl volcano's climate is poorly known so far. However, the study of Palacios *et al.* (1999) about Jamapa glacier mentions that Lauer and Klaus (1975) and Lauer (1978) provided important data about the climatology of the mountain. They said that at 4,000 m on the western slope of the volcano, the mean annual temperature is about  $5^{\circ}\text{C}$ . The average number of days with minimum temperatures below freezing is 200, whereas the average number of days with maximum temperatures below freezing is 45. This area had an annual precipitation of 900 mm being these conditions almost similar along the year. Thus, with these climate conditions, a dramatic shrinkage of the glaciers on Citlaltépetl volcano ( $8 \text{ km}^2$  of extension) cannot be sustained.

**Table 1.** Extension changes of Mexican glaciers since the end of the LIA. \*Glacial area reported by Lorenzo (1964). \*\*Glacial area reported in this study. <sup>a</sup>Data corrected after Cortés-Ramos and Delgado-Granados (2013).

CITLATÉPETL				POPOCATÉPETL				IZTACCÍHUATL			
Year	Altitude of glacier front (m)	Area $\text{km}^2$	Retreat rate $\text{km}^2/\text{yr}$	Year	Altitude of glacier front (m)	Area $\text{km}^2$	Retreat rate $\text{km}^2/\text{yr}$	Year	Altitude of glacier front (m)	Area $\text{km}^2$	Retreat rate $\text{km}^2/\text{yr}$
1850	4395	--	--					1850	4350	6.369	--
1958*	4640	9.5	--	1958*	4690	0.892011	--	1958*	4700	1.369	-0.046
1958**	4640	2.04	--	1982	4760	0.559	-0.014	1973	4750	0.909	-0.031
1975	4700	1.56	-0.028	1996	4785	0.537	-0.002	1982	4830	0.863	-0.005
2001 <sup>a</sup>	4980	0.98	-0.025	2000	4925	0.255	-0.071	2001	4900	0.435	-0.023

## Conclusions

The inconsistencies found in this study lead to conclude that the glacial area determined by Lorenzo in 1964 ( $\sim 9.5 \text{ km}^2$ ) was wrong. Therefore, the glaciers on Citlaltépetl volcano or the climate conditions in the surrounding area were not very different from those at Popocatepetl and Iztaccíhuatl at the time of that study. Furthermore, considering the altitudes measured in 1958, in average they are comparably the same indicating that climatic conditions for all glacier systems is the same because they reached the same average minimal altitude.

Citlaltépetl's glaciated area reported by Lorenzo (1964) was geographically corrected after an analysis of cartographic errors. Errors were confirmed and mainly attributed to the methodology applied to map the measurements made in the field. Since the cartographic material and the aerial photographs available at the time were poor and not enough, it is concluded that the map published by Lorenzo and his team in 1964 was possibly made by hand and without any auxiliary cartography to support their mapping. As a consequence, the resulting map was a distorted representation of Glaciar Norte where the magnitude of the area was exaggerated and the outlines did not coincide with the topography of the volcano.

A reconstruction of Glaciar Norte was made and the 1958 glaciated area calculated as realistically as possible. The obtained area is useful to better understand the climate effect on the glacier, in spite of paucity of data that may allow for a precise relationship between the glacial shrinkage and the climate factors involved in the process. The new 1958 glaciated area value for Citlaltépetl volcano discard any mechanic, volcanic, or strong climatic event that triggered an accelerated shrinkage of the glacier system, in contrast with the implications that rise when using the value reported by Lorenzo (1964).

Finally, this study is a key to update the glacial inventory at Citlaltépetl volcano and correct that of Mexican glaciers currently existing at the World Glacier Monitoring Service database.

## Acknowledgements

The authors want to express their profound admiration and recognition to the remarkable, visionary and thoughtful study Lorenzo and his colleagues did in 1958, later published in 1964. We want to state that this study does

not represent, by any means, detracting to the pioneering work of José Luis Lorenzo. The authors know by personal experiences how difficult the fieldwork can be on the Mexican mountains. So, the difficulties encountered in 1958 were much larger than they are at present and it is understandable that at some point, those problems were reflected in the final outcome especially under the enormous pressure to report the total glaciated areas of the country for the IGY. Thus, this study tries to make a correction for the sake of science, and not to diminish the merit of Lorenzo's work. This study was supported by DGAPA (grant IN-113914) and CONACYT (Consejo Nacional de Ciencia y Tecnología) through grant 83633.). The first author acknowledges the scholarship granted by CONACYT. Secretaría de Comunicaciones y Transportes is greatly acknowledged for supplying the aerial photographs used in this study. Also, the authors want to thank Simone Fisher for her preliminary study about the correction of cartography, during her scholar visit to Mexico in 2005, her report was very useful to better detect the inconsistencies described in this study. We acknowledge to Kerygma Larrazabal, Natalie Ortíz and the anonymous reviewers for their comments and suggestions to improve this manuscript.

## References

- Álvarez R., Delgado Granados H., 2002, Characterization of a tropical ice body on Iztaccíhuatl volcano, Mexico, in Ninth International Conference on Ground Penetrating Radar, Proceedings of SPIE, 4758, 2000, pp. 438–442
- Cortés-Ramos J., Delgado Granados H., 2012, The recent retreat of Mexican glaciers on Citlaltépetl Volcano detected using ASTER data. *The Cryosphere Discussions*, 6, 3149–3176.
- Cortés-Ramos J., Delgado Granados H., 2013, La evolución del mayor glaciar de México vista desde el espacio. Primera Edición. Coordinación de Estudios de Posgrado (Ed.), UNAM, México.
- Delgado Granados H., 2007, Climate change vs. Volcanic activity: Forcing Mexican glaciers to extinguish and related hazards, in Proceedings of the First International Conference on the Impact of Climate Change on High-Mountain Systems. Instituto de Hidrología, Meteorología y Estudios Ambientales, Bogotá, Colombia, pp. 153–168.

- Delgado Granados H., Julio Miranda P., Huggel C., Ortega del Valle S., Alatorre Ibarguengoitia M.A., 2007, Chronicle of a death foretold: Extinction of the small-size tropical glaciers of Popocatepetl volcano (Mexico). *Global and Planetary Change*, 56, 13–22.
- Delgado H., Brugman M., 1994, Monitoreo de los glaciares del Popocatepetl. Centro Nacional de Prevención de Desastres (Ed.), Volcan Popocatepetl, estudios realizados durante la crisis de 1994, 1995, 221–241.
- INEGI (Instituto Nacional de Estadística Geografía e Informática), 1975, Archivo aéreo-fotográfico escala 1:50,000. Volcán Citlaltépetl, zona 18-A-A.
- INEGI (Instituto Nacional de Estadística Geografía e Informática), 2002, Mapa topográfico escala 1:50,000. Coscomapetec de Bravo, zona E14B46.
- Lauer W., 1978, Timberline studies in central Mexico. *Arctic and Alpine Research*, 383–396.
- Lauer W., Klaus D., 1975, Geoecological investigations on the timberline of Pico de Orizaba, Mexico. *Arctic and Alpine Research*, 315–330.
- Linder W., 2009, Digital photogrammetry: A Practical Course, 3rd. edition. Springer, New York, 227 pp.
- Lorenzo J.L., 1964, Los glaciares de México, 2nd ed. Universidad Nacional Autónoma de México, 124 pp.
- Ontiveros-González G., Delgado Granados H., Cortés-Ramos J., (submitted), The Surface Energy Balance of Glaciar Norte on Citlaltépetl Volcano, Mexico during 2006–2009. *Geofísica Internacional*.
- Palacios D., Parrilla G., Zamorano J.J., 1999, Paraglacial and postglacial debris flows on a Little Ice Age terminal moraine: Jamapa Glacier, Pico de Orizaba (Mexico). *Geomorphology*, 28, 95–118.
- Palacios D., Vázquez-Selem L., 1996, Geomorphic Effects of the Retreat of Jamapa Glacier, Pico de Orizaba Volcano (Mexico). *Geografiska Annaler. Series A, Physical Geography*, 78, 19–34.
- Schneider, D., Delgado Granados, H., Huggel, C., Kääb, A., 2008. Assessing lahars from ice-capped volcanoes using ASTER satellite data, the SRTM DTM and two different flow models: case study on Iztaccíhuatl (Central Mexico). *Natural Hazards and Earth System Science*, 8, 559–571.
- SCT (Secretaria de Comunicaciones y Transportes), 1998, Archivo aéreo-fotográfico escala 1:25,000. Volcán Citlaltépetl.
- SIGSA (Sistemas de Información Geográfica S. A.), 2006, Proyecto México: Modelos Digitales de Elevación escala 1:20,000. Volcán Citlaltépetl.
- Waitz P., 1910, Observaciones geológicas acerca del Pico de Orizaba. *Boletín de la Sociedad Geológica Mexicana*, 7, 67–76.
- Waitz P., 1921, Popocatepetl again in activity. *American Journal of Science*, 5, 1, 81–87.
- Welch, R. and Jordan, T. R., 1996, Using scanned air photographs. Raster Imagery in geographic Information Systems (S. Morain and S.L. Baros, eds), Onward Press, 55–69.
- White S.E., 1954, The Firn Field on the Volcano Popocatepetl, Mexico. *Journal of Glaciology*, 2, 389–392.
- White S.E., 1956, Probable Substages of Glaciation on Iztaccíhuatl, Mexico. *The Journal of Geology*, 64, 289–295.
- Zemp M., Haeberli W., Bajracharya S., Chinn T. J., Fountain A. G., Hagen J. O., Huggel C., Kääb A., Kaltenborn B. P., Karki M., Kaser G., Kotlyakov V. M., Lambrechts C., Li Z., Molnia B. F., Mool P., Nellesmann C., Novikov V., Osipova G. B., Rivera A., Shrestha B., Svoboda F., Tsvetkov D. G., Yao T., 2006, Glaciers and ice caps, in: Global Outlook for ice and snow, UNEP (Ed.), Arendal, Norway, 27, 115–152.

## New Paleomagnetic results and evidence for a geomagnetic field excursion during the pleistocene-holocene transition at Pichincha province, Ecuador

Hugo G. Nami

Received: October 09, 2013; accepted: September 09, 2014; published on line: March 31, 2015

### Resumen

Se reportan datos paleomagnéticos de tres secciones sedimentarias del noroeste de Sudamérica (Ecuador). Las direcciones del magnetismo remanente natural obtenido de 109 muestras orientadas tomadas en 4 sitios -ciudad de Quito (QC), Mullimica (Mu) y El Tingo (ET)- mostraron que algunas registraron un componente magnético diferente al campo geomagnético (CGM) normal actual. La magnetización característica fue determinada por desmagnetización progresiva de campos alternos. El análisis de las muestras mostró que las secciones registraron una magnetización remanente característica de polaridades normales, intermedias y reversas durante la transición Pleistoceno-Holoceno y Holoceno. En QC se registraron direcciones de polaridad normal, mientras que normal e intermedia en Mu y, polos geomagnéticos virtuales (VGVs) reversos en el ET. QC y la parte superior de Mu corresponden a la variación paleosecular del Holoceno en Ecuador durante los  $\sim 4,7$  ka BP. Por otro lado, la parte inferior del registro de Mu representa la transición de direcciones normales a intermedias ocurridas a  $\geq 5,6$  ka BP. En ET se observaron dos registros estables oblicuos reversos con una gran fluctuación lejana del campo geomagnético actual a los  $\sim 10,5$  ka BP. Los polos geomagnéticos virtuales (PGV) transicionales generalmente

coinciden con los registrados durante la posible excursión acaecida durante la transición Pleistoceno-Holoceno observada en otros lugares del planeta. Cuando se los representa en un mapa del mundo actual, los PGV calculados a partir de las muestras normales de QC están muy bien agrupados en el norte de América del Norte, Groenlandia y el norte de Europa; la mayoría de los de Mu se sitúan entre  $30^\circ$  y  $60^\circ$  de latitud norte en América del Norte, Groenlandia, oeste de Europa, África y el norte del Océano Pacífico. La mayoría de las direcciones reversas de ET se agrupan en un parche ubicado en el sur de África, y unos pocos están situados en el centro de África, el este de Australia y la Antártida. Con los PGV resultantes de QC y Mu se calculó un paleopolo ecuatorial; también fueron procesados otros paleopolos de la misma edad en sitios de Norte y Sud América. Cabe destacar que coinciden bien, aunque mostraron una diferencia angular  $\sim 15^\circ$  con respecto al eje de la rotación de la Tierra. Finalmente, se discute la hipótesis del estado excursional global del CGM durante los últimos  $\sim 11,0$  ka BP y el uso potencial como herramienta de datación de la excursión fechada en 10.5 ka BP.

Palabras clave: Paleomagnetismo, variación paleosecular, excursión, transición Pleistoceno-Holoceno, Holoceno, América del Sur.

---

H. G. Nami  
CONICET-IGEBBA  
Laboratorio de paleomagnetismo  
"Daniel A. Valencio"  
Departamento de Ciencias Geológicas  
Facultad de Ciencias Exactas  
Físicas y Naturales  
Universidad de Buenos Aires  
Ciudad Universitaria (Pabellón II)  
(1428) Buenos Aires, Argentina  
Associated researcher  
National Museum of Natural History  
Smithsonian Institution  
Wa. D.C., U.S.A.  
*Corresponding author: hgnami@fulbrightmail.org*

## Abstract

Paleomagnetic data from three sedimentary sections in Pichincha province -Quito City (QC), Mullimica (Mu) and El Tingo (ET)- Ecuador (northwestern South America) are reported. Analysis of natural remanent magnetization directions obtained from 109 oriented samples taken at 4 sites, shows that some samples recorded a magnetic component different from the normal present geomagnetic field (GMF). The characteristic remanent magnetization (ChRM) was determined by progressive AF demagnetization. The analysis shows that the sections recorded ChRM of normal, intermediate and reverse polarities during the Pleistocene-Holocene transition and Holocene. Normal directions were recorded in QC, while normal and intermediate polarity directions at Mu and, reverse VGPs at ET. QC and the upper portion of Mu correspond to the paleosecular variation Holocene record for Ecuador during the  $\sim \leq 4.7$  ka BP. On the other hand, the lower portion of Mu logs represents the transition from normal to intermediate directions occurring at  $\sim \geq 5.6$  ka BP. Sites from ET recorded two stable oblique reverse records with a large fluctuation far from the present GMF at  $\sim 10.5$  ka BP. The transitional virtual geomagnetic poles generally agree with those registered during the possible

Pleistocene-Holocene excursion observed in other places of the planet. When plotted in a present world map, VGPs calculated from normal samples at QC are very well clustered in Northern North America, Greenland and Northern Europe; most VGP's calculated from Mu are situated between  $30^\circ$  and  $60^\circ$  northern latitude in Northern North America, Greenland, western Europe, Africa and North Pacific Ocean. Interestingly, the majority of the reverse directions from ET conforms a patch located in southern Africa, and a few ones are situated in central Africa, eastern Australia and Antarctica. An Ecuadorian paleopole was calculated with data resulting from QC and Mu. Also other paleopoles of the same age were processed from other North and South American sites. Remarkably they agree well, although they do not agree with the geographical pole showing  $\sim 15^\circ$  angular difference in relation to the rotation's axis of the Earth. Finally, is discussed the hypothesis of the global excursions state of the GMF during the last  $\sim 11.0$  ka BP and the potential use as dating tool the excursion dated at 10.5 ka BP.

**Key words:** Paleomagnetism, paleosecular variation, excursion, Pleistocene-Holocene transition, Holocene, South America.

## Introduction

During the last decades, a number of paleomagnetic records across the world yielded anomalous geomagnetic field (GMF) directions likely corresponding to different excursions occurred during the terminal Pleistocene and Holocene (e.g. Petrova and Pospelova, 1990; Burakov and Nachasova, 1990; Dergachev *et al.*, 2004, 2012; Guskova *et al.*, 2008; Kochegura and Pisarevsky, 1994; Lund *et al.*, 2007, 2008; Moreiras *et al.*, 2013; Nami, 1995, 1999a, 1999b; Nelson, 2009; Platzman *et al.*, 2010; Raspopov *et al.*, 2003; Urrutia-Fucugauchi *et al.*, 1995; Zhu *et al.*, 1998; among others). Radiocarbon dating indicates that they span the last  $\sim 11000$ - $10000$  uncalibrated or  $\sim 13000$ - $12000$  calibrated years before present that, hereafter they are respectively referred as  $\sim 11$ - $10$  ka BP or  $\sim 13$ - $12$  cal. ka BP. Investigations on this topic have significant geomagnetic, environmental and stratigraphic implications (e.g., Westaway, 2003; Backmutov, 2006; Constable and Korte, 2006; Brown *et al.*, 2007; Kuznetsova and Kuznetsov, 2008; Dergachev *et al.*, 2012). Additionally, due to the occurrence of this kind

of GMF behavior paleomagnetic data may be used as dating tools (Parkes, 1986; Thompson, 1991; Herz and Garrison, 1998). For this reason, compatible evidence on diverse material of similar age must be investigated using similar sampling and laboratory techniques (Roberts and Piper, 1989). Therefore, sampling in sedimentary sections from diverse environments was conducted in the Republic of Ecuador. The main goal was to explore the Late Pleistocene-Holocene GMF behavior in a low latitude area, because GMF anomalous records were previously observed at other latitudes across North and South America (e.g., Clark and Kennett, 1973; Gonzalez *et al.*, 1997; Urrutia-Fucugauchi *et al.*, 1995; Nami, 1999a, 1999b, 2012, 2013; Nami and Sinito, 1991, 1993, 1995; Ortega Guerrero and Urrutia-Fucugauchi, 1997; Sinito *et al.*, 1997, 2001; Moreiras *et al.*, 2013).

## Study area, sampling sites and chronology

The sampling sites are located around the Ilaló hill, Los Chillos valley in the Pichincha province (Figure 1). A brief description of the sites follows:

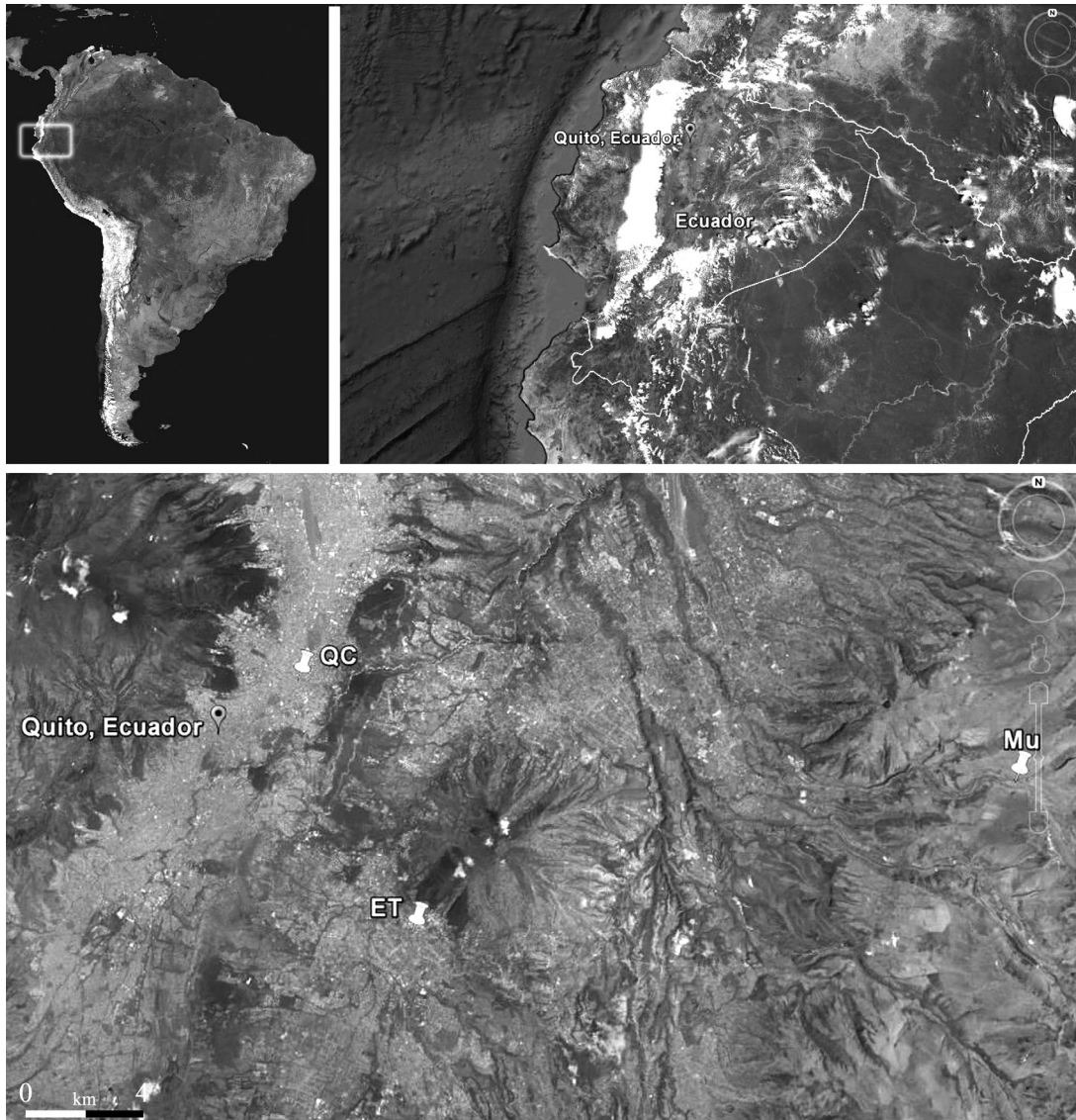


**Figure 1.** Map of Ecuador and location of the sampling sites mentioned in the text. QC: Quito City, Mu: Mullimica, ET: El Tingo (after Google Maps, 2013).

Quito city (QC,  $00^{\circ} 12.10' S$ ,  $78^{\circ} 29.40' W$ ) section belongs to a  $\sim 2.30$  meter deep pit made on Gerónimo Carrión St. for a building construction in Quito city. Despite of nowadays there is not evidence of alluvial activity, the sediments represent a characteristic lacustrine environment, formed by an ancient lake existing in this part of Quito until the Spanish conquest and colonial times. Due to the sedimentological and lithological composition, 9 intercalated clay, sand and silty sand natural strata were identified at QC, numbered "I" to "IX" (Figure 2a).

Mullimica (Mu,  $00^{\circ} 14.40' S$ ,  $78^{\circ} 14.58' W$ ) is situated at the *paramo* in the eastern cordillera at about 4000 m.a.s.l. The paleomagnetic

sampling was performed on the left bank of San Lorenzo River, very close to its intersection with the Quebrada de Mullimica (Salazar, 1980). The sedimentary pile consist in a 2 m thick deposit of homogeneous black sediment overlying a late glacial deposit of pebbles and cobbles (Figure 2b)

El Tingo (ET,  $00^{\circ} 17.43' S$ ,  $78^{\circ} 26.88' W$ ) is located in the homonymous village situated at Los Chillos Valley, southeast of Quito. The sampling was made in the upper part of a large section of *cangagua* that is a very fine volcanic material similar to loess, but with different mineralogical composition; although, this geological unit is widely believed to have been deposited during a glacial episode in the

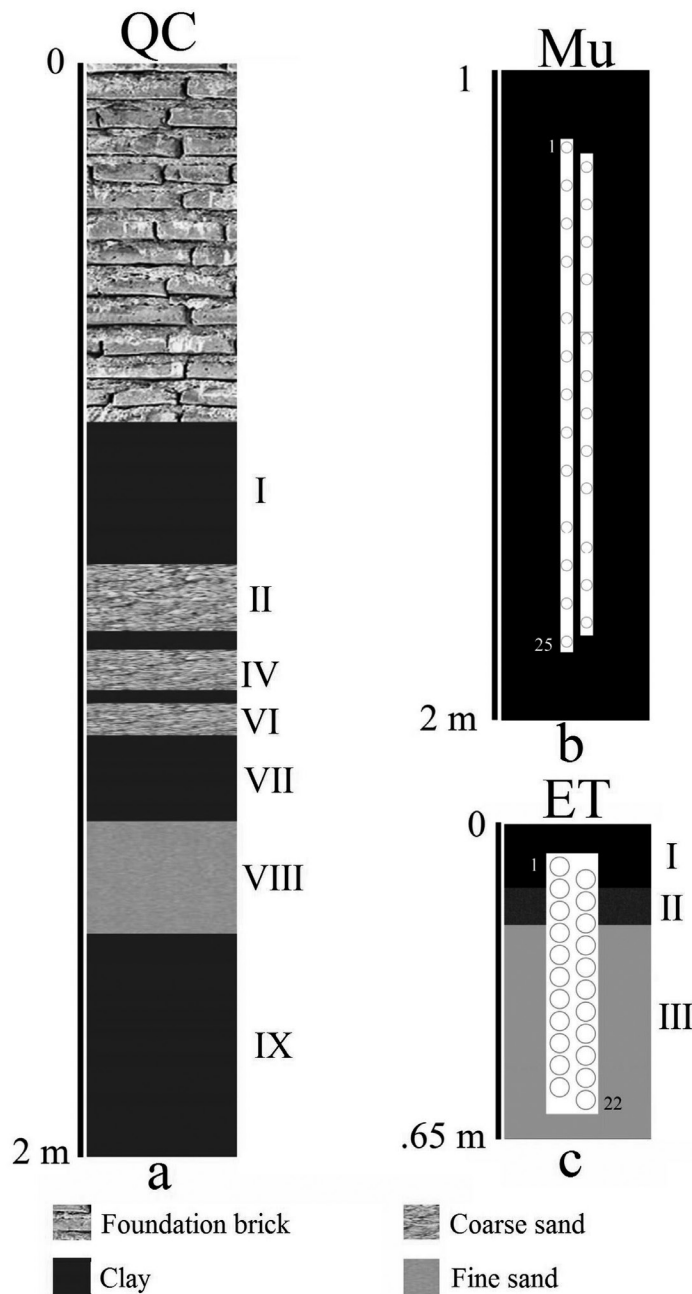


**Figure 2.** Schematic stratigraphic profiles showing the sampled sections, AMS dates and location of the palaeomagnetic sampling related to stratigraphy at Mu and ET. Numbers on the cylinders' top and bottom show the correlative order of the samples. In the text is given the description of each stratigraphic level which is numbered with roman numbers on the right of each section. At QC, level III and V were not numbered.

Pleistocene (Sauer, 1965). Elsewhere in the Ilaló region, the upper part of the *cangagua* yielded highly diagnostic archaeological Paleoindian "fishtail" or Fell projectile points (Bell, 1965; Mayer-Oakes and Bell, 1960; Mayer-Oakes, 1963, 1966, 1986) which in South America were consistently dated ~11-10 ka BP (Nami, 2007: Table 1). Most of the archaeological remains at these sites occur on a dark layer of sediment overlying regional deposits of *cangagua*, a volcanic tuff presently exposed in the lower slopes of the Ilaló hill (Mayer-Oakes, 1966).

Considering the stratigraphic occurrence of the Paleoindian discoveries as well as the Pleistocene age of the deposit, it must be considered as Late Pleistocene/early Holocene in age. For this reason, with paleomagnetic purposes, only the upper part of the section underlying the recent soil was sampled, where the *cangagua* is the parental material.

It consisted of three levels, called here I, II and III (Figure 2c). Level I is the recent soil with vegetation, II is the transitional part between level I and III, which is formed by a gray *cangagua*.

**Table 1.** List of AMS dates obtained in the sites described in this paper. The calibrated ages were calculated with the "Calib radiocarbon calibration program" (Stuiver and Reimer, 1993) and the calibration data set assembled by Reimer and colleagues (2013).

Site	Depth cm	Material dated	<sup>14</sup> C age yr BP	95.4 % (2σ) (2s) cal age ranges (cal yr BP)	Relative area under distribution	Laboratory number
Quito City	189-192	Sediment	4730±40	5445-5494	0.22	CURL-5503
Mullimica	185-190	Sediment	5630±95	6277-6652	1.0	KI-5082
El Tingo	50-55	Sediment	10550±55	12254-12256	0.001	CURL-5504

AMS radiocarbon dating technique (Hedges and Gowlett, 1986; Taylor, 1997) showed to be highly useful for dating the sediment's organic matter (Wang *et al.*, 1996; Willey *et al.*, 1998; Pessenda *et al.*, 2001). Dates from this kind of material tend to provide reliable calibrated ages. However, it can be considered as a minimum age because the apparent mean residence time (MRT) of organic components is an important factor in soil dating. This is because the mix of younger and old organic matter that might provide younger dates (Scharpenseel, 1971, 1976; Scharpenseel and Schiffmann, 1977; Stein, 1992). Then, sediment samples were submitted to determine the age of each site. QC and ET AMS measurements and ages calculation were performed by the NOSAMS facility at Woods Hole Oceanographic Institute and the CU-Boulder INSTAAR Laboratory for AMS Radiocarbon; all other preparation of the samples were carried out by the CU-Boulder INSTAAR Laboratory for AMS Radiocarbon Preparation and Research, University of Colorado at Boulder, USA. Mu sample was processed by the Leibniz-Labor für Altersbestimmung und Isotopenforschung, Universität Kiel Leibniz-Laboratory for Radiometric Dating and Stable Isotope Research Kiel University, Germany. Dates were made from the humic acid fraction of the sediment, which tends to provide more reliable ages for this kind of materials (Pessenda *et al.*, 2001). The results obtained are given in Table 1 depicting the uncalibrated and calibrated ages using the "Calib radiocarbon calibration program" (Stuiver and Reimer, 1993) and the calibration data set assembled by Reimer and colleagues (2013).

AMS essays from the lower portion of the QC and Mu sections dated both sites to the Middle Holocene, while the sample from ET yielded an age spanning the Pleistocene-Holocene transition conventionally established at 10.0 ka BP (Dawson, 1992). ET date is coincident with

the age of the archaeological finds belonging similar stratigraphic position in the area and other parts of South America (Nami, 2002, 2007; Maggard and Dillehay, 2011); however, QC and Mu results might represent minimum age for the deposits.

## Paleomagnetic study

### Sampling procedures

Paleomagnetic samples were vertically taken using 2.5 cm long and 2 cm diameter cylindrical plastic containers. At QC and ET the cylinders were carefully pushed into the sediments overlapping the next one about 50% each in the way illustrated in figure 2c, while in Mu the interval was ~2-3 cm (Figure 2b). Their orientation was measured using a Brunton compass. Samples were consolidated with sodium silicate once removed and finally, they were numerated from the top to the bottom. This sampling technique allows obtaining detailed paleomagnetic records and therefore, it is highly useful for the definition of short time excursions (Clement and Kent, 1984).

Following the interval described above and illustrated in figure 2c, at QC the sampling ( $n = 49$ ) was taken between 0.72 m and 1.89 m depth in the following levels: I (samples QC1 1 to 10), III (QC1 11 and 12), V (QC13 and 14), VII (QC15 to 24), VIII (QC25 to 33) and IX (QC34 to 49). Sand layers II, IV and VI were not sampled due to the presence of coarse elements. Mu Sampling ( $n = 25$ ) was performed between -1.26 and 1.90 m below the present vegetal soil. At ET, two samplings sites identified as ET1 ( $n = 22$ ) and ET2 ( $n = 20$ ) were taken each 30 cm each other. For comparative purposes and to cross check the section magnetic behavior according to depth, an additional sample (ET3 1) was taken approximately 30 meter below the surface in a red level of cangagua. Samples from ET were

taken as follows: ET1 1 and 2 and ET2 1 to 3 from level I, ET1 3 to 6 and ET2 4 to 6 in level II while ET1 7 to 22 and ET2 7 to 20 from level III. Sediment near the surface was not sampled because it was highly disrupted by plant roots and there was evidence of recent archaeological pottery remains.

*Laboratory analysis and results*

All samples were subjected to detailed stepwise alternating field (AF) demagnetization in progressive steps of 3, 6, 9, 12, 15, 20, 25, 30, 40 and 60 mT with a 3-axis static degausser attached 2G cryogenic magnetometer (755 R). Additional steps of 80 and 100 mT were used in some samples. The characteristic directions were calculated using principal components' analysis (Kirschvink, 1980). Paleomagnetic data were processed with the "Interactive analysis of palaeomagnetic data" (Torsvik, 1992) and MAG88 (Oviedo, 1989) computer programs. Some cores were not processed because their orientation marks were lost (e.

g. QC20 to 23, ET1 9 and ET2 1, 2 and 15) or were highly unstable to isolate directions (Mu13, 19 and 21).

Following are the results for each section: QC specimens showed similar magnetic behavior with less of 10 % of the NRM remained at field of 60 mT. The majority of the samples display linear demagnetization plots in with a Characteristic remanent magnetization (ChRM) that could be defined trending in the vector diagrams (Zijderveld, 1967) towards the origin (e.g., QC6, 38, 48, figure 3a, c, e); A few samples present two components with the second one decaying to the origin in the vector projection diagrams (e.g., QC12, 42, figure 3b, d), with a soft viscous component removed at 3 mT (e.g., QC42, Figure 3d). The cores show normal directions with steep inclinations with north-easterly directions (e.g., QC38, Figure 3c).

Mu cores exhibited a different behavior with less than 10 % of the remanence at 25 mT

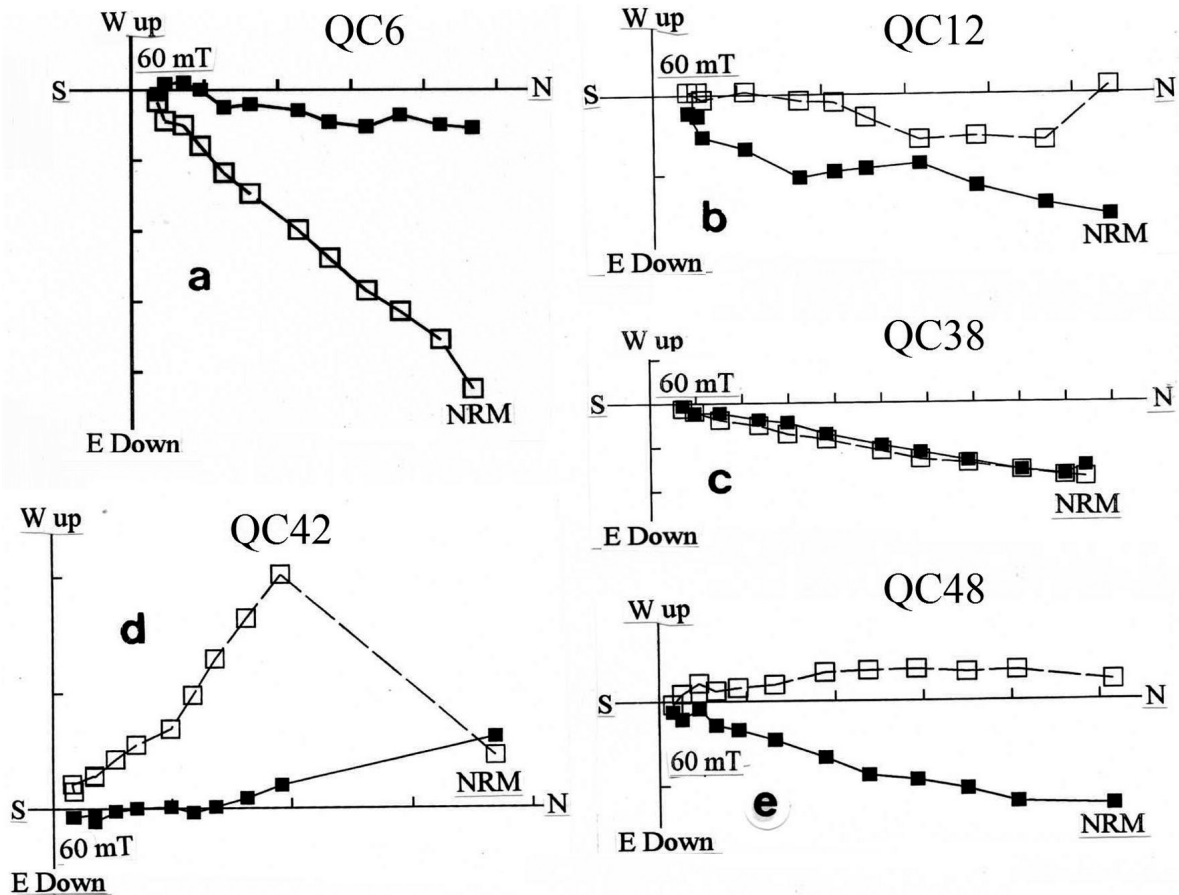


**Figure 3.** Typical Zijderveld diagrams of stepwise demagnetization of five samples with normal polarity from Quito City.

(Mu25, Figure 4f), 40 mT (Mu4, 17, Figure 4b, d), 60 mT (Mu1, Figure 4a) and 100 mT (Mu24, Figure 4e). There are univectorial samples (e. g., Mu4, Figure 4b), other ones with two vectors (e. g. Mu1, 17, Figure 4a, d), and finally a few specimens recorded three magnetic components, one of them with southwesterly direction (Mu24, Figure 4e).

ET samples showed a common pattern with similar reliable magnetic behavior. Some of them have a sudden drop with less than 10 % of the remanence at 15 mT (e. g., ET1 5, 17, ET2 16, Figure 5a, d, h), 25 mT (e. g. ET3 1, Figure 5i), 30 mT (e. g. ET1 13, 14, Figure 5b-c), 40 mT (ET2 6, Figure 5f), and 60 mT (ET2 3, 10, Figure 5e, g). Most secondary components were a soft viscous magnetization that was easily removed between 3 and 12 mT. In most cases, a ChRM could be defined trending in the Zijderweld diagrams towards the coordinate's origin (e.g., ET1 5, 17, ET2 10, 16, Figure 5a, d, g-h). A scarce number of specimens had two components with the second one decaying to the origin in the VDP (ET2 6, Figure 5f). Except ET3 1 that yielded a normal direction (Figure 5i), reversed or "anomalous" southward directions were found at the majority of ET1 and ET2 cores (e. g. ET1 5, 13, 17, ET2 3, 6, 10, 16, Figure 5a-b, d-h); Two samples (ET1 13 and ET2 11) exhibit easterly directions (Figure 5c).

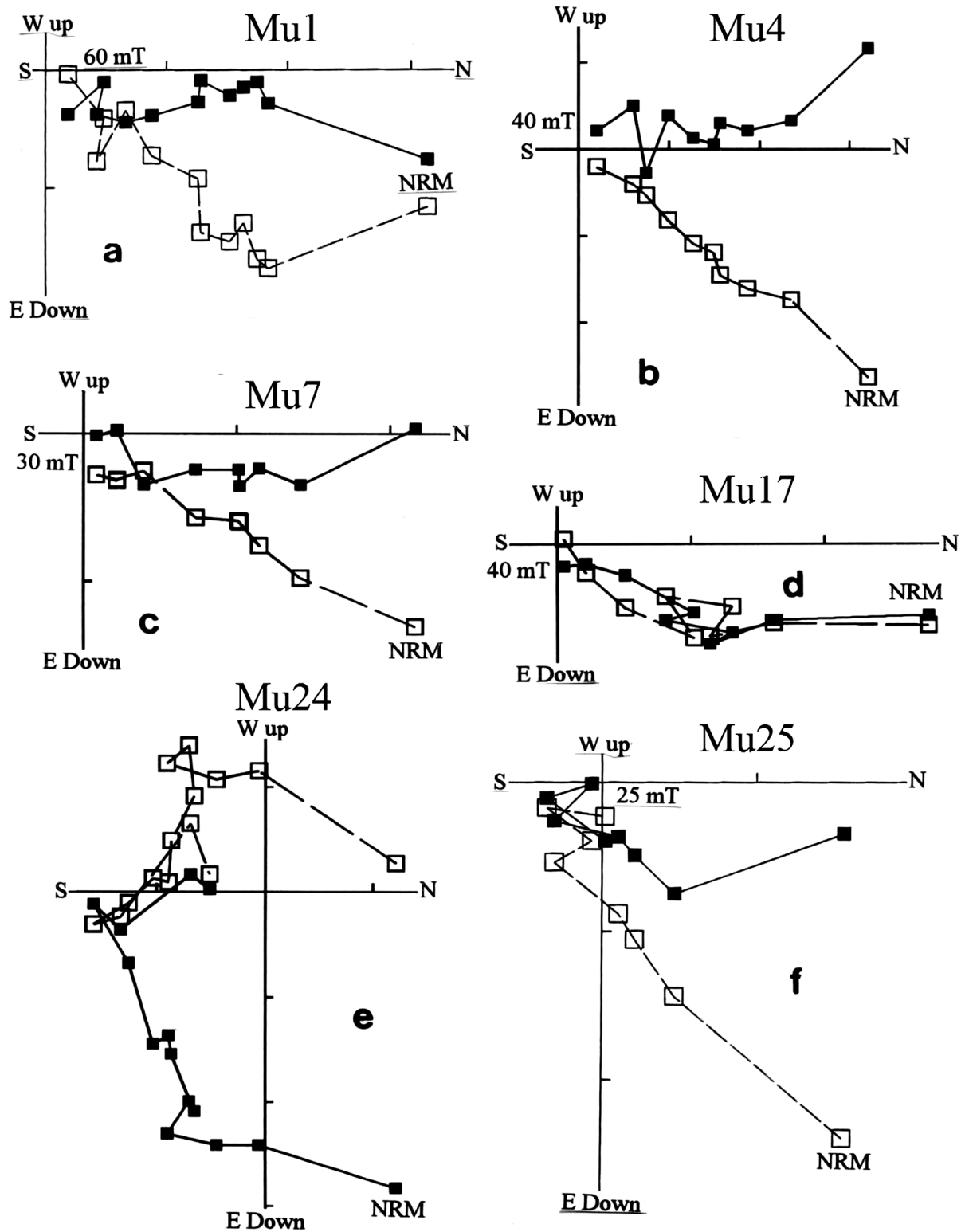
Samples with less 10 % of the NRM remaining at 60 mT from the analyzed sites suggest titanomagnetite as the dominant carrier of the NRM (Nagata, 1961; Stacey and Banerjee, 1974; Tarling, 1983; Thompson and Oldfield, 1986). The number and intervals of demagnetization steps used to isolate the ChRM of each site are depicted in the appendix.

The stereographic projection of each locality is illustrated in figure 6. QC displays normal GMF direction; despite that most of the samples at Mu display normal polarities, there are also intermediate directions which are considered in this way when departure from the mean is greater than 30° (Quidelleur and Valet 1996). Surprisingly at ET, both sites yielded strongly similar reverse records. Magnetograms of stratigraphic presentation of the declination and inclination profiles from each site are exhibited in Figures 7 to 9. QC shows stable logs with a gentle positive to negative inclination from ~40° to 10° (Figure 7). Mu shows wide amplitude pulses both in declination and inclination with normal and intermediate directions with transitional positive to negative inclination values and wide amplitude pulses between normal declinations

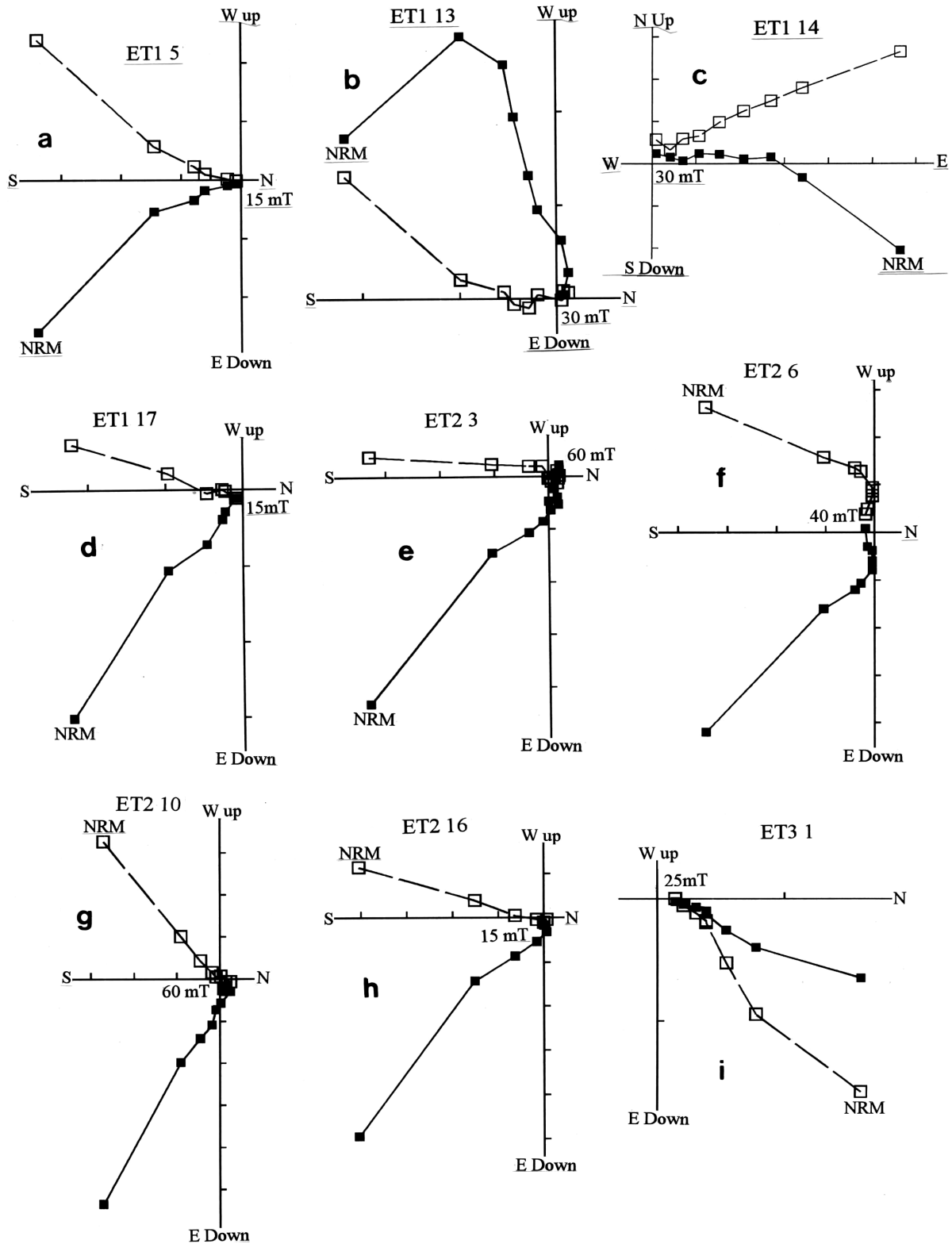
(Figure 8). It also present a ~90° westward declination swing and a strong fluctuating inclination shifting from positive to negative values from ~40 to 70° which are showed between dashed lines and pointed with an arrow in Figure 8. Remarkably is that ET1 and ET2 showed reverse directions with a similar wide fluctuation of ~90° represented by one sample (ET1 10 and ET2 9) in each site. Figure 10 exhibit the overlapped stratigraphic presentation of both sections related with <sup>14</sup>C date and depth.

Figure 11 depicts the stereoplots of virtual geomagnetic pole (VGP) positions calculated from the directions isolated of each section. When plotted in a present world map, VGPs calculated from normal samples at QC are very well clustered in Northern North America, Greenland and Northern Europe (Figure 12a); most VGP's calculated from Mu are situated between 30° and 60° northern latitude in Northern North America, Greenland, western Europe, Africa and North Pacific Ocean (Figure 12b). Interestingly, the majority of the reverse directions from ET conforms a patch located in southern Africa, and finally, a few ones are situated in central Africa, eastern Australia and Antarctica (Figure 12c-d). Figure 12e illustrate the totality of VGPs calculated from the Ecuadorian sites presented in this paper, positions that agree well with VGPs observed in previous paleomagnetic studies performed on sections of similar age from Argentina and Chile (Nami, 1995, 1999a, 2012, 2013). Finally, VGPs sited on South America also occurred in other paleomagnetic records of comparable age. In northern Europe, several varved cores from Björkeröds Mosse lake exhibit low latitude VGPs located in western Africa during the Pleistocene/Holocene boundary (Mörner, 1977: 422). Their distribution shows strong similarities with the VGPs calculated for the Laschamp and Iceland basin excursions, dated at ~40 ka and ~180–220 ka respectively (Laj and Channel, 2007: Figure 5 and 8).

Finally, a mean geomagnetic pole called Ecu was calculated from QC and Mu, the sites with normal and intermediate directions. They were computed from all VGP's located within 40° window around the mean geomagnetic pole (cf. McElhinny *et al.*, 1974). Additional palaeopoles for the sites from North and southern South America was also determined. On of them, named "Eastern Argentina" (EA) was computed using poles from 6 localities situated in northeastern Argentina where transitional VGPs were computed (Nami, 1999a, 2006, 2012). Another paleopole was calculated from the Red Rock sites from California, Southwestern North



**Figure 4.** Vector components diagrams showing the behavior of typical samples cleaned using AF progressive demagnetization from Mullimica.



**Figure 5.** a-h) Typical Zijderveld diagrams of stepwise demagnetization of samples with reverse polarity from El Tingo 1 and 2, i) sample with normal direction from ET3.

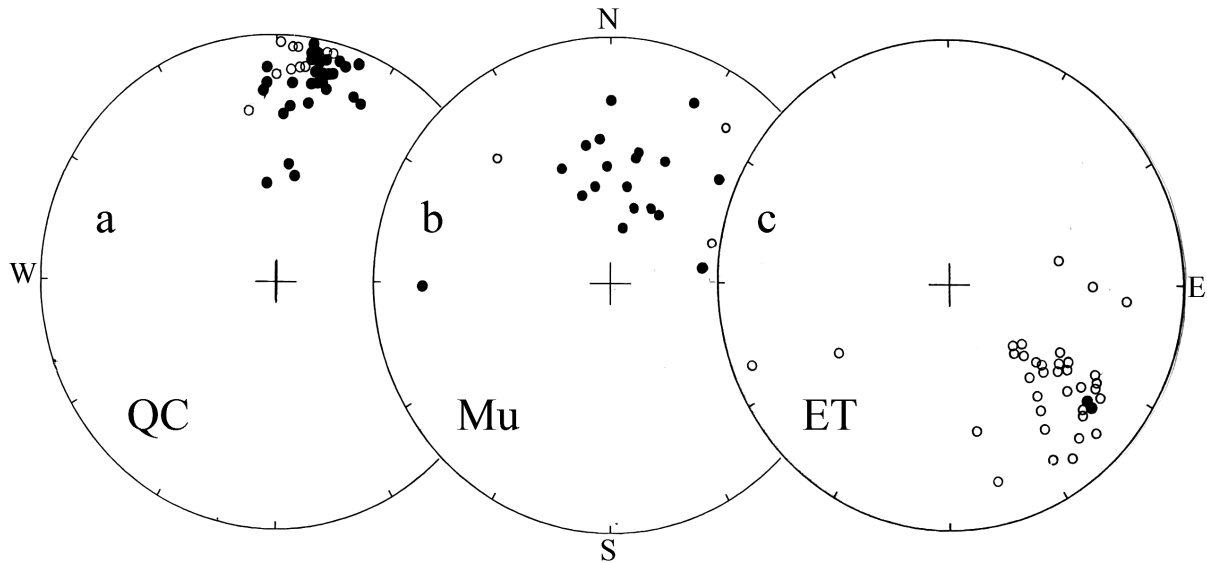
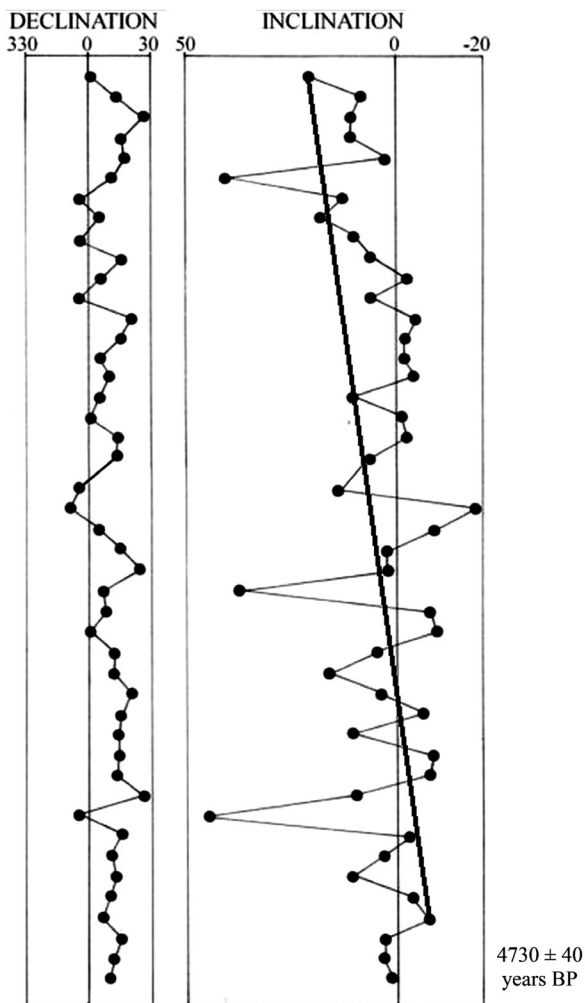


**Figure 6.** Stereoplots showing the directional data with field correction from QC (a), Mu (b) and ET (c). Solid and open circles represent positive and negative values, respectively).



America, where anomalous GMF directions were also recorded (Nami, 1999b). The totality of calculated paleopoles are depicted in Table 2. Finally, it was also used the previously published paleopole determined with the sites where the Mylodon excursion was computed ([ME= 336.7° W. Long., 68.65°S. La. with (A95) 8.2°], Nami 1999a). As observed in figure 13, they agree well, and as previously informed (Nami, 1999a, 2006, 2011; Mena and Nami, 2002), they do not agree with the geographical pole and shows ~15° angular difference in relation to the rotation's axis of the Earth. This suggest that a time span of 10.0/11.0 ka is insufficient to average out geomagnetic secular variation ([PSV], Hyodo *et al.*, 1993: 692; Nami, 1999a, 2006; Mena and Nami, 2002).

**Discussion**

New data obtained in sediments from different environments and lithologies cored in Pichincha province in Ecuador have been found to contain records that showed normal and anomalous GMF behavior. Normal directions were recorded in QC, while normal and intermediate polarity directions at Mu and, reverse VGPs at ET. QC and the upper portion of Mu correspond to the PSV Holocene record for Ecuador during the

**Figure 7.** Declination and inclination logs from QC. The line in the inclination shows the decreasing trend from ~-10° at the lower part to ~20° at the upper part.

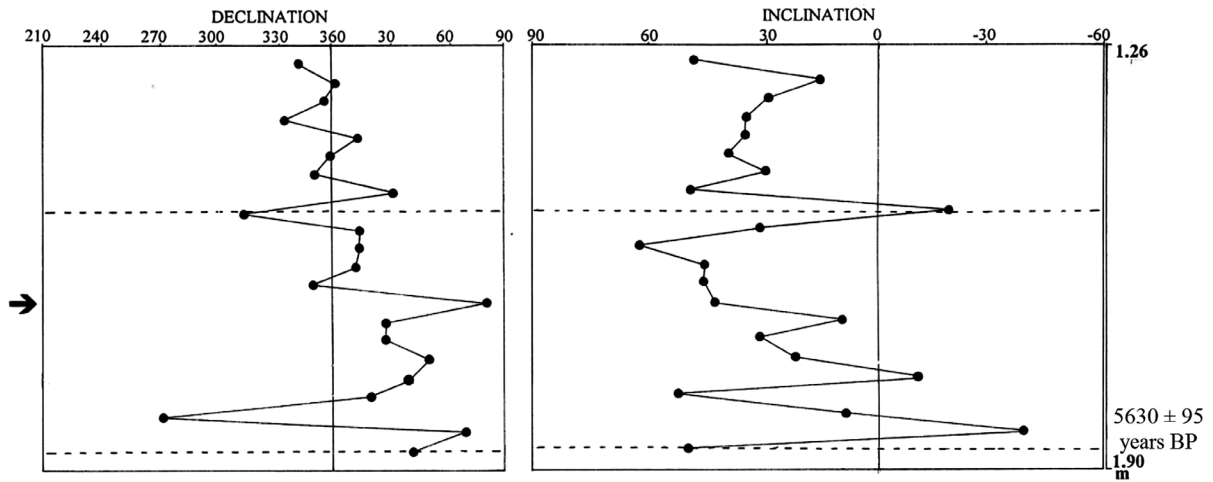


**Figure 8.** Stratigraphic plots of the declination and inclination profiles from Mu. The more conspicuous long direction and inclination departures are depicted between dashed lines and pointed with an arrow.

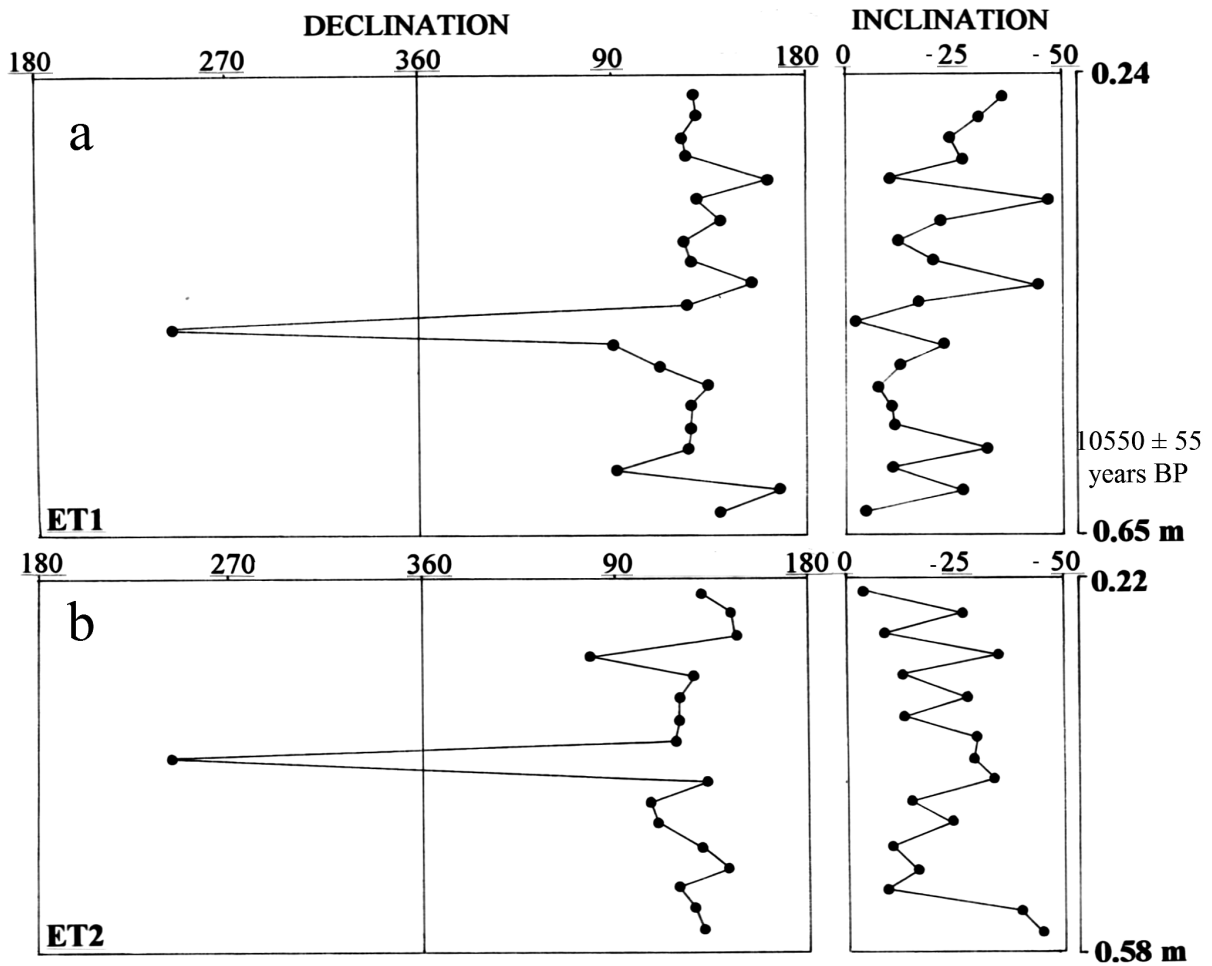


**Figure 9.** Stratigraphic presentation of the declination and inclination profiles from ET sites. a) ET1, b) ET2.

**Table 2.** Late Pleistocene/Holocene geomagnetic poles from Ecuador, northeastern Argentina and Red Rock locality in western North America calculated within 40° around the mean. References: n= number of samples, A95: semi-angle of cone 95% confidence, K: precision parameter (Fisher, 1953); r: resultant vector.

Section/Site	Sites (n)	Samples (n)	Long E. (°)	Lat. (°)	A95	R	K
Ecu	-	62	332.13	76.65	3.9	59.20	21.84
EA	6	-	336.62	78.47	9.1	5.9	59.4
RR	-	42	7.62	78.15	6.0	39.16	14.44

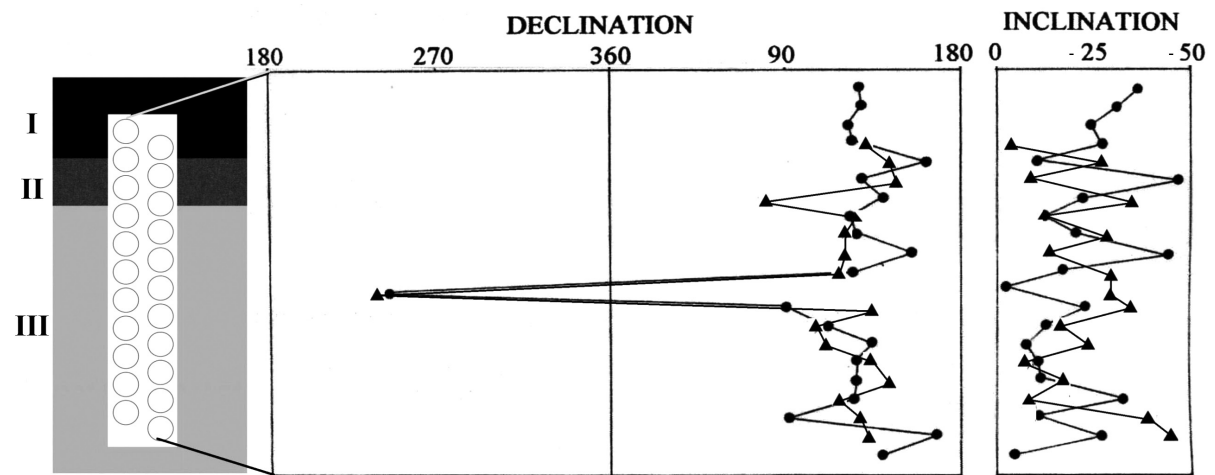


**Figure 10.** Overlapped stratigraphic display of ET1 and ET2 logs respectively represented by solid circles and triangles related with the direct absolute date by 14C. Roman numbers to the left indicates the geological layers.

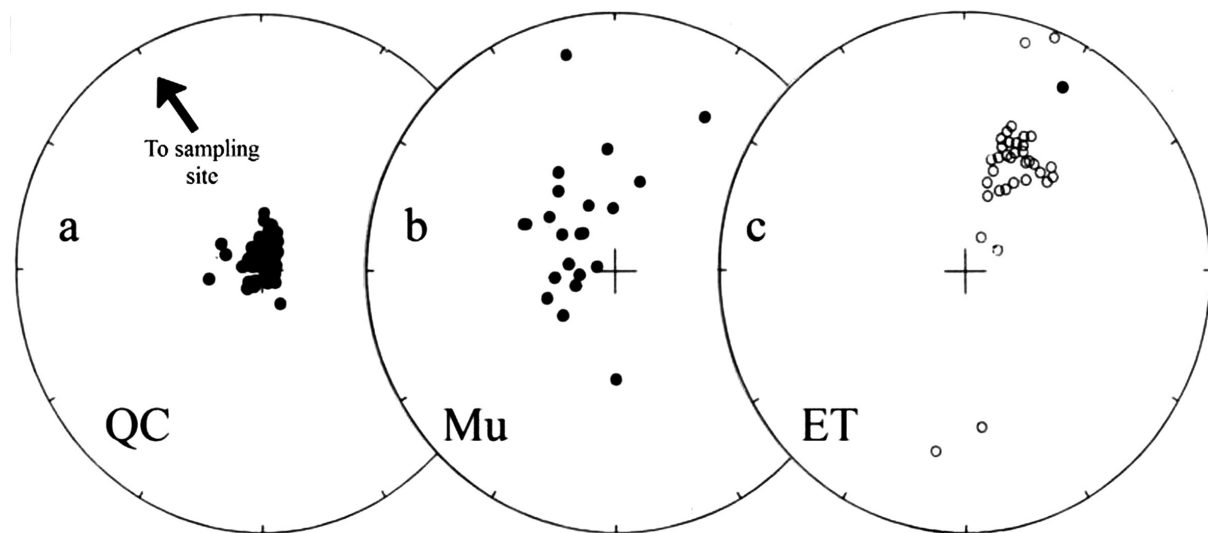


**Figure 11.** Stereographic projection of VGP calculated from directions of ChRM calculated from the sites mentioned in the text. Solid circles show those ones located in the Northern Hemisphere. The center of the projection is the geographic Southern Pole.

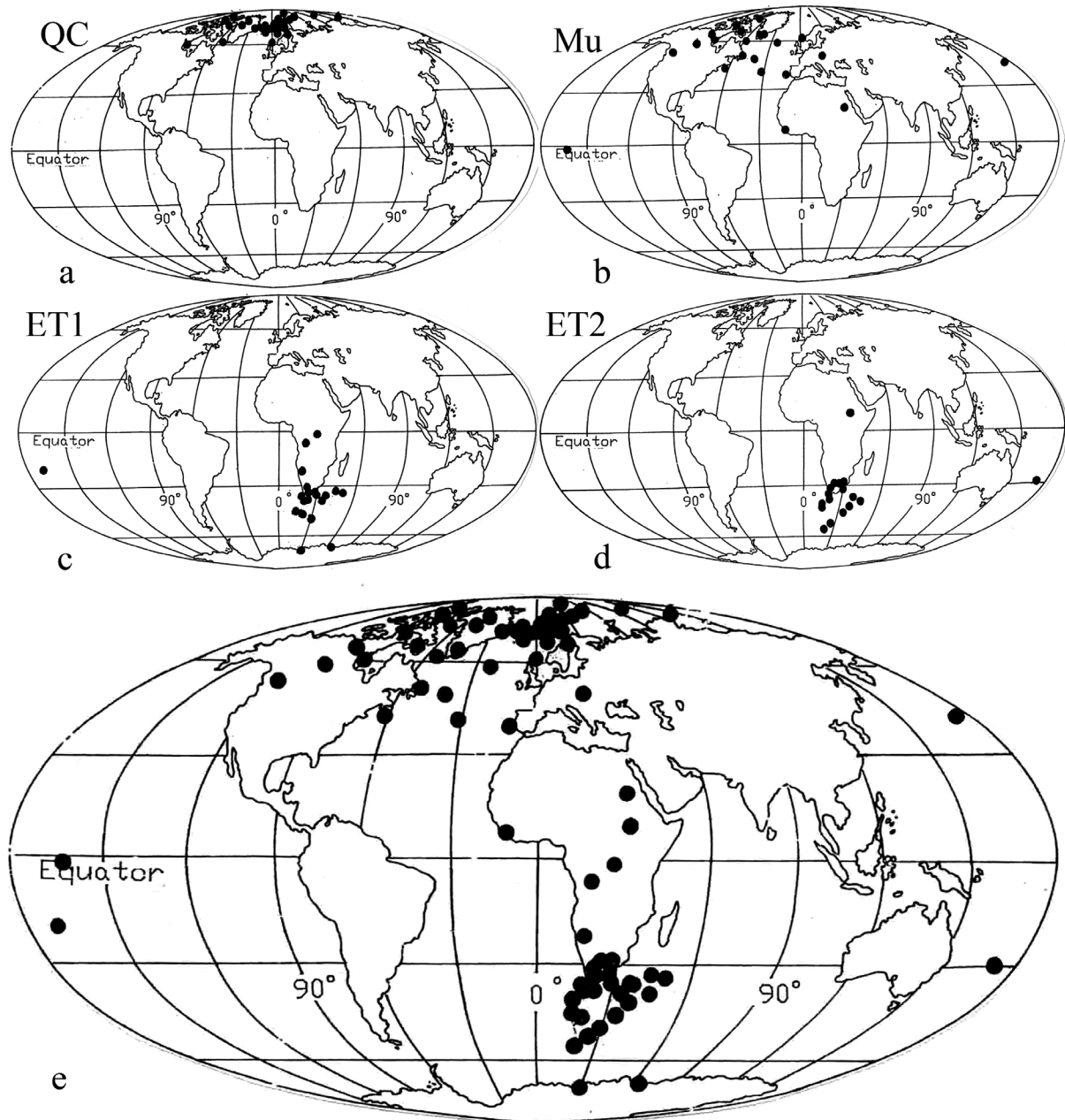


**Figure 12.** World map showing the location of the VGP obtained from the sites described in this paper (a-d) and the totality of VGPs from the Ecuadorian sites (e).

$\sim \leq 4.7$  ka BP; on the other hand, the lower portion of Mu logs represents the transition from normal to intermediate directions occurring at  $\sim \geq 5.6$  ka BP. Finally, sites from ET recorded two stable oblique reverse records with a large fluctuation far from the present GMF at  $\sim 10.5$  ka BP. The core from ET3 with normal direction might be consistent with the Brunhes chron normal polarity, suggesting that this part of the section may have  $< 700$  ka (Hailwood, 1989) and the Pleistocene age

of the deposit. Then, if the records presented here are not sediment artifacts (Langereis *et al.*, 1992; Quideller and Valet, 1994), ET corresponds to a PSV record that occurred during the reverse polarity position prevailed at Ecuador during the Pleistocene-Holocene transition at  $\sim 10.5$  ka BP. Mu sampling interval which is different to QC, might explain in part differences between magnetograms. Actually, the declination log at Mu shows a difference of  $90^\circ$  and a larger fluctuation of  $\sim 100^\circ$  in

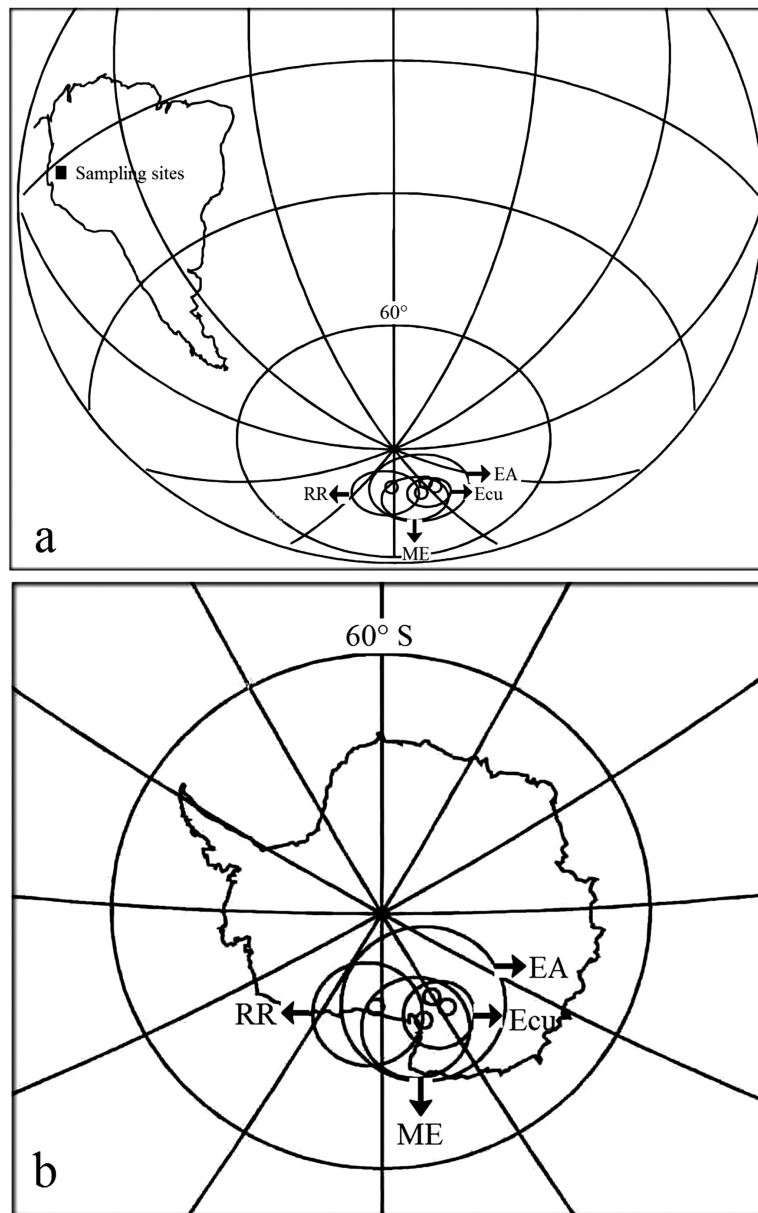


**Figure 13.** Projection showing the paleopole (Ecu) obtained with 40° filter and their confidence interval in relation with the paleopole obtained for the other sites with anomalous GMF directions from Northeastern Argentina (EA), North America (RR) and South America (ME) in relation with the sampling site (a) and the Antarctic continent (b).

inclination. Also some VGP from Mu and the totality of ET differ by more than 40–45° away from the geographic pole during normal or reverse polarity, signifying that they might be consider as a major deviation in GMF behavior over a relatively short period of geologic time (e.g., Wilson *et al.*, 1972; Cox, 1975; Barbetti and McElhinny, 1976; Verosub and Banerjee, 1977; Merrill and McElhinny, 1983; Thouveny and Creer, 1992; Jacobs, 1994; Merrill and Mc Fadden, 1994; Laj and Channel, 2007; Valet, 2008; Watkins, 1976). Hence, the anomalous directional data observed at Mu and ET, probably corresponds to different field excursions likely occurred at  $\sim 5.0$  and  $\sim 10.0$  ka BP. Actually,

large amplitude fluctuations with reverse and intermediate polarities were observed across the Americas during the middle Holocene at  $\sim 4\text{--}5\text{--}5.5$  ka BP in lava flows and sediments from diverse environments in Mexico and the Red Rock locality, California, USA (Gonzalez *et al.*, 1997, Urrutia-Fucugauchi *et al.* 1995, Nami 1999b); in southern South America a number of well date locales yielded records with intermediate and reverse directions, mainly at La Serranita site in northeastern Patagonia, Argentina directly dated at  $5300 \pm 40$  yr. BP (Nami, 2012, 2013). At the same time and in other parts of the world, large departures of the GMF were observed in Chinese fresh-water

sediments from Beijing that occurred between 5060 and  $4860 \pm 90$  yr. B.P (Zhu *et al.*, 1998), several cores from the Barents sea yielded records of the Solovki excursion dated at 4.5-7.5 ka BP (Guskova *et al.*, 2008).

During the terminal Pleistocene and its transition to the Holocene other anomalous directions were recorded in several sites and localities across the world (Table 3). In other areas of South America in Southern Chile, Mylodon cave yielded a stable record with intermediate and reverse directions registered at sediments consistently dated at  $\sim 11.0$ - $10.0$  and  $\sim 5.0$  ka BP (Nami, 1995). Furthermore, similar directions were recorded at Las Buitreras, Alero de las Circunferencias, and Barrancas de Maipú in Chile and Argentina (Nami, 1999a; Moreiras *et al.*, 2013). In North America, the Grandfather Lake in Alaska, yielded records with an excursion dated at the terminal Pleistocene and early Holocene dated between  $\sim 9.7$ - $11.7$

ka BP or  $\sim 11.8$ - $13.6$  Cal ka BP (Geiss and Banerjee, 2003); also, Creer and colleagues (1976) observed large GMF fluctuations at the Erieau Lake (Canada) in the time span under consideration. These anomalous directions might be contemporaneous to those excursions observed by Lund and associates (2008) at marine sediments of the Tahiti Coral Reef dated at 10.6 and 11.1 cal. ka BP and 12.6 and 13.2 cal. ka BP, other one observed at the South Pacific Ocean region at Tahiti, also dated a 12.5 cal. ka BP (Lund *et al.*, 2007) and, in West Coast South Island, New Zealand (Nelson *et al.*, 2009). Also, during the last millennium of the Pleistocene a number of PSV records in the northern Hemisphere, showed that despite the inclinations has the expected positive values, large amplitude swings in declination were recorded in Scandinavia and northern Russia (Backmutov, 1997; Backmutov *et al.*, 1994; Saarnisto and Sarinen, 2001).

**Table 3.** List of well dated records with anomalous GMF directions occurred during the last millennium of the Pleistocene and Pleistocene-Holocene transition. References: †: no given. To unify the results, all the available dates were calibrated using the "Calib radiocarbon calibration program" (Stuiver and Reimer, 1993) and the calibration data set assembled by Reimer and colleagues (2013). Calibrated ages are reported with 95.4 % ( $2\sigma$ ) cal age ranges.

Site	Environment	Material Dated	Uncalibrated AMS date yr BP	Calibrated age yr BP	Relative area under distribution	Reference
El Tingo	Continental	Sediment	$10550 \pm 55$	12254-12256	0.001	This paper
Grandfather Lake	Lacustrine	Wood	$9797 \pm 60$	11100-11331	1.00	Gneiss and Banerjee 2003
"	"	"	$11739 \pm 55$	13454-13718	1.00	"
Tahiti Coral Reef (younger excursion)	Marine	†	†	11600-11100	†	Lund <i>et al.</i> 2008
Tahiti Coral Reef (older excursion)	Marine	†	†	12600-13200	†	Lund <i>et al.</i> 2008
Alero de las Circunferencias	Continental	Charcoal	$9180 \pm 230$	10918-11089	0.05	Nami 1999a
"	"	"	$9190 \pm 110$	10612-10660	0.02	"
Barrancas de Maipú	Continental	Charcoal	$9180 \pm 120$	10051-10700	0.99	Moreiras <i>et al.</i> 2013

## Conclusions

The aforementioned anomalous GMF behavior occurred during the Pleistocene-Holocene transition and middle Holocene supports the hypothesis of the global excursions state of the GMF with not coetaneous intermediate and reverse directions during the last ~11.0 ka BP (Nami, 1999b, 2012, 2013). Hence, it might be expected that the Holocene GMF might have had a peculiar behavior with normal, intermediate and/or reverse polarity positions at the same time in different regions. In this sense, remarkably is the GMF model proposed by Brown and colleagues (2007) to explore the possible influence of the time-varying nondipole components during reversals and excursions. With that aim, they varied the magnitude of the axial dipole component in the model CALS7K.2 constructed by using paleomagnetic and archeomagnetic data of the last 7.0 ka BP (Korte and Constable, 2005). Resulting from their analysis, the authors suggest that non-dipole components could add significant structure to the GMF during the processes occurred in reversals and excursions which, in the latter, are neither global in extent nor synchronous in occurrence. Surprisingly, VGPs locations derived from the Brown and colleagues (2007: Figure 5) model agrees fairly well with the VGPs distribution observed in the likely excursions occurred during the last 11.0 ka BP at about 2.5, 5.0 and 10.0 ka BP (Nami, 1995, 1999a, 2012, 2013). Remarkably, the presence of VGP across Africa is coincident with the theoretical model developed by Gubbins (1987, 1994), who pointed out that beneath the South Atlantic Ocean, there is a "reverse flux" patch which is a source of magnetic anomalies, particularly in Africa (Bloxham and Gubbins 1985, Bloxham 1995). Therefore, if the paleomagnetic records informed in this paper truly reflect the GMF behavior, they might be related with these anomalies.

Finally, if the anomalous GMF behavior observed at ~10.5 ka BP represents a true excursion, it will become an excellent magnetostratigraphic marker for the Pleistocene-Holocene transition in certain parts of the world. In fact, as a dating tool, the excursion recorded at ET may be considered highly useful for dating materials and events formed and occurred during the Pleistocene-Holocene transition in the area surrounding the Ilaló hill in Ecuador. Repetition of denser sampling and supplementary precise dating is needed in order to gain a more detailed knowledge of the GMF behavior during the last 11.0 ka BP.

## Acknowledgments

I am deeply indebted to Ernesto Salazar and W. Mayer-Oakes (R.I.P.) for their continuous support of my work in the El Ilaló region and to Byron Camino for his friendship and invaluable help during the fieldwork. The University of Buenos Aires and CONICET for their support; H. Vizán for their continuous support and counseling during the processing and interpretation of the paleomagnetic data; G. Ré for his help; AMS dating was kindly provided by the NSF and IAI program for Latin American Quaternary research to global change studies; and by NSF grant ATM-9809285 to the University of Colorado INSTAAR - Laboratory for AMS Radiocarbon Preparation and Research. Jocelyn Turnbull was very helpful during the AMS date processing. Dr. Helmut Erlenkeuser, Leibniz-Labor für Altersbestimmung und Isotopenforschung, Universität Kiel Leibniz-Laboratory for Radiometric Dating and Stable Isotope Research Kiel University (Germany) for his invaluable help and understanding during the processing of the radiocarbon data. An anonymous reviewer and J. Urrutia Fucuguchi provided useful observations, help and cooperation during the edition of this paper.

## Bibliography

- Bakhmutov V., 1997, Secular variations of the geomagnetic field, indicated in Early Holocene deposits of Lake Ladoga. *Geophys. J.*, 16, 481-498.
- Bakhmutov V., 2006, The connection between geomagnetic secular variation and long-range development of climate changes for the last 13,000 years: the data from NNE Europe. *Quat. Int.*, 149(1), 4-11.
- Bakhmutov V., Yevzerov V., Kolka V., 1994, Geomagnetic secular variations of high-latitude glaciomarine sediments: data from the Kola Peninsula, northwestern Russia. *Phys. Earth. Planet. Inter.*, 85, 143-153.
- Barbetti M.F., McElhenny M.W., 1976, The Lake Mungo Geomagnetic Excursion. *Phil. Trans. R. Soc. Lond. A*, 281, 515.
- Bell R.E., 1965, Investigaciones arqueológicas en el sitio de El Inga, Ecuador. Casa de Cultura Ecuatoriana, Quito, 330 pp.
- Bloxham J., 1995, Global Magnetic Field. *Global Earth Physic. A Handbook of Physical Constants*, AGU Reference Shelf 1, pp. 47-65, American Geophysical Union, Washington D. C.

- Bloxham J., Gubbins P., 1985, The secular variations of Earth's magnetic field. *Nature*, 317, 777-781.
- Brown M.C., Holme R., Bargery A., 2007, Exploring the influence of the non-dipole field on magnetic records for field reversals and excursions. *Geophys. J. Int.*, 168, 2, 541-550, doi: 10.1111/j.1365-246X.2006.03234.x
- Burakow K.S., Nachasova I.E., 1990, Anomalous Behaviour of the Geomagnetic Field in the 1st thousand Years B.P. Geomagnetic Field in Quaternary. Zipe 62, 135-138, Akademie der Wissenschaften der DDR, Postdam.
- Clark H.C., Kennet J.P., 1973, Paleomagnetic Excursion recorded in Latest Pleistocene Deep-sea Sediments, Gulf of Mexico. *Earth Planet. Sci. Lett.*, 19, 267-274.
- Clement B.M., Kent D.V., 1984, Latitudinal dependency of geomagnetic polarity transition durations. *Nature*, 310, 488-491.
- Constable, C., Korte, M., 2006, Is Earth's magnetic field reversing? *Earth Planet. Sci. Lett.*, 246, 1-2, 1-16.
- Cox A., 1975, The frequency of geomagnetic reversals and the symmetry of the nondipole field. *Rev. Geophys.*, 13, 3, 35-51.
- Creer K.M., Anderson T.W., Lewis C.F.M., 1976, Late Quaternary geomagnetic stratigraphy recorded in the Lake Erie sediments. *Earth Planet. Sci. Lett.*, 31, 37-49.
- Dawson A.G., 1992, Ice Age Earth. Late quaternary Geology and Climate, Routledge, New York, 340 pp.
- Dergachev V.A., Raspopov O.M., van Geel B., Zaitseva G.I., 2004, The 'Sterno-Etrussia' Geomagnetic Excursion around 2700 BP and Changes of Solar Activity, Cosmic Ray Intensity, and Climate. *Radiocarbon*, 46, 2, 661-681.
- Dergachev V.A., Vasiliev S.S., Raspopov O.M., 2012, Climate Variations and the Shift of the Geomagnetic Poles of the Earth. Proceedings of the 9th Intl Conf. "Problems of Geocosmos", pp. 33-38, St. Petersburg.
- Fisher R.A., 1953, Dispersion on a Sphere. *Proc. R. Soc. Ser. A.*, 217, 295-305.
- Geiss C.E., Banerjee S.K., 2003, A Holocene-Late Pleistocene geomagnetic inclination record from Grandfather Lake, SW Alaska. *Geophys. J. Int.*, 153, 497-507
- Gonzalez S., Sherwood G., Bohnel H., Schnepf E., 1997, Palaeosecular variation in Central Mexico over the last 30 000 years: the record from lavas. *Geophys. J. Int.*, 130, 201-219.
- Gubbins D., 1987, Mechanism for geomagnetic polarity reversals, *Nature*, 326, 167-169.
- Gubbins D., 1994, Geomagnetic polarity reversals: A connection with secular variation and core-mantle interaction? *Rev. Geophys.*, 32, 1, 61-83.
- Guskova E.G., Raspopov O.M., Piskarev A.L., Dergachev V.A., 2008, Magnetism and Paleomagnetism of the Russian Arctic Marine Sediments. Proceedings of the 7th International Conference "Problems of Geocosmos", pp. 380-385, St. Petersburg.
- Hailwood E.A., 1989, The role of magnetostratigraphy in the development of geological time scales. *Paleoceanography*, 4, 1, 1-18.
- Head M.J., Zhou W., Zhou M., 1989, Evaluation of <sup>14</sup>C Ages of Organic Fractions of Paleosols from Loess-Paleosol Sequences near Xian, China. *Radiocarbon*, 31, 680-696.
- Hedges R.E.M., Gowlett J.A., 1986, Radiocarbon Dating by Accelerator Mass Spectrometry. *Sci. Am.*, 259, 1, 100-107.
- Herz N., Garrison E.G., 1998, Geological Methods for Archaeology, Oxford University Press, New York, 343 pp.
- Hyodo M., Itota C., Yaskawa K., 1993, Geomagnetic secular variation reconstructed from magnetizations of wide-diameter cores of Holocene sediments in Japan. *J. Geomag. Geoelectr.*, 45, 669-696.
- Jacobs J.A., 1994, Reversals of the Earth's Magnetic Field, Cambridge University Press, Cambridge, 339 pp.
- Kirschvink J.L., 1980, The least-squares line and plane and the analysis of palaeomagnetic data. *Geophys. J. R. Astr. Soc.*, 62, 699-718.

- Kochegura V.V., Pisarevsky S.A., 1994, Paleomagnetic Study of the Holocene and Late-glacial Sediments of the North-Western Russia. XXI International Union of Geodesy and Geophysics General Assembly. Boulder, USA, *Abstracts*, A173.
- Korte M., Constable C., 2005, The geomagnetic dipole moment over the last 7000 years - new results from a global model. *Earth Planet. Sci. Lett.*, 236, 1-2, 348-358,
- Korte M., Genevey A., Constable C.G., Frank U., Schnepf E., 2005, Continuous geomagnetic field models for the past 7 millennia: 1. A new global data compilation. *Geochem. Geophys. Geosyst.*, 6, 2, Q02H15, DOI:10.1029/2004GC000800. <http://www.agu.org/pubs/crossref/2005/2004GC000800.shtml>
- Kuznetsova N.D., Kuznetsov V.V., 2008, Implications of Volcanism and Geomagnetic Field Polarity Reversals into the Climate Variability, Proceedings of the 7th Conference "Problems of Geocosmos", pp. 146-151, St. Petersburg.
- Laj C., Channell J.E.T., 2007, Geomagnetic Excursions. In: *Treatise on Geophysics*, 5, pp. 373-416, Elsevier, Amsterdam.
- Langereis C.G., van Hoof A.A.M., Rochette P., 1992, Longitudinal confinement of geomagnetic reversal paths as a possible sedimentary artifact. *Nature*, 358, 228-230.
- Lund S.P., Platzman E., Thouveny N., Camoin G., 2007, Evidence for Two New Paleomagnetic Field Excursions ~2,500 and ~12,500 Years Ago from the South Pacific Ocean Region (Tahiti), AGU, Fall Meeting 2007, abstract #GP42A-05
- Lund S.P., Platzman E., Thouveny N., Camoin G., Yokoyama Y., Matsuzaki H., Seard C., 2008, Evidence for Two New Magnetic Field Excursions (11,000 and 13,000 Cal Yrs BP) from sediments of the Tahiti Coral Reef (Maraa tract), AGU, Fall Meeting 2008, abstract #GP21B-0786
- Maggard G., Dillehay T., 2011, El Palto Phase (13800-9800 BP). In: *From foraging to farming in the Andes: New perspectives on food production and social organization*, edited by T. Dillehay, pp. 77-94, Cambridge University Press, Cambridge.
- Mayer-Oakes W.J., 1963, Early Man in the Andes. *Sci. Am.*, 208, 5, 117-128.
- Mayer-Oakes W.J., 1966, El Inga projectile points-Surface collections. *Am. Ant.*, 31, 5, 644-661.
- Mayer-Oakes W.J., 1986, El Inga. A Paleoindian site in the Sierra of Northern Ecuador. *Transactions of the American Philosophical Society*, 76, 4, Philadelphia, 235 pp.
- Mayer-Oakes W.J., Bell R. 1960, Early Man Site Found Highland Ecuador. *Science*, 131, 1805-1806.
- McElhinny M.W., Embleton B.J.J., Wellman P., 1974, A Synthesis of Australian Cenozoic Palaeomagnetic Results. *Geophys. J. Roy. Astr. Soc.*, 36, 141-151.
- Mena M., Nami H.G., 2002, Distribución geográfica de PGV's Pleistoceno tardío-Holoceno obtenidos en Sedimentos de América del Norte y América del Sur. XXI Reunión Científica de Geofísicos y Geodestas, pp. 213-218, Buenos Aires.
- Merrill R.T., Mc Elhinny M.W., 1983, *The Earth's Magnetic Field: Its History, Origin and Planetary Perspective*, Academic Press, New York, 401 pp.
- Merrill R.T., McFadden P.L., 1994, Geomagnetic field stability: Reversal events and excursions. *Earth Planet. Sci. Lett.*, 121, 57-69.
- Moreiras S.M., Marsh E., Nami H., Estrella D., Durán V., 2013, Holocene Geomorphology, Tectonics, and Archaeology in Barrancas, Arid Central Andes piedmont (33° S). *Appl. Geogr.*, 42, 217-226.
- Mörner N.A., 1977, The Gothenburg Magnetic Excursion. *Quat. Res.*, 7, 3, 413-427.
- Nagata T., 1961, *Rock Magnetism*, Maruzen Ltd., Tokyo, 350 pp.
- Nami H.G., 1995, Holocene Geomagnetic Excursion at Mylodon Cave, Ultima Esperanza, Chile, *J geomag Geoelect*, 47, 1325-1332.
- Nami H.G., 1999a, Possible Holocene Excursion of the Earth's Magnetic Field in Southern South America: New Records from Archaeological Sites in Argentina. *Earth, Planets, Space*, 51, 175-191.

- Nami H.G., 1999b, Probable middle Holocene geomagnetic excursion at the Red rock archaeological site, California. *Geofís. Int.*, 18, 4, 239-250.
- Nami H.G., 2002, An AMS 14C Date from a Late Pleistocene Deposit in the Ilaló Region, Ecuador: Implication for Highland Paleoindian Occupation. *Cur. Res. Pleist.*, 19, 70-72
- Nami H.G., 2006, Preliminary paleomagnetic results of a terminal Pleistocene/Holocene record from northeastern Buenos Aires province (Argentina). *Geofizika*, 23, 2, 119-141.
- Nami H.G., 2007, Research in the Middle Negro River Basin (Uruguay) and the Paleoindian Occupation of the Southern Cone. *Cur. Ant.*, 48, 164-176.
- Nami H.G., 2011, New detailed paleosecular variation record at Santa Lucía archaeological site (Corrientes province, northeastern Argentina). *Geofísica Internacional*, 50, 2, 9-21.
- Nami H.G., 2012, New Detailed Holocene Paleomagnetic Records with Anomalous Geomagnetic Field Behavior in Argentina. *Geoacta*, 37, 2, 83-116.
- Nami H.G., 2013, Paleomagnetic Results from Argentinean Patagonia: New Evidence for the Holocene Geomagnetic Excursion in Southern South America. Geological Epochs, Acadeciaedu Publishers. In press.
- Nami H.G., Sinito A.M., 1991, Preliminary paleomagnetic results, the Campo Cerda Rockshelter, province of Chubut, Argentina. *Quat. South Am. Antarc. Peninsula*, 9, 141-151.
- Nami H.G., Sinito A.M., 1993, Evidence of a Possible Excursion of the Geomagnetic Field Registered during the Late Holocene in the Province of Chubut, Argentina. *Geoacta*, 20, 19-26.
- Nami H.G., Sinito A.M., 1995, Primeros resultados de los estudios paleomagnéticos en sedimentos de Cueva del Medio (Ultima Esperanza, Chile). *Ans. Inst. Pat. S. Cs. H.*, 23, 135-142.
- Nelson F.E., Wilson G.S., Shipboard party, 2009, Environmental magnetism and excursion record of the Pleistocene-Holocene transition in marine cores, West Coast South Island, New Zealand. *Geophys. Res. Abstracts*, 11, EGU2009-430.
- Ortega-Guerrero B., Urrutia-Fucugauchi J., 1997, A Paleomagnetic Secular Variation Record from Late Pleistocene-Holocene Lacustrine Sediments from Chalco Lake, Basin of Mexico. *Quat. Int.*, 43/44, 87-96.
- Oviedo E.S., 1989, Un Sistema de Computación para Análisis de Datos Paleomagnéticos, su Aplicación al Estudio de Datos Paleomagnético de Sedimentos de la Cuenca Neuquina. Doctoral dissertation, FCEfyN, University of Buenos Aires, 178 pp.
- Parkes P.A., 1986, Current Scientific Techniques in Archaeology, St. Martin's Press, New York, 271 pp.
- Pessenda L.C.R., Gouveia S.E.M., Aravena R., 2001, Radiocarbon Dating of Total Soil Organic Matter and Humin Fraction and its Comparison with 14C Ages of Fossil Charcoal. *Radiocarbon*, 43, 2B, 595-601.
- Petrova G.N., Pospelova G.A., 1990, Excursions of the magnetic field during the Brunhes chron. *Phys. Earth Planet. Inter.*, 63, 135-143.
- Platzman E.S., Lund S., Camoin G., Thouveny N., 2010, Geomagnetic Secular Variation Determined from Paleomagnetic Observations in Late Quaternary (8-16,000 YBP) Carbonates From The South Pacific Ocean Abstract presented at 2010 Fall Meeting, AGU, San Francisco, Calif., 13-17 Dec.
- Quidelleur X., Valet J.P., 1994, Paleomagnetic records of excursions and reversals: possible biases caused by magnetization artefacts. *Phys. Earth Planet. Int.*, 82, 27-48.
- Quidelleur X., Valet J.P., 1996, Geomagnetic changes across the last reversal recorded in lava flows from La Palma, Canary Islands. *J. Geophys. Res.*, 101, 13,755-13,773.
- Raspopov O.M., Dergachev V.A., Goos'kova E.G., 2003, Ezekiel's vision: Visual evidence of Sterno-Etrussia geomagnetic excursion? *Eos, Transactions AGU*, 84, 9, 77-83 (84: doi: 10.1029/2003EO090001)
- Raspopov O.M., Dergachev V.A., Goos'kova E.G., Mörner N.A., 2003, Visual Evidence of the Sterno-Etrussia Geomagnetic Excursion (2700 BP)? *Geophys. Res. Abs.*, 5.

- Reimer P.J., Bard E., Bayliss A., Beck J.W., Blackwell P.G., Ramsey C.B., Buck C.E., Cheng H., Edwards R.L., Friedrich M., Grootes P.M., Guilderson T.P., Hafliðason H., Hajdas I., Hatté C., Heaton T.J., Hoffmann D.L., Hogg A.G., Hughen K.A., Kaiser K.F., Kromer B., Manning S.W., Niu M., Reimer R.W., Richards D.A., Scott E.M., Southon J.R., Staff R.A., Turney C.S.M., van der Plicht J., 2013, Intcal13 and Marine13 Radiocarbon Age Calibration Curves 0–50,000 Years Cal Bp. *Radiocarbon*, 55, 4, 1869–1887.
- Roberts N., Piper J.D.A., 1989, A Description of the Behaviour of the Earth's Magnetic Field. In: *Geomagnetism*, edited by J. A. Jacobs, 3, pp. 163-260, Academic Press, New York.
- Saarnisto M., Saarinen T., 2001, Deglaciation chronology of the Scandinavian Ice Sheet from the Lake Onega Basin to the Salpausselkä End Moraines. *Global Planet. Ch.*, 31, 387-405.
- Salazar E., 1980, Talleres Prehistóricos en los Altos Andes del Ecuador, Publicación del Departamento de Difusión de la Universidad de Cuenca, Cuenca, 132 pp.
- Sauer W., 1965, Geología del Ecuador, Editorial del Ministerio de Educación, Quito, 383 pp.
- Scharpenseel H.W., 1971, Radiocarbon Dating of Soils-Problems, Troubles, Hopes. In: *Paleopedology. Origin, Nature and Dating*, edited by D. H. Yaalon, pp. 77-88, International Society of Soil Scientists and Israel University Press, Jerusalem.
- Scharpenseel H.W., 1976, Soil Fraction Dating. In: *Radiocarbon Dating. Proceedings of the Ninth International Conference, Los Angeles and La Jolla*, edited by R. Berger and H.E. Suess, pp 277-283, University Of California Press, Los Angeles.
- Scharpenseel H.W., Schiffmann H., 1977, Soil radiocarbon analysis and soil dating. *Surv. Geophys.*, 3, 2, 143-156.
- Sinito A.M., Nami H.G., Gogorza C., 1997, Analysis of Palaeomagnetic Results from Holocene Sediments Sampled at Archaeological Excavations in South America. *Quat. South Am. Antarc. Peninsula*, 10, 31-44.
- Sinito A.M., Gogorza C., Nami H.G., Irurzun M.A., 2001, Observaciones Paleomagnéticas en el Sitio Arqueológico Puesto Segundo (Misiones, Argentina). *An. Asoc. Fís. Arg.*, 13, 237-241.
- Stacey F.D., Banerjee S.K., 1974, *The Physical Principles of Rock Magnetism*, Elsevier, Amsterdam, 195 pp.
- Stein J.K., 1992, Organic Matter in Archaeological Contexts. In: *Soils in Archaeology*, edited by V. T. Holliday, pp. 193-216, Smithsonian Institution Press, Washington D. C.
- Stuiver M., Reimer P.J., 1993, Extended 14C data base and revised CALIB 3.0 14C age calibration program. *Radiocarbon*, 35, 1, 215-230.
- Tarling D., 1983, *Paleomagnetism*, Chapman and Hall, New York 379 pp.
- Taylor R.E., 1997, Radiocarbon Dating. In: *Chronometric Dating in Archaeology*, edited by R. E. Taylor and J. Aiken, pp. 65-96, Plenum Press, New York and London.
- Thompson R., 1991, Paleomagnetic Dating. In: *Quaternary Dating Methods. A User Guide*, edited by Smart, P.L. and Frances, P.D., Quaternary Research Association (Great Britain), Technical guide 4, Cambridge, 233 pp.
- Thompson R., Oldfield F., 1986, *Environmental Magnetism*, Allen and Unwin, London, 227 pp.
- Thouveny N., Creer K.M., 1992, Geomagnetic excursions in the past 60 ka: Ephemeral secular variation features. *Geology*, 20, 399-402.
- Torsvik T., 1992, IAPD, Interactive analysis of Palaeomagnetic Data. Manual. NGU, N-7002, Trondheim, 51 pp.
- Urrutia-Fucugauchi J., Lozano-García S., Ortega-Guerrero B., Caballero Miranda M., 1995, Palaeomagnetic and palaeoenvironmental studies in the southern basin of Mexico-II Late Pleistocene-Holocene Chalco lacustrine record. *Geofísica Internacional*, 34, 33-53.
- Valet J., 2008, Field Excursions and Reversals: Observational Constraints. AGU, Spring Meeting, abstract #GP33A-03
- Wang Y., Amundson R., Trumbore S., 1996, Radiocarbon Dating of Soil Organic Matter. *Quat. Res.*, 45, 282-288.

- Watkins N., 1976, Polarity group sets up guidelines. *Geotimes*, 21, 18-20.
- Westaway R., 2003, The Effect of Changes in the Earth's Moment of Inertia During Glaciation on Geomagnetic Polarity Excursions and Reversals: Implications for Quaternary Chronology. *Curr. Sci.*, 84, 1105-1115.
- Willey K.L., Johnson W.C., Isaacson J.S., 1998, Preservation of the Paleoindian record in Alluvial Fill, Northeastern Kansas. *Cur. Res. Pleist.*, 15, 68-70.
- Wilson R.L., Dagley P., McCormack A.G., 1972, Paleomagnetic evidence about the source of the geomagnetic field. *Geophys. J. R. astr. Soc.*, 28, 213-224.
- Zhu R.X., Coe R.S., Zhao X.X., 1998, Sedimentary record of two geomagnetic excursions within the last 15,000 years in Beijing, China. *J. Geophys. Res.*, 103(B12), 30323-30334.
- Zijderveld J.D.A., 1967, AC demagnetization of rocks: Analysis of results. In: *Methods in Paleomagnetism*, edited by Collinson, D.W., Creer, K. M., Runcorn, S. K., pp. 254-286, Elsevier, Amsterdam.

---

Appendix. Characteristic remanent magnetization, virtual geomagnetic pole positions, and intervals of each sample. Negative values show negative inclination or VGP located in the Southern Hemisphere. Intervals of selected ChRM are given in mT. References: D: Declination, I: Inclination, Long.: Longitude, Lat.: Latitude, Int.ChRM: Intervals of selected ChRM, Or.: Origin in the Zijderveld diagram.

QC						Sample	D°	I°	Long. E	Lat.	Int.ChRM
Sample	D°	I°	Long. E	Lat.	Int.ChRM	7	349	30	249	70	0-20
1	2	21	292	78	3-60	8	32	50	323	47	0-20
2	14	9	353	75	3-Or.	9	315	-18	179	44	0-40
3	28	11	360	61	3-30	10	14	32	319	68	0-Or.
4	16	43	312	61	0-25	11	15	63	297	43	25-Or.
5	18	3	7	72	3-30	12	12	46	304	60	0-30
6	11	42	305	68	9-Or.	14	351	46	265	61	0-Or.
7	356	13	251	82	0-Or.	15	81	43	347	8	25-Or.
8	5	18	310	79	3-Or.	16	28	10	1	62	0-15
9	357	11	254	84	3-Or.	17	27	31	338	58	12-Or.
10	17	7	359	73	3-Or.	18	50	23	356	39	0-12
11	6	-2	28	83	3-Or.	20	40	-10	19	50	12-Or.
12	357	7	242	85	0-Or.	22	20	53	309	51	0-15
13	20	-4	17	70	3-Or.	23	269	9	196	-1	30-60
14	16	-2	15	74	3-Or.	24	70	-37	34	19	9-60
15	5	-2	22	85	0-Or.	25	40	50	329	41	3-20
16	10	-4	23	80	6-Or.	ET1					
17	5	11	323	82	0-Or.	Sample	D°	I°	Long. E	Lat.	Int.ChRM
18	1	-1	33	88	0-50	1	129	-36	37	-36	0-Or.
19	14	-2	15	76	3-60	2	129	-31	33	-37	0-Or.
20	15	7	358	75	0-40	3	123	-24	27	-32	0-Or.
21	358	-5	244	87	0-50	4	125	-27	29	-34	0-15
22	27	28	341	53	3-25	5	164	-10	30	-73	9-Or.
23	353	8	222	82	0-12	6	130	-48	48	-34	0-Or.
24	12	7	355	77	9-60	7	141	-22	30	-50	0-15
25	355	14	247	81	6-40	8	127	-12	19	-37	0-15
26	350	-19	147	76	6-20	10	129	-20	25	-38	0-30
27	4	-8	56	84	9-25	11	156	-45	44	-32	3-30
28	14	3	5	72	3-Or.	12	125	-17	23	-35	0-Or.
29	23	2	9	67	3-25	13	250	-2	191	-20	3-30
30	6	38	297	68	3-30	14	91	-23	24	-1	6-30
31	7	-7	38	82	3-50	15	121	-13	20	-31	0-15
33	0	-9	102	86	3-60	16	136	-8	18	-45	0-Or.
34	12	5	359	78	0-Or.	17	127	-11	19	-37	0-Or.
35	11	17	333	76	0-60	18	130	-12	20	-40	0-15
36	20	4	6	70	6-Or.	19	128	-33	34	-36	0-20
37	15	-6	23	75	0-Or.	20	95	-11	17	-5	0-20
38	11	11	344	78	3-Or.	21	168	-27	63	-71	3-15
39	13	-8	24	77	0-Or.	22	141	-5	16	-51	0-Or.
40	12	8	353	77	0-60	ET2					
41	25	10	360	65	3-Or.	Sample	D°	I°	Long. E	Lat.	Int. ChRM
42	354	45	270	63	3-Or.	3	132	-5	15	-42	0-30
43	13	-3	18	77	0-50	4	138	-27	33	-46	0-30
44	10	3	2	80	0-60	5	146	-8	19	-56	0-Or.
45	12	11	346	77	3-Or.	6	79	-35	31	10	12-30
46	10	-4	22	80	3-60	7	127	-13	20	-37	0-25
47	8	-7	35	81	3-Or.	8	123	-28	29	-32	0-30
48	15	-3	17	72	0-Or.	9	122	-13	20	-32	0-15
49	11	3	3	79	0-Or.	10	119	-30	30	-28	0-Or.
50	10	1	8	80	3-Or.	11	241	-30	173	-28	12-30
Mu						12	135	-34	37	-42	0-20
Sample	D°	I°	Long. E	Lat.	Int. ChRM	13	119	-15	21	-29	0-15
1	341	48	252	56	6-30	14	120	-25	27	-29	0-20
2	1	16	289	82	0-50	16	131	-11	19	-41	0-Or.
3	356	29	268	74	0-60	17	143	-17	26	-52	0-20
4	335	35	232	59	0-30	18	124	-10	18	-34	0-Or.
5	14	35	316	66	3-50	19	130	-41	41	-36	0-Or.
6	359	39	279	68	0-50	20	133	-46	47	-37	0-30

# Source Model of the October 9, 1995 Jalisco-Colima Tsunami as constrained by field survey reports, and on the numerical simulation of the tsunami

Elizabeth Trejo-Gómez\*, Modesto Ortiz and Francisco Javier Núñez-Cornú

Received: October 11, 2013; accepted: June 17, 2014; published on line: March 31, 2015

## Resumen

En este trabajo se modela la fuente sísmica del tsunami de Jalisco-Colima del 9 de octubre de 1995 ajustando los resultados del modelo numérico del tsunami para reproducir adecuadamente las alturas de inundación del tsunami documentadas in situ durante los trabajos de reconocimiento del área afectada por el tsunami. La fuente sísmica corresponde a un sismo de magnitud  $M_w \sim 8.0$  con un área de ruptura  $A = 9000 \text{ km}^2$ ,  $L = 150 \text{ km}$ ,  $W = 60 \text{ km}$ , con dislocación cosísmica heterogénea: dislocación de 1 m en los primeros 60 km a lo largo del plano de falla iniciando en el extremo NW, mar adentro frente a Chalacatepec y Chamela, y dislocación de 3 m en los restantes 90 km, mar adentro frente a Tenacatita, Navidad y Manzanillo. Como se esperaba, la fuente sísmica obtenida en este estudio es un modelo simplificado en comparación con la obtenida invirtiendo datos sísmicos y de GPS. Sin embargo, el hecho de que este modelo simplificado reproduzca aproximadamente la dislocación cosísmica y el área de ruptura y su localización, es importante para validar la fuente sísmica de aquellos tsunamis históricos de los que únicamente se cuenta con algunos testimonios y relatos vagos de sus efectos y de los cuales no existen registros sísmicos ni del nivel del mar.

Palabras Clave: Tsunami Local, Bloque Jalisco, Costa sur de Jalisco.

## Abstract

A model of the seismic source of the October 9, 1995 Jalisco-Colima tsunami is obtained using the numerical modeling of the tsunami as constrained by field survey reports of tsunami run-up and the extent of flooding, by considering an earthquake ( $M_w \sim 8.0$ ) with rupture area  $A = 9000 \text{ km}^2$ ,  $L = 150 \text{ km}$ ,  $W = 60 \text{ km}$ , with two different coseismic dislocation patches: 1 m the dislocation of the first 60 km along the fault plane starting from its NW edge, offshore Chalacatepec and Chamela, and 3 m the dislocation of the next 90 km; offshore Tenacatita, Navidad and Manzanillo. As expected, the seismic source obtained in this study is a simplified model in comparison of the seismic source obtained by inverting seismic and GPS data. However, the fact that this simplified model reproduces adequately the location of the rupture area and its coseismic dislocation is still important in order to provide some degree of certainty for the tsunami source of those historical tsunamis for which no seismic nor tide records are available, and only testimonies and vague relates of its effects are documented.

Key words: Local Tsunami, Jalisco Block; Southern Coast of Jalisco.

---

E. Trejo\*  
F.J. Núñez-Cornú  
Centro de Sismología y Volcanología de Occidente  
Centro Universitario de la Costa  
Universidad de Guadalajara  
Avenida Universidad 203, C.P. 48200  
Ixtapa, Puerto Vallarta  
Jalisco, México  
*\*Corresponding author: elyt@cuc.udg.mx*

M. Ortiz  
Departamento de Oceanografía Física  
Centro de Investigación Científica  
y de Educación Superior de Ensenada

## Background

### *Tectonic frame*

In this region, the North-American, Pacific, and Rivera lithospheric plates are interacting and several models of triple junctions have been proposed, but the seismotectonic setting is still poorly understood. A tectonic unit known as the Jalisco block has been proposed in this region (Luhr *et al.*, 1985). The Jalisco block extends northward from the Colima graben, along the Pacific coast, and connects at its northern end with two other major extensional structures: the Tepic-Zacoalco rif zone (trending roughly northwest-southeast), which is defined as the northern boundary of the Jalisco block; and the Chapala rift zone (trending roughly east-

west). The connection between the northwest border of the Jalisco block (the Tamayo Fault Zone (Tamayo FZ) and the continent is not well defined. Previous studies have related this border to the San Blas fault as a continuation of the Tamayo FZ or to the Tres Mariás escarpment (west of Marias Islands) and the Río Ameca graben which crosses the Bahía de Banderas and continues along the Vallarta graben to join the Tepic-Zacoalco rif zone (Figure 1). Another possible connection is to the Tres Mariás escarpment. The last two possibilities suggest the existence of an additional small block, the Tres Mariás block, which may be experiencing strong crustal stresses as a result of the convergence direction of the Rivera plate (Kostoglodov and Bandy, 1995).

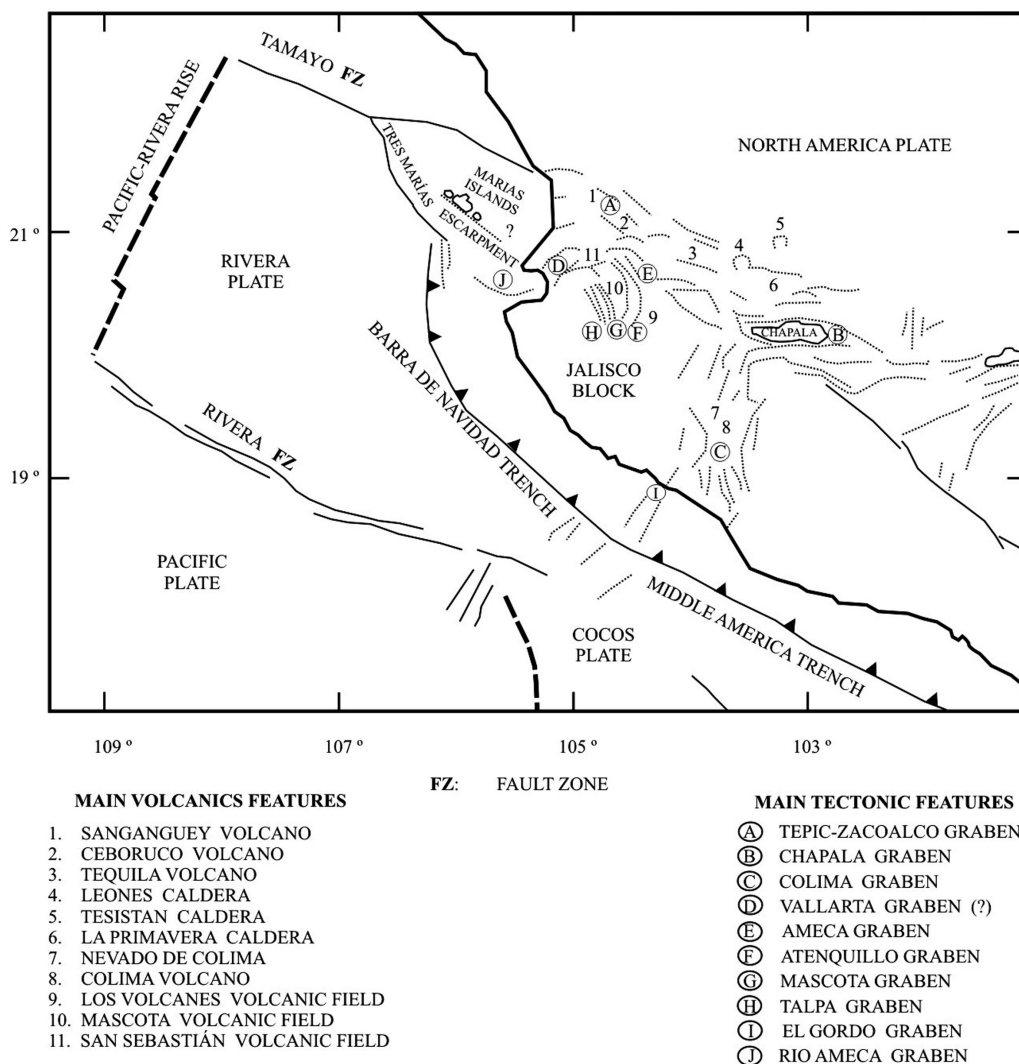


**Figure 1.** Tectonic frame of Jalisco Block region, modified from Núñez-Cornú *et al.* (2011).

*Regional seismicity*

The seismicity in the coast of Jalisco is associated with the subduction of the Rivera plate beneath the Jalisco block. Macroseismic data of seismicity in the region date back to 1544 and are described by Núñez-Cornú (2011). It is believed that both the 1932 earthquakes (Figure 2) ruptured the entire seismogenic contact between the Rivera plate and the Jalisco block (Singh *et al.*, 1985): The June 3, 1932 earthquake (M8.2) with an estimated rupture area of  $L = 220$  km and  $W = 80$  km; and the June 18, 1932 earthquake (M7.8) with an estimated rupture area of  $L = 60$  km, and  $W = 80$  km. Moreover, the complexity of this tectonic region reflects the existence of unknown or unstudied structures which may generate medium size earthquakes (M7.0-7.6), as the one occurred near Marias Islands, where the M7.0 earthquake turned

down masonry buildings of the presidio in María Madre island on December 3, 1948.

Shallow thrust earthquakes have also occurred resulting from intraplate activity, such as the M7.4 January 22, 2003 earthquake, located on the coast near of the city of Armería, Colima (Núñez-Cornú *et al.*, 2004, 2010).

The last large earthquake (M8.0) and tsunami in the southern part of the Jalisco Blok occurred on October 9, 1995. The rupture area was estimated to be  $L = 160 \pm 20$  km,  $W = 60$  km (Ortiz *et al.*, 1998; and Ortiz *et al.*, 2000), with a dislocation of less than 5 m. This rupture zone represents only the southern half of the area proposed by Singh *et al.* (1985) for the earthquakes of 1932, therefore the northern coast of Jalisco and Bahía de Banderas, Nayarit, remains to break.

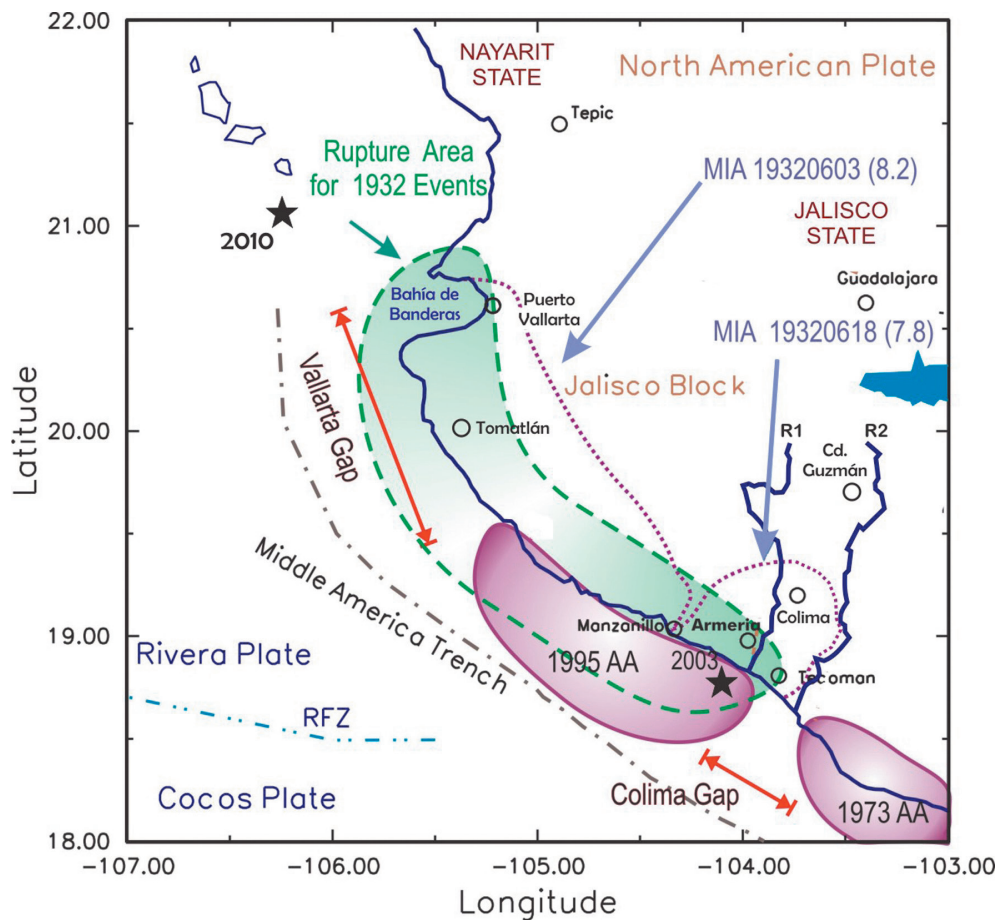


**Figure 2.** Seismotectonic features of the Jalisco region, modified from Rutz López *et al.* (2013). RFZ: Rivera Fracture Zone; R1: Armería River; R2: Coahuayana River; MIA: Maximum Intensity Areas for earthquakes in 1932 (dates and magnitudes indicated); AA: Aftershocks Areas; Cities; ★ 2003 Epicenter of the Armería earthquake (after Núñez-Cornú *et al.*, 2004) and ★ 2010 Marias Islands earthquake.

### *Tsunamis in Mexico*

The Mexican tide gauge network began in 1952, since then, until 1985 (Sanchez and Farreras, 1993), non-destructive transoceanic or distant generated tsunamis have been recorded with maximum heights in the range of  $0.1 \leq h \leq 2.5$  m. These distant tsunamis were caused by major earthquakes in areas of high seismicity, such as Alaska, Chile, Colombia, Kuril Islands, Japan, Kermadec, Kamchatka, and Perú.

While recent (Sumatra 2004; Chile 2010; Japan 2011) and historical (Chile 1960; Alaska 1964; Aleutians 1957) distant tsunamis have not generated damage on the west coast of Mexico, historical destructive tsunamis were originated by local earthquakes with seismic moment magnitude  $M_w \geq 7$ , along the interplate contact area located between the coast and the Middle America Trench, such as the one occurred off the coast of Oaxaca in 1787 (Núñez-Cornú *et al.*, 2008).

#### *Local tsunamis in Jalisco*

In the case of Jalisco, to the twentieth century, there are records of locally generated destructive tsunamis, three of them in June 1932 and one in October 1995. Historical reports mixed different tsunami damage in the month of June 1932, since the three of them occurred in a very short period of time in a sparsely populated and poorly communicated region. There is little information of these tsunamis and no published studies about its source mechanism. It is estimated that two of them were generated after the first two large earthquakes and the other probably by a submarine slump of sediments provided by the Armería River.

The June 3, 1932 tsunami, associated to the M8.2 earthquake, was observed to flood Barra de Navidad and partially flooded the port of San Blas, Nayarit. In Manzanillo Bay, the coast guard ship was in danger of running aground and capsizing due to the rapid sea level change. In Santiago Bay, the sea level rose about 3 m. In Cuyutlán, the coast seemed to rise and the sea flooded the resort, sweeping away several houses (Sanchez and Farreras, 1993).

After the June 18, 1932 earthquake (M7.8), the sea level in Manzanillo Bay decreased and then rose about 1 m. Sea waters flooded part of the port, and large part of the rocky coast lost its previous shape. Some of the shoals indicated in nautical charts disappeared.

The tsunami produced on the June 22, 1932 earthquake (M7.7) was the most destructive of all those produced in this region. It destroyed the resort of Cuyutlán. The estimated maximum height was  $h \leq 15$  m and the average extent of flooding was 1 km along 20 km of coast. This tsunami was generated probably by a submarine slump of sediments provided by the Armería River and accumulated on the continental shelf, to one of the creeks of the Middle America Trench (Ortiz, cited by Pacheco *et al.*, 1997). Cuyutlán was invaded by two tsunami waves of less intensity: one during the night of 22 June, and the other in the morning of the next day (Sanchez and Farreras, 1993).

The most recent and well documented tsunami in Jalisco is the one that occurred on the morning of October 9, 1995. "Historical" testimonies of the inhabitants describing the manner in which the waves invaded the coast were carefully collected, and the extent and height of the flooding or tsunami run-up along the Jalisco and Colima coasts were documented during the tsunami field survey conducted by Ortiz *et al.*, (1995), where the observed run-up heights were corrected or reduced to the height ( $h_c$ ) above the tide level at the time of flooding. The highest tsunami run-up ( $h_c \sim 5$  m) was observed in Tenacatita Bay in the towns of La Manzanilla and Boca de Iguanas. Figure 3, illustrates the tsunami flooding marks inside and outside the temple of La Manzanilla, Jalisco. The extents of flooding and run-up heights are shown in Table 1.

In spite of the very well documented seismic source of the October 9, 1995 Jalisco-Colima tsunami by inverting seismic and GPS data (see e.g., Courboulex *et al.*, 1997; and Pacheco *et al.*, 1997), inversion of this "historical" tsunami run-up records to model the 1995 Jalisco tsunami source is still important in order to provide some degree of certainty for the tsunami source of those historical tsunamis for which no seismic nor tide records are available, and only testimonies and vague relates of its effects are documented.

### **Method**

This paper follows the methodology used by Núñez-Cornú *et al.* (2008) to model the mechanism of the 1787 Tsunami source from historical data of the effects of flooding waves.

The rupture length of the October 9, 1995 Jalisco-Colima earthquake is estimated here as the length along the coast where tsunami

**Figure 3.** To illustrate the tsunami flooding marks inside and outside the temple of La Manzanilla, Jalisco, modified from Ortiz *et al.* (1995).

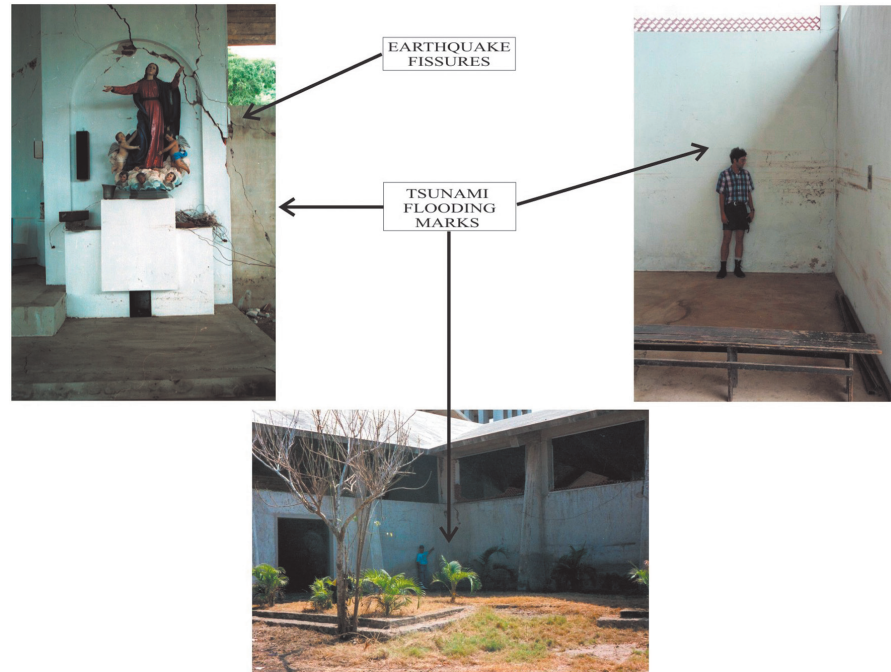


**Table 1.** Synthetic and observed tsunami run-up heights

Field survey, 1995					Model results				
+Distance km	Long	Lat	Extent of flooding (m)	Run up height $\odot$ hc (m)	Run up height $\blacklozenge$ hm (m)	$\Delta$ (%)	Time minutes	VTG/zone	County
15	105.26	19.68	100	2.90	2.63	- 9	41	1/Chalacatepec	Tomatlán
15	105.26	19.67	60	2.60		- 1			
32	105.13	19.59	40	3.3	3.90	18	40	2/Chamela	La Huerta
33	105.12	19.59	40	3.4		15			
35	105.11	19.58	40	4.9		- 20			
40	105.08	19.53	30	3.2		22			
40	105.08	19.53	15	3.0		30			
50	105.04	19.44	115	3.5	3.67	5	48	3/Careyes	La Huerta
67	104.94	19.31	70	3.8	4.30	13	72	4/El Tecuán	La Huerta
75	104.81	19.30	15	5.10	3.62	- 29	39	5/Tenacatita	La Huerta
78	104.81	19.30	30	4.20		- 14			
81	104.79	19.28	172	3.80		- 5			
81	104.79	19.28	141	4.00		- 9			
81	104.79	19.28	77	3.20		13			
90	104.73	19.23	30	4.10	4.64	13	46	6/San Patricio (Melaque)	Cihuatlán
92	104.71	19.22	41	4.50		3			
93	104.70	19.22	25	5.10		- 9			
96	104.68	19.20	17	3.70		26			
-	-	-	-	-	3.68	-	37	7/Marabasco	Cihuatlán
114	104.51	19.13	-	3.87	4.12	7	48	8/Playa de Oro	Manzanillo
125	104.41	19.10	-	4.40	3.69	- 16	82	9/Majagua	Manzanillo
127	104.38	19.12	-	3.74	3.38	- 10	51	10/Manzanillo	Manzanillo
129	104.35	19.16	-	3.00		13			
136	104.31	19.07	-	3.79		- 11			

+ Distance along the fault plane illustrated in Figure 4, starting from its NW edge.

$\odot$  hc = Observed tsunami run up height (Ortiz *et al.*,1995)

$\blacklozenge$  hm = Synthetic run-up height

$\Delta$ (%) = 100 (hm-hc)/hc; relative difference

flooding was observed (150-160 km, from Chalacatepec to Cuyutlán; Ortiz *et al.* (1995). In turn, to delineate the extent of the flooding of the tsunami we used the observed tsunami run-up data (Ortiz *et al.*, 1995). The run-up height ( $hc$ ) facilitates the delineation of the extent of flooding on the regional digital terrain elevation model by interpolating  $hc$  along the coast.

The rupture area proposed here (Figure 4), is a buried fault plane of  $L = 150$  km,  $W = 60$  km, dipping  $11^\circ$  towards the coast at the depth of 10 km in the interplate region, corresponding to an earthquake of  $Mw \sim 8.0$ , according to the relation:

$$Mw = \log_{10}(A) + 4.0,$$

where  $A$  is the area in  $km^2$  (Utsu and Seki, 1954; Wyss, 1979, Singh *et al.*, 1980). To this case, we are using an upper limit of  $Mw \sim 8.0$  obtained by seismic information (Pacheco *et al.*, 1997).

The total area is composed by ten segments with individual subareas  $A_i = 30 \times 30$   $km^2$ . The seismic moment  $Mo_i$  of each one of the segments may be varied by varying the coseismic dislocation ( $d_i$ ) according to the relationship  $Mo_i = \mu A_i d_i$ , to fit the moment magnitude of the earthquake (Hanks and Kanamori, 1979). Moment estimates assume a rigidity modulus  $\mu = 5 \times 10^{11}$   $dyne/cm^2$ ):

$$Mw = \frac{2}{3} \log_{10} \left( \sum_{i=1}^{10} Mo_i \right) - 10.7.$$

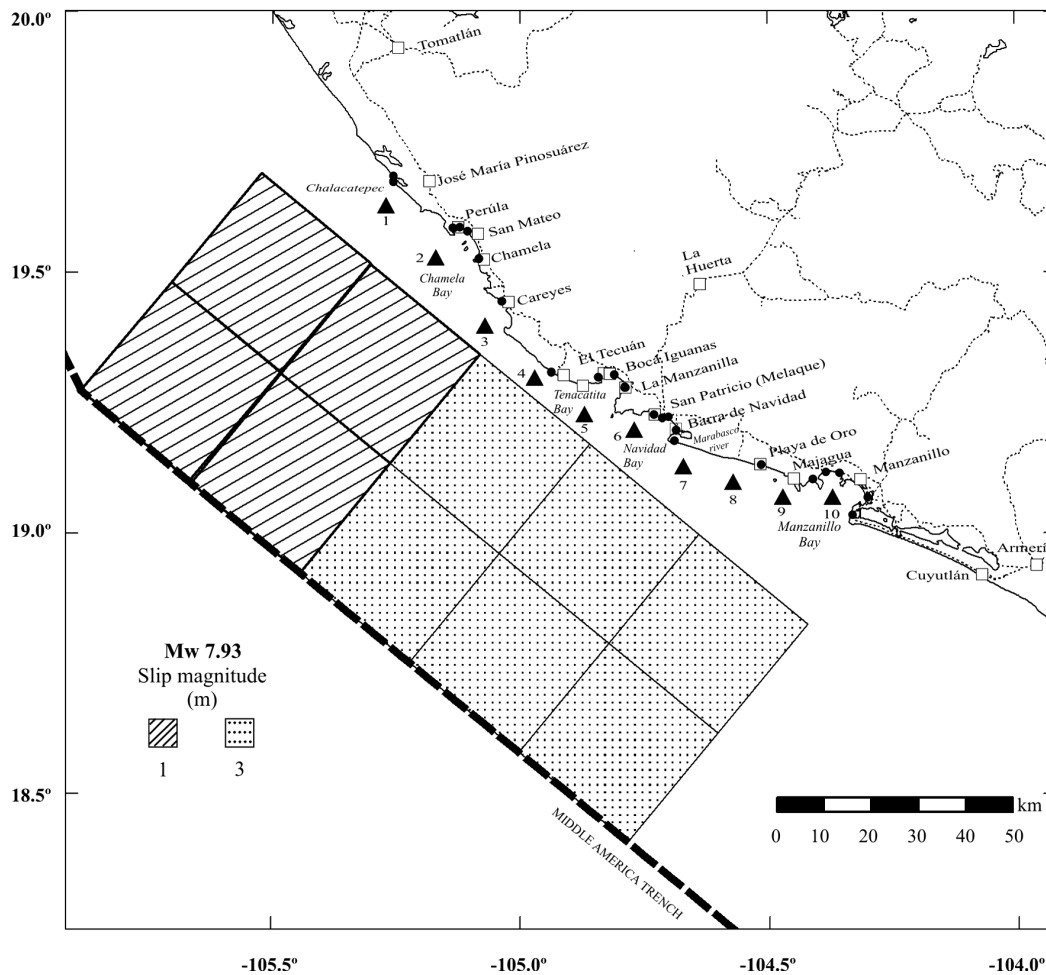


**Figure 4.** Map of the region and location of rupture area and subareas (rectangles) assumed in the numerical modeling of tsunami. Black dots indicate locations where tsunami run-up heights ( $hc$ ) were surveyed by Ortiz *et al.*, (1995). Black triangles indicate VTG locations where model results or synthetic run-up values ( $hm$ ) were obtained.

The coseismic vertical deformation of the seafloor as produced by the buried fault plane is computed by using the dislocation model of Mansinha and Smylie, (1971), by prescribing a reverse fault mechanism on each one of the segments. For the tsunami initial condition, the sea-level change was taken to be the same as the sea floor uplift calculated from the dislocation model.

The propagation of the tsunami was simulated by the vertically integrated long-wave equations (Pedlosky, 1979):

$$\frac{\partial \eta}{\partial t} + \nabla \cdot \mathbf{M} = 0$$

$$\frac{\partial \mathbf{M}}{\partial t} + gh \nabla \eta = 0$$

In these equations,  $t$  is time,  $\eta$  is the vertical displacement of the water surface above the equipotential level,  $h$  is the depth of the water column,  $g$  is the gravity acceleration, and  $\mathbf{M}$  is the vector of the discharge fluxes in longitudinal and latitudinal directions. These equations are solved in a spherical coordinate system by the method of finite differences with Leap-Frog scheme (Goto *et al.*, 1997). In the computation, the time step was set to 1 sec, and a grid spacing of 27 sec was used for the whole region, whereas a grid spacing of 3 sec was used to describe the shallow areas.

For near shore bathymetry, from 1000 m depth to the coast, we used data from local navigational charts, while for depths greater than 1000 m we used data from the ETOPO-2 data set (Smith and Sandwell, 1997).

A digital terrain model (cells of  $10 \times 10$  m<sup>2</sup>) for mapping the observed tsunami run-up values, as well as the synthetic ones resulting from the tsunami model, was interpolated from the digital topographic data set (GEMA), obtained by photogrammetry in a grid spacing of 3 sec in the years 1980-1990 (INEGI, 1994).

## Results

Model results or synthetic tsunamis are heights and times of arrival of wave trains within the first ten hours after the quake at locations defined here as virtual tide gauges (VTG), distributed along the coasts of Jalisco and Colima as illustrated in Figure 4. Synthetic run-

up values are defined here as the maximum height ( $hm$ ) of the synthetic tsunami above the sea level at the tsunami arrival time, at each one of the VTG locations.

### *Rupture area and dislocation*

The initial hypothesis considered the offshore rupture area  $L = 150$  km and  $W = 60$  km with a maximum coseismic dislocation of 4 m (Pacheco *et al.*, 1997). However, by setting  $d_i = 4$  m for the ten segments, all of the resulting synthetic run-up values ( $hm$ ) overestimate the corresponding observed ones ( $hc$ ). Guided by our prejudice that causal faults slipped with simple geometry, and that seafloor deformation field should be homogeneous and "smooth" we varied  $d_i$  smoothly as to obtain our best fit between  $hm_i$  and  $hc$  by setting up to 1 m the dislocation of the fault plane for the first 60 km along the fault plane starting from its NW edge (offshore Chalcatepec and Chamela), and to 3 m the dislocation of the next 90 km (offshore Tenacatita, Navidad and Manzanillo). For 19 of the 23 surveyed sites, the resulting synthetic run-up values are within 20% of the observed ones. Larger differences (less than 30%) are observed at the Bays of Chamela, Tenacatita, and Melaque, probably by the effects of local bathymetry. Observed and synthetic run-up values are shown in Table 1. The moment magnitude for this heterogeneous fault model is  $Mw7.93$ .

A series of plots (Figure 5) illustrate the sensitivity of the results ( $hm$ ) by shifting the location of the fault plane 30 km onshore; 30 km NW, and 30 km SW, respectively from our preferred location illustrated in Figure 4.

As expected, by shifting the fault plane 30 km onshore, most of the synthetic run-up values are 40% smaller than the observed ones; by shifting the fault 30 km NW, some of the synthetics are 50% larger than the ones observed in Chamela, and 40% smaller in Manzanillo; while by shifting the fault 30 SE, most of the synthetics underestimate the observed ones, with exception of the ones in Manzanillo.

### *Arrival times*

Synthetic tsunami waveforms at VTG's are shown in Figure 6; the synthetic tsunami arrival time in Jalisco is  $9 \leq t \leq 12$  minutes after the quake, while the time of the maximum wave height is  $39 \leq t \leq 46$  minutes, with exception at El Tecuán where the maximum occurs at  $t = 72$  minutes.

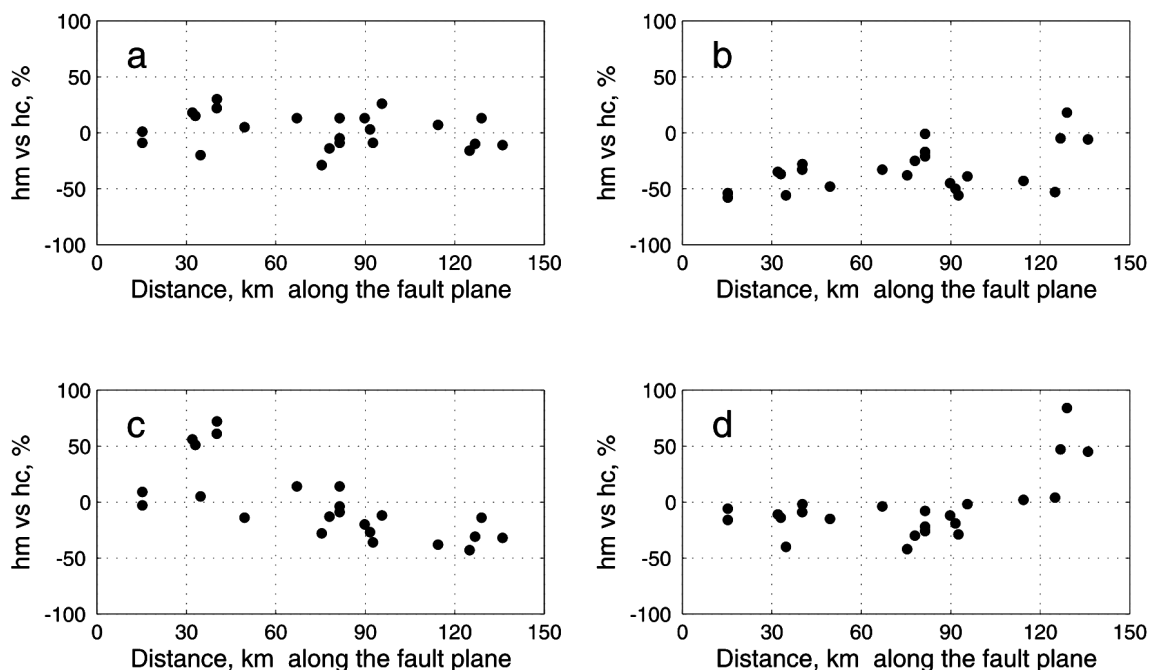


**Figure 5.** Observed  $hc$  versus synthetic  $hm$  run-up values obtained for the coast of Jalisco and Colima: a) by considering the rupture area proposed in Figure 4; b) by shifting the rupture area 30 km onshore; c) by shifting the rupture area 30 km NW; d) by shifting the rupture area 30 km SE. The origin of the distance axis corresponds to the NW edge of the fault plane illustrated in Figure 4.

#### *Extent of flooding*

By mapping observed run-up values as well as synthetic ones along the coast, we delineated the extent of flooding by the tsunami (Figure 7). In general, the flooding is extending in a strip of 50 m wide from the shoreline. Larger flooding areas are observed in Chalacatepec, the northern part of Chamela Bay, and in the Bays of Tenacatita and Navidad along rivers beds and wetland areas, where eyewitnesses reported that the tsunami penetrated up to 400 m inland. These maps can be used for urban planning and preparedness for large local tsunamis as the one occurred in 1995.

#### **Conclusions**

We model the source mechanism of the October 9, 1995 Jalisco-Colima earthquake as constrained by field survey reports of tsunami run-up and extent of flooding, and on the numerical simulation of the tsunami by considering an earthquake ( $M_w \sim 8.0$ ) with rupture area  $A = 9000 \text{ km}^2$ ,  $L = 150 \text{ km}$ ,  $W = 60 \text{ km}$ , with two different coseismic dislocation patches: 1 m the dislocation of the first 60 km along the fault plane starting from its NW edge (offshore Chalacatepec and Chamela), and 3 m the dislocation of the next 90 km (offshore Tenacatita, Navidad and Manzanillo).

As expected, the source mechanism of the earthquake obtained in this study is a simplified model in comparison of the seismic source obtained by inverting seismic and GPS data. However, the fact that this simplified model reproduces adequately the location of the rupture area and its coseismic dislocation, is still important in order to provide some degree of certainty for the tsunami source of those historical tsunamis for which no seismic nor tide records are available, and only testimonies and vague relates of its effects are documented.

#### **Acknowledgments**

We thank CONACYT for the scholarship to support the PhD student Elizabeth Trejo in the graduate program BEMARENA at the University of Guadalajara. To anonymous reviewers for their helpful review. We also acknowledge CONACYT-FOMIXJAL support for the Project M2012-08-189963 "Caracterización del Peligro Sísmico y Tsunamigénico asociado a la estructura cortical del contacto Placa de Rivera-Bloque Jalisco (TSUJAL)". TSUJAL Project CGL2011-29474-C02-01, Ministerio de Ciencia e Innovación, Dirección General de Investigación y Gestión del Plan Nacional de I+D+i, España.

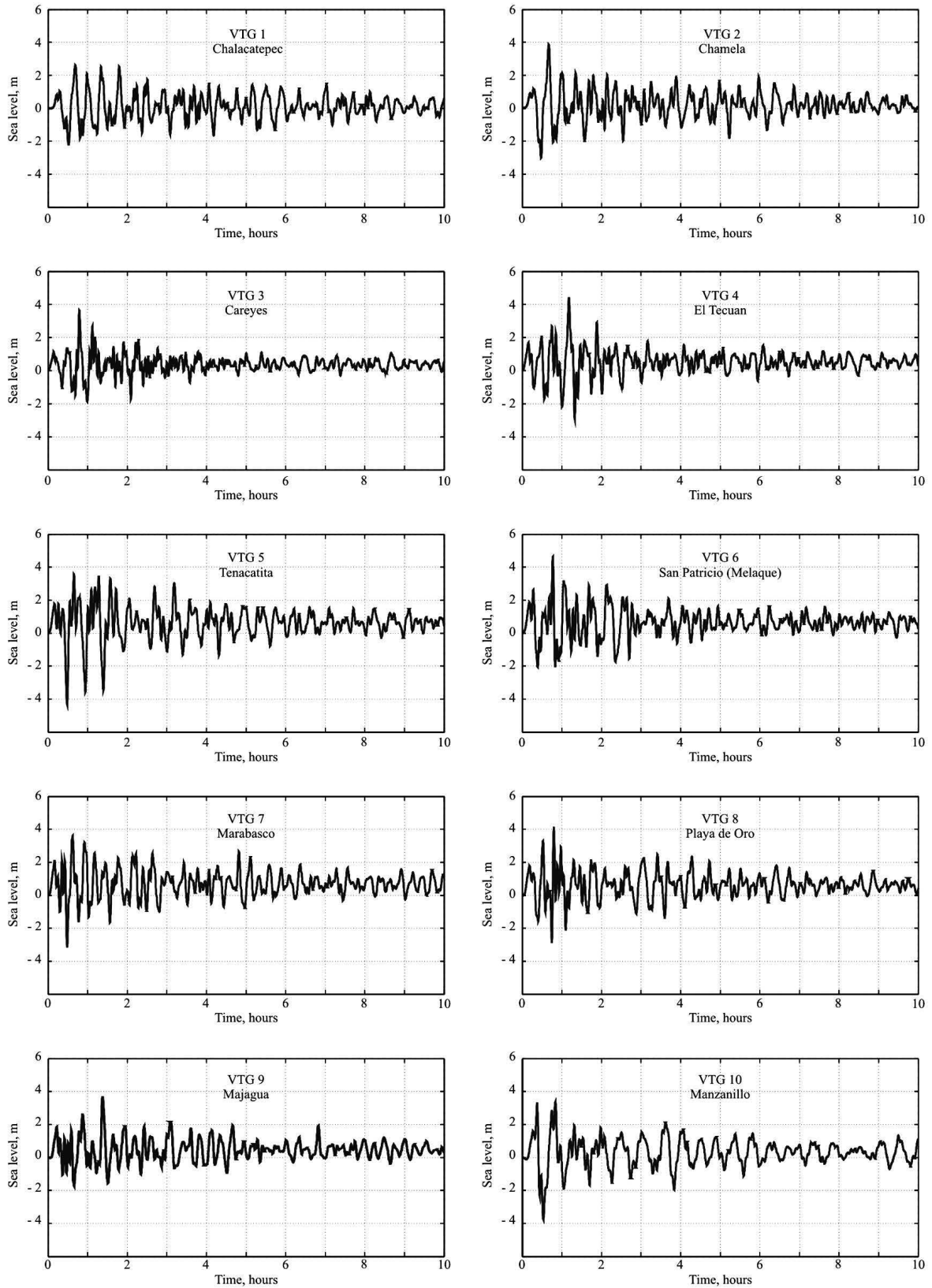


**Figure 6.** Synthetic tsunami waveforms at obtained the VTG locations illustrated in Figure 4.

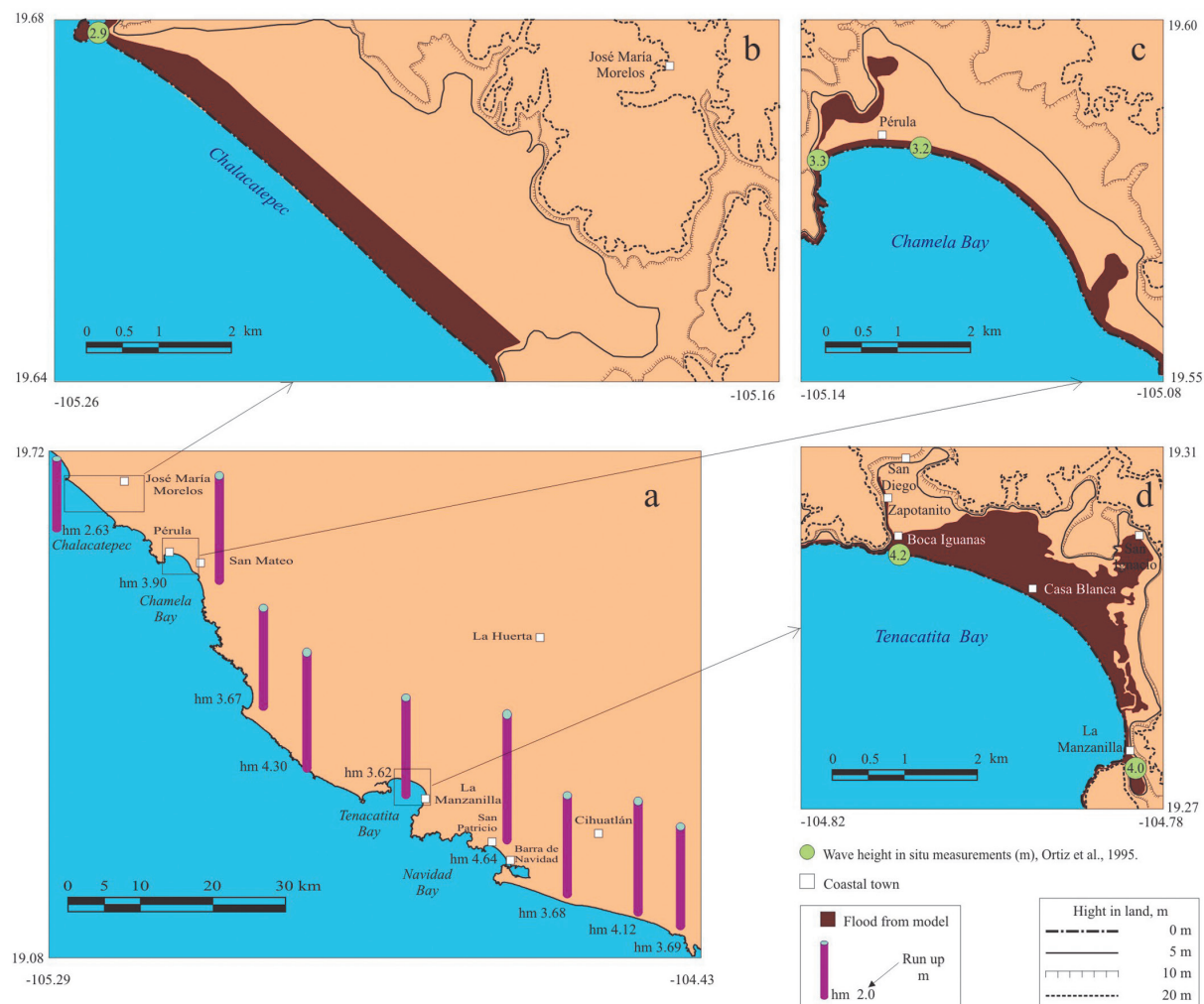


**Figure 7.** Extent of flooding by the October 9, 1995 Jalisco-Colima tsunami by mapping observed run-up values as well as synthetic ones along the coast of Jalisco and Colima: a) synthetic run-up values (hm) along the coast of Jalisco and Colima; b, c, and d) enlarged view of the extent of flooding in Chalacatepec, Chamela, and Tena-catita, respectively.

### Bibliography

Courboux F., Singh S.K., Pacheco J.F., Ammon C.J., 1997, The 1995 Colima Jalisco, Mexico, Earthquake (Mw8): A Study of the Rupture Process. *Geophys. Res. Lett.*, 24, 1019-1022.

Goto C., Ogawa Y., Shuto N., Imamura F., 1997, IUGG/IOC TIME Project: Numerical Method of Tsunami Simulation with the Leap-Frog Scheme. *Manual and Guides*, 35, 4, Intergovt. Oceanogr. Comm. of UNESCO, Paris.

Hanks T.C., Kanamori H., 1979, A Moment Magnitude Scale, 1979. *J. Geophys. Res. SE.*, 84, B5, 2348-2350. DOI:10.1029/JB084iB05p02348.

INEGI, 1994, Geo Modelo de Altitud del Territorio Nacional (GEMA-1994). Instituto Nacional de Estadística y Geografía (INEGI), Aguascalientes, México.

Kostoglodov V., Bandy W., 1995, Seismotectonic Constraints on the Convergence Rate Between the Rivera and North American Plates. *J. Geophys. Res.*, 100. DOI:10.1029/95JB01484.

Luhr J., Nelson S., Allan J., Carmichael I., 1985, Active Rifting in Southwestern Mexico: Manifestations of an Incipient Eastward Spreading-ridge jump. *Geology*, 13, 54-57.

Luhr J., Nelson S., Allan J., Carmichael I., 1985, Active Rifting in Southwestern Mexico: Manifestations of an Incipient Eastward Spreading-ridge jump. *Geology*, 13, 54-57.

- Mansinha L., Smylie E., 1971, The Displacement Field of Inclined Faults. *Bull. Seism. Soc. Am.*, 61, 1433-1440.
- Núñez-Cornú F.J., Ortiz M., Sánchez J.J., 2008, The Great 1787 Mexican Tsunami. *Nat. Haz.*, 47, 569-576. DOI:10.1007/s11069-008-9239-1.
- Núñez-Cornú F.J., 2011, Peligro Sísmico en el Bloque Jalisco. *Física de la Tierra*, 23, 199-299.
- Núñez-Cornú F.J., Reyes-Dávila G.A., Rutz-López M., Trejo-Gómez E., Camarena-García M.A., Ramírez-Vázquez C.A., 2004, The 2003 Armería, Mexico Earthquake (Mw7.4): Mainshock and Early Aftershocks. *Seis. Res. Lett.*, 75, 6, 734-743.
- Núñez-Cornú F.J., Rutz López M., Márquez Ramírez V., Suárez-Plascencia C., Trejo Gómez E., 2010, Using an Enhanced Dataset for Reassessing the Source Region of the 2003 Armería, México Earthquake. *Pure and App Geoph.*, 168, 1293-1302. (ISSN: 0033-4553). DOI 10.1007/s00024-010-0178-x.
- Ortiz M., González J.I., Reyes J., Nava C., Torres E., Saenz G., Arrieta J., 1995, Efectos Costeros del Tsunami del 9 de Octubre de 1995 en la Costa de Colima y Jalisco, Informe Técnico. Centro de Investigación Científica y de Educación Superior de Ensenada (CICESE), Baja California, México, 19 pp.
- Ortiz M., Kostoglodov V., Singh S.K., Pacheco J., 2000, New Constraints on the Uplift of October 9, 1995 Jalisco-Colima Earthquake (Mw8) Based on the Analysis of Tsunami Records at Manzanillo and Navidad, Mexico. *Geofísica Internacional*, 39, 349-357.
- Ortiz M., Singh S.K., Pacheco J., Kostoglodov V., 1998, Rupture Length of the October 9, 1995 Colima-Jalisco earthquake (Mw8) estimated from Tsunami Data. *Geophys. Res.*, 25, 2857-2860.
- Pacheco J., Singh S.K., Domínguez J., Hurtado A., Quintanar L., Jiménez Z., Yamamoto J., Gutiérrez C., Santoyo S., Bandy W., Guzmán M., Kostoglodov V., 1997, The October 9, 1995 Colima-Jalisco Mexico Earthquake (Mw8): and Aftershock Study and Comparison of this Earthquake with those of 1932. *Geophys. Res. Lett.*, 24, 17, 2223-2226.
- Pedlosky J., 1979, *Geophysical Fluid Dynamics*. Springer-Verlag, New York, 664 pp.
- Rutz López M., Núñez Cornú F.J., Suárez Plascencia C., 2013, Study of Seismic Clusters at Bahía de Banderas Region, Mexico. *Geofísica Internacional*, 52, 1, 59-72.
- Sánchez A.J., Farreras S., 1993, Catalog of Tsunamis on the Western Coast of Mexico, World Data Center A for Solid Earth Geophysics. Publication SE-50, National Geophysical Data Center, National Oceanic and Atmospheric Administration (NOAA), Washington, 94 pp.
- Singh S.K., Bazan E., Estevas L., 1980, Expected Earthquake Magnitude from a Fault. *Bull. Seism. Soc. Am.*, 70, 903-914.
- Singh S.K., Ponce L., Nishenko S. P., 1985, The Great Jalisco, México, Earthquakes of 1932: Subduction of the Rivera plate. *Bull. Seism. Soc. Am.*, 75, 1301-1313.
- Smith W.H.F., Sandwell D.T., 1997, Global Sea Floor Topography from Satellite Altimetry and Ship Depth Soundings. *Science*, 277, 1956-1962.
- Utsu T., Seki A., 1954, A Relation Between the Area of Aftershock Region and the Energy of Main Shock (in Japanese). *J. Seism. Soc. Jap.*, 7, 233-240.
- Wyss M., 1979, Estimation Maximum Expectable Magnitude of Earthquakes from Fault Dimensions. *Geology*, 7, 336-340.

## The Chromospheric Solar Millimeter-wave Cavity; a Common Property in the Semi-empirical Models

Víctor de la Luz\*, Miguel Chavez and Emanuele Bertone

Received: December 11, 2013; accepted: August 14, 2014; published on line: March 31, 2015

### Resumen

Los modelos semi-empíricos de la cromosfera solar son herramientas importantes en el estudio de la radio emisión solar a longitudes de onda milimétricas-infrarrojas. Sin embargo, los modelos actuales siguen sin reproducir las observaciones del Sol quieto. En este trabajo, presentamos un estudio teórico de la ecuación de transferencia radiativa para cuatro modelos semi-empíricos a estas longitudes de onda. Encontramos que la Cavidad Cromosférica Solar a Longitudes de Onda Milimétricas (CSMC), una región donde la atmósfera se vuelve ópticamente delgada localmente a longitudes de onda milimétricas, está presente en los modelos semi-empíricos bajo estudio. Concluimos que la CSMC es una propiedad general de la cromosfera solar donde los modelos cromosféricos muestran un mínimo de temperatura.

Palabras clave: Sol: cromosfera, Sol: radio emisión solar, Sol: infrarrojo, métodos: numéricos, transferencia radiativa, estrellas: cromosferas.

### Abstract

The semi-empirical models of the solar chromosphere are useful in the study of the solar radio emission at millimeter - infrared wavelengths. However, current models do not reproduce the observations of the quiet sun. In this work we present a theoretical study of the radiative transfer equation for four semi-empirical models at these wavelengths. We found that the Chromospheric Solar Millimeter-wave Cavity (CSMC), a region where the atmosphere becomes locally optically thin at millimeter wavelengths, is present in the semi-empirical models under study. We conclude that the CSMC is a general property of the solar chromosphere where the semi-empirical models shows temperature minimum.

Key words: Sun: chromosphere, Sun: radio radiation, Sun: infrared, methods: numerical, radiative transfer, stars: chromospheres.

---

V. De la Luz\*  
SCiESMEX  
Instituto de Geofísica  
Unidad Michoacán  
Universidad Nacional Autónoma de México  
CP. 58190  
Morelia, Michoacán, México  
\*Corresponding author: [iztli@gmail.com](mailto:iztli@gmail.com)

M. Chavez  
E. Bertone  
Instituto Nacional de Astrofísica  
Óptica y Electrónica  
Apdo. Postal 51 y 216, 72000  
Tonantzintla, Puebla, México

## Introduction

In 1902, the first theoretical computation of the stellar radio emission using a black body at 5700 K showed that the flux that emerges of the solar surface was almost impossible, at that epoch, to observe from ground based observations due to low computed flux and the sensitivity of the instruments, which discouraged the first attempts to observe the solar radio emission (Nordmann, 1905).

Fourty years after the Planck theoretical computations, the first radio observation of the quiet sun was confirmed (Reber, 1944; Martyn, 1946). Observations (Pawsey and Yabsley, 1949; Zirin, Baumert, and Hurford, 1991; Vourlidis *et al.*, 2010), and the theoretical models where subsequently improved from two steps models (cold-hot) to sophisticated hydrostatic models (Smerd, 1950; van de Hulst, 1953; Allen, 1963; Ahmad and Kundu, 1981; Vernazza, Avrett, and Loeser, 1981; Fontenla *et al.*, 2011).

The hydrostatic semi-empirical models showed that the stratification of the chromosphere could explain the continuum in the millimeter-infrared spectral region. The UV emission becomes the major point of reference to calibrate the semi-empirical models while the radio continuum was used only to test the auto consistence of the models (Vernazza, Avrett, and Loeser, 1981).

The semi-empirical models of the quiet sun chromosphere have two hypotheses: the magnetic field at these scales have no effect in the convective flux and the vertical scale is lower than the horizontal scale (Fontenla *et al.*, 2006). The results of these hypotheses is a stratified plain-parallel atmosphere in hydrostatic equilibrium. In the UV-visible region have provided good approximations, however differences between the synthetic spectra and the observations, specially those associated at altitudes around the temperature minimum of the solar chromosphere, can be observed at millimeter and infrared regions (Landi and Chiuderi Drago, 2003).

Regardless of the theoretical approaches, we now know that the chromosphere is a very reach region of the solar atmosphere where the magnetic field at micro scales plays an important role in the morphology of this layer (Vourlidis *et al.*, 2010). However, the infrastructure required to observe the micro structure at radio frequencies is still beyond current observational capabilities.

In this work, we study the radiative transfer equation specially at heights associated with the temperature minimum of the solar chromosphere to reproduce the Chromospheric Solar Millimeter-wave Cavity (CSMC) found in De la Luz, Raulin, and Lara (2013) using 4 different semi-empirical models as input: VALC from Vernazza, Avrett, and Loeser (1981), SRPM305 from Fontenla *et al.* (2006), the cold [1000A], and hot [1008Q] models from Fontenla *et al.* (2011). These models have the general characterize that present temperature minimum region and the authors used the millimeter emission region to test the auto consistence of their models.

The goal of this work is to explore if CSMC is a general property of solar atmospheric models that include a temperature minimum region.

## The Semi-empirical Models

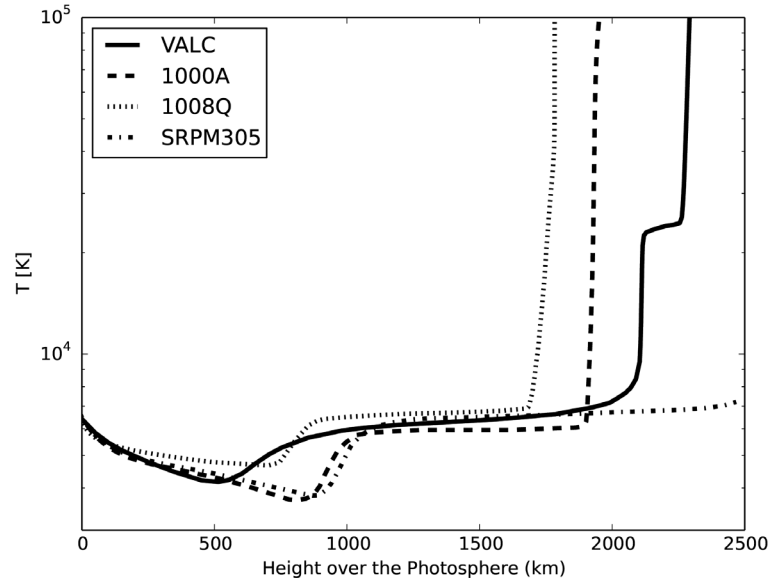
In Figure 1 we plot the temperature profile for the VALC, SRPM305, 1000A, and 1008Q models. We can observe the temperature minimum region between 100 and 1000 km over the photosphere. The temperature profiles show a decrement of the temperature that comes from the photosphere until reaches to the minimum value of temperature, then the gradient inverts and the temperature increments, a plateau of temperature of around 1000 km is presented in all the models, finally the temperature grows until coronal temperatures of around  $1e6$  K.

For the density (figure 2), the models shows a exponential decrease starting at photospheric altitudes until altitudes around the value of minimum temperature. The density profiles depend directly of the temperature profile: for lower temperatures the density is also lower. Finally, at high altitudes with respect the photosphere, the density profile is correlated with the increase of the temperature profile towards coronal temperatures. In this region, the density drops two orders of magnitude to coronal density values ( $n \approx 1e7\text{cm}^{-3}$ ).

## Computations

We used the code PakalMPI (De la Luz, Lara, and Raulin, 2011) to solve the radiative transfer equation. The code is written in C/ MPI with GNU/GPL License. PakalMPI take as input the hydrogen density, temperature, and metallicity radial profiles; computes the ion abundances in LTE for 18 atoms and the NLTE abundances for H, H-, and electrons. Then, computes the ray path and solve (using integrations step controlled by an intelligent algorithm) the radiative transfer equations

**Figure 1.** Temperature profiles for semi-empirical models.



using three opacity functions (Bremsstrahlung, H $\gamma$ , and Inverse Bremsstrahlung). Finally, the brightness temperature, the optical depth and the opacities are printed step by step in altitude at each frequency. This information is used for our analysis to compute the local emissivity:

$$E_1 = 1 - \exp(-\tau_{\text{local}})$$

where  $\tau_{\text{local}}$  is the local optical depth. The  $E_1$  parameter shows the capability of the atmosphere to generate radiation. When  $E_1 \approx 0$  the atmosphere is transparent (optically thin) and if  $E_1 \approx 1$  the atmosphere is optically thick. We use the  $E_1$  value as a diagnostic of the radiative transfer in the solar chromosphere (De la Luz, Raulin, and Lara, 2013).

**Results**

Figure 3 shows the local emissivity ( $E_1$ ) for the four semi-empirical models under study plotting height vs frequency over the photosphere and in colors the  $E_1$  parameter or equivalently, the altitude where the emission is generated. For the four semi-empirical models the region where the atmosphere is locally optically thick is presented as a peak around 1000 km over the photosphere. Below this peak, a region where locally the atmosphere is transparent is also presented. This region is what we have called the CSMC. We found that the CSMC is present in all models. In the Figure 4, we show that the depth of the cavity (with respect to the frequency) reaches lower frequencies for

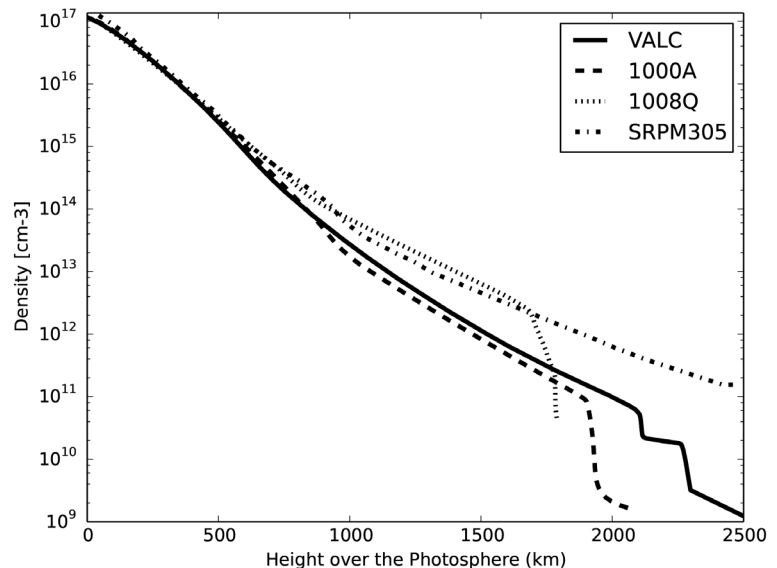


**Figure 2.** Density profiles for semi-empirical models.

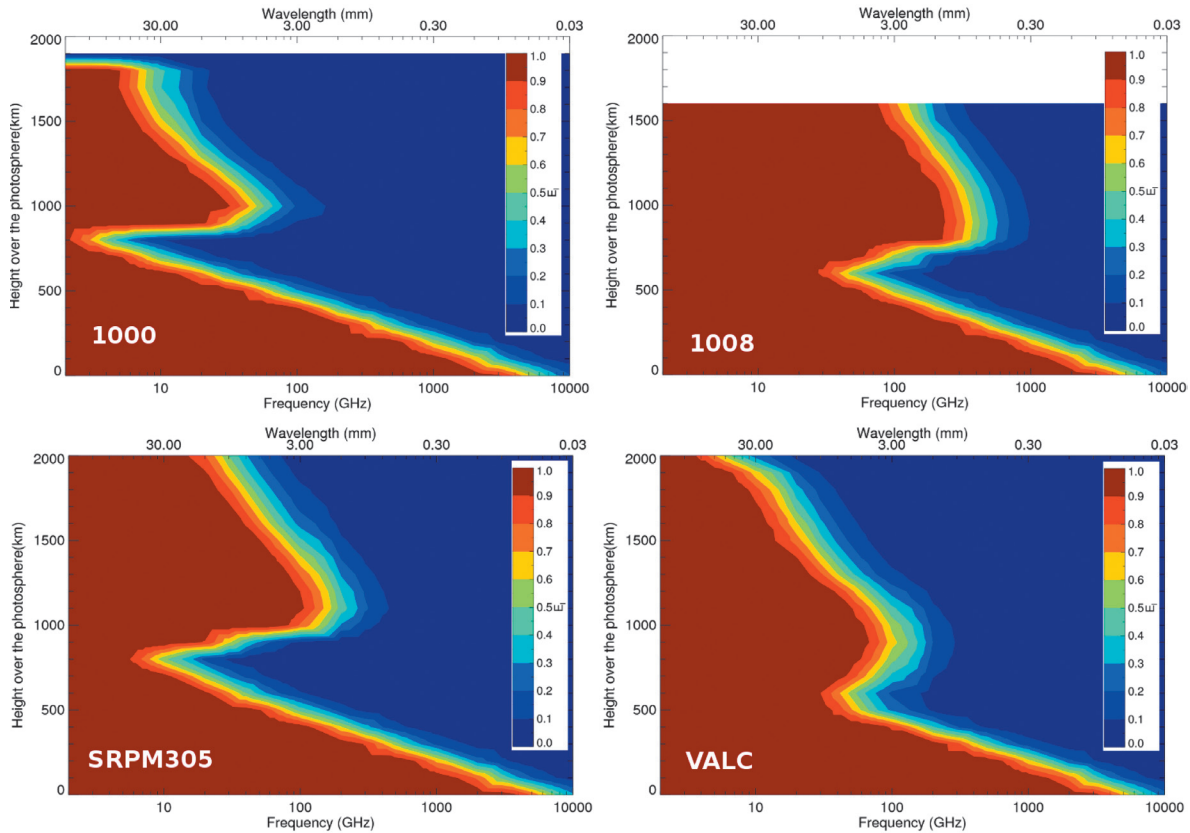


**Figure 3.** CSMC for the four models under study.

lower temperature minimum. In the Figure 5, we show the relation between the cavity and the density profile. The continuous line show the relation between the height over the photosphere where the peak of the CSMC is

maximum in frequency and their density in the semi-empirical model at the same altitude. A dependence between frequency and density is not evident for the case of the peak of the CSMC.

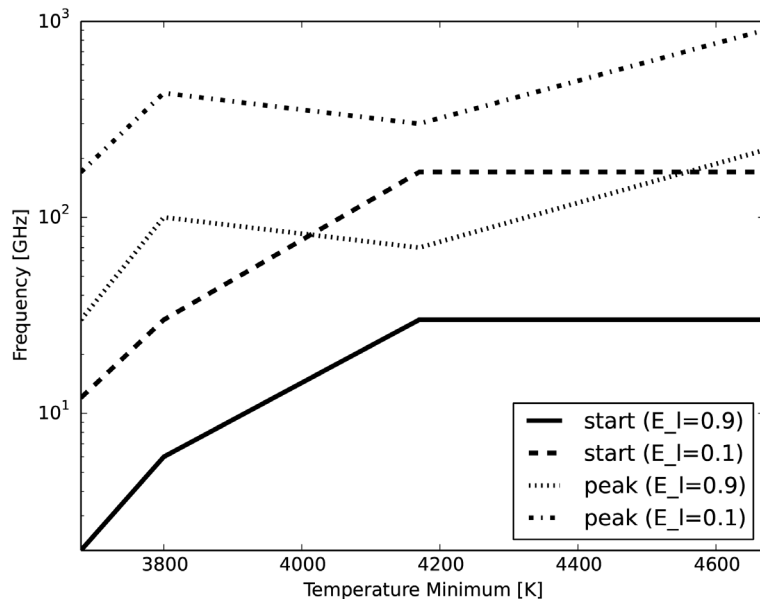
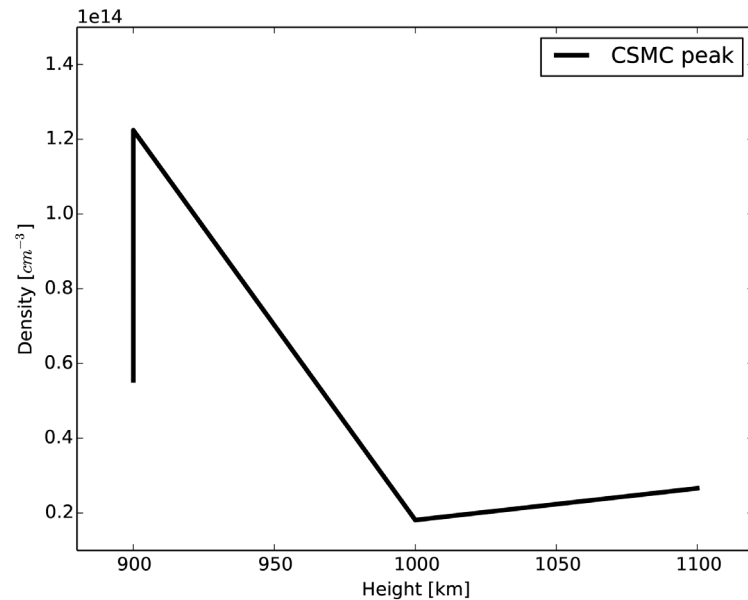


**Figure 4.** Relation between the value of the temperature minimum and the CSMC for the start of the cavity (for two local emissivity thresholds, 0.9 and 0.1) and the peak of the cavity (also for  $E_l = 0.9$  and 0.1). We take into account the value of the following temperature minimum: 1000A  $\sim$  3680K; SRPM305  $\sim$  3800K; VALC  $\sim$  4170K; 1008Q  $\sim$  4670K.

**Figure 5.** Relation between the height over the photosphere where the peak of the cavity is maximum ( $E_i = 0.1$ ) and their density at this altitude.



## Conclusions

We found the CSMC in the four semi-empirical models under study. Figures 4 and 5 show that the temperature plays an important role in the depth in frequency of the cavity, however a clear relation between the density and the peak of the cavity is not clearly shown. The peak of the cavity is important because it is the responsible of the morphology of the spectrum at sub-millimeter and infrared wavelengths, and its characterization is fundamental to develop more realistic models that ameliorate the discrepancies between theory and observations. The fact that we found the CSMC in the four semi-empirical models, allow us to conclude that the CSMC is a general property of physical systems where the density drops exponentially and where there is a temperature minimum region.

## References

- Ahmad I.A., Kundu M.R., 1981, Microwave solar limb brightening. *Solar Phys.*, 69, 273 – 287.
- Allen C.W., 1963, Local Physics of the Corona. In: Evans, J.W. (ed.) *The Solar Corona*, IAU Symposium 16, 1 – +.
- De la Luz V., Lara A., Raulin J.-P., 2011, Synthetic Spectra of Radio, Millimeter, Sub-millimeter, and Infrared Regimes with Non-local Thermodynamic Equilibrium Approximation. *Astrophys. J.* 737, 1 – +. doi:10.1088/0004-637X/737/1/1.
- De la Luz V., Raulin J.-P., Lara A., 2013, The Chromospheric Solar Millimeter-wave Cavity Originates in the Temperature Minimum Region. *Astrophys. J.*, 762, 84. doi:10.1088/0004-637X/762/2/84.
- Fontenla J.M., Avrett E., Thuillier G., Harder J., 2006, Semiempirical Models of the Solar Atmosphere. I. The Quiet- and Active Sun Photosphere at Moderate Resolution. *Astrophys. J.*, 639, 441 – 458. doi:10.1086/499345.
- Fontenla J.M., Harder J., Livingston W., Snow M., Woods T., 2011, High-resolution solar spectral irradiance from extreme ultraviolet to far infrared. *Journal of Geophysical Research (Atmospheres)*, 116, 20108. doi:10.1029/2011JD016032.
- Landi E., Chiuderi Drago, F., 2003, Solving the Discrepancy between the Extreme Ultraviolet and Microwave Observations of the Quiet Sun. *Astrophys. J.*, 589, 1054 – 1061. doi:10.1086/374811.
- Martyn D.F., 1946, Temperature Radiation from the Quiet Sun in the Radio Spectrum. *Nature*, 158, 632 – 633. doi:10.1038/158632a0.
- Nordmann C., 1905, Essai Sur le Role des Ondes Hertiennes en Astronomie Physique et Sur Diverses Questions Qui S'y Rattachent. *Annales de l'Observatoire de Nice* 9, A1.
- Pawsey J.L., Yabsley D.E., 1949, Solar Radio-Frequency Radiation of Thermal Origin.

Australian Journal of Scientific Research A  
Physical Sciences 2, 198 – +.

Reber G., 1944, Cosmic Static. *Astrophys. J.*,  
100, 279 – +.

Smerd S.F., 1950, Radio-Frequency Radiation  
from the Quiet Sun. *Australian Journal of  
Scientific Research A Physical Sciences*, 3,  
34 – +.

van de Hulst H.C., 1953, The Chromosphere  
and the Corona, *The Sun*, 207 – +.

Vernazza J.E., Avrett E.H., Loeser R., 1981,  
Structure of the solar chromosphere. III –  
Models of the EUV brightness components  
of the quiet-sun. *Astrophys. J. Supp.*, 45,  
635 – 725. doi:10.1086/190731.

Vourlidas A., Sanchez Andrade-Nuno B., Landi  
E., Patsourakos S., Teriaca L., Schuhle  
U., Korendyke C.M., Nestoras I., 2010,  
The Structure and Dynamics of the Upper  
Chromosphere and Lower Transition Region  
as Revealed by the Subarcsecond VAULT  
Observations. *Solar Phys.*, 261, 53 – 75.  
doi:10.1007/s11207-009-9475-x.

Zirin H., Baumert B.M., Hurford G.J., 1991,  
The microwave brightness temperature  
spectrum of the quiet sun. *Astrophys. J.*,  
370, 779 – 783. doi:10.1086/169861.

## Paleomagnetic Pole Positions and Geomagnetic Secular Variation from the Cretaceous Ponta Grossa Dike Swarm (Brazil)

Miguel Cervantes Solano, Avto Goguitchaichvili\*, Mabel Mena, Luis Alva-Valdivia, Juan Morales Contreras, Ruben Cejudo Ruiz, Héctor López Loera, Ana María Soler and Jaime Urrutia-Fucugauchi

Received: February 19, 2014; accepted: July 03, 2014; published on line: March 31, 2015

### Resumen

A detailed paleomagnetic and rock magnetic investigation has been carried out on the Early Cretaceous Ponta Grossa dike swarm in southern Brazil. This formation seems an excellent target for paleomagnetic study. The dikes are widely distributed over a large area, easy to access, and they record faithfully the geomagnetic field at the time of the eruption. Most of them are fresh and have been dated by K-Ar and Ar-Ar. Thermomagnetic experiments (low-field versus temperature curves) suggest low-Ti titanomagnetites as main remanence carriers, and their domain structure is characterised by a mixture of single-domain and multi-domain grains. Characteristic paleomagnetic directions are retrieved from 28 out of 29 sites (235 standard paleomagnetic cores). 17 sites show normal polarity, 10 sites show reverse polarity and one site shows an oblique direction, with negative inclination, separated 79° of

the mean normal directions. The reversal test is positive at the 95% confidence level which ensures that the secondary remanent magnetizations were successfully removed and the sampling adequately averaged the palaeosecular variation. The paleosecular variation parameters values obtained in this study correlate with those determined for the Cretaceous Normal Superchron, between 125 to 84 Ma. The new paleomagnetic pole position (222.0° E, 88.1° S,  $N = 24$ ,  $K = 35.68$ ,  $A_{95} = 5.0^\circ$ ) agrees well (within uncertainties) with the reference poles determined from Besse and Courtillot (2002), and disagree with those reported in previous studies. The new results should be considered for estimating the Cretaceous paleomagnetic poles for stable South America.

Palabras clave: Ponta Grossa Dike Swarm, South America, Paleomagnetism, Cretaceous.

---

M. Cervantes Solano  
Escuela Nacional de Estudios Superiores  
Unidad Morelia  
Universidad Nacional Autónoma de México  
Morelia, México

A. Goguitchaichvili  
J. Morales Contreras  
R. Cejudo Ruiz  
Laboratorio Interinstitucional de Magnetismo Natural  
Instituto de Geofísica  
Campus Morelia  
Universidad Nacional Autónoma de México  
Morelia, México  
*\*Corresponding author: avto@geofisica.unam.mx*

M. Mena  
Instituto de Geofísica  
Daniel Valencio  
Dpto. Ciencias Geológicas  
Facultad de Ciencias Exactas y Naturales  
Universidad de Buenos Aires, Argentina

L. Alva-Valdivia  
H. López Loera  
A. María Soler  
División de Geociencias Aplicadas del  
Instituto Potosino de Investigación Científica y  
Tecnológica A. C.  
San Luis Potosí, S. L. P., México

J. Urrutia-Fucugauchi  
Laboratorio de Paleomagnetismo  
Instituto de Geofísica  
Universidad Nacional Autónoma de México  
Ciudad Universitaria  
Delegación Coyoacán, 04510  
México D.F., México

## Abstract

A detailed paleomagnetic and rock magnetic investigation has been carried out on the Early Cretaceous Ponta Grossa dike swarm in southern Brazil. This formation seems an excellent target for paleomagnetic study. The dikes are widely distributed over a large area, easy to access, and they record faithfully the geomagnetic field at the time of the eruption. Most of them are fresh and have been dated by K-Ar and Ar-Ar. Thermomagnetic experiments (low-field versus temperature curves) suggest low-Ti titanomagnetites as main remanence carriers, and their domain structure is characterised by a mixture of single-domain and multi-domain grains. Characteristic paleomagnetic directions are retrieved from 28 out of 29 sites (235 standard paleomagnetic cores). 17 sites show normal polarity, 10 sites show reverse polarity and one site shows an oblique direction, with negative inclination, separated 79° of

## Introduction

The study of the remanent magnetism recorded in rocks is the basis for constraining important problems in plate tectonics and paleogeographic reconstructions at different time scales. Paleomagnetic poles are often used to determine past location of continents. Reliable reconstructions of geological terrains cannot be obtained from poorly defined paleomagnetic poles, no matter how many sites are used. Precisely defined reference paleopoles (Besse and Courtillot, 2002) are crucial to produce robust paleocontinental reconstructions.

The Parana Magmatic Province and surrounding volcanic areas, including the Ponta Grossa Dikes have been subject of many paleomagnetic studies (Ernesto *et al.*, 1990, 1996, 1999; Raposo *et al.*, 1995; Raposo *et al.*, 1998; Alva-Valdívila *et al.*, 2003; Mena *et al.*, 2006). However, the paleomagnetic pole positions obtained in these studies present unusually high dispersion, which probably do not reflect the true characteristics of the Earth's magnetic field for the time interval of ~140-120 Ma. As discussed by Alva-Valdivia *et al.* (2003), the apparent high scatter in paleomagnetic pole positions may be due to unrecognized tectonic disturbances (see also Ernesto *et al.*, 1990).

On other hand, the fine scale characteristics of the geomagnetic field during the Cretaceous is of great interest in understanding the long-

term evolution of the geomagnetic field, related to the constant polarity superchron, the polarity reversal frequency patterns and paleosecular variation. The fluctuation of earth's magnetic field elements is closely connected to conditions in the Earth's liquid core and at the core-mantle boundary. Paleomagnetic data provide an invaluable source of information on the Earth's liquid core and deep interior.

the mean normal directions. The reversal test is positive at the 95% confidence level which ensures that the secondary remanent magnetizations were successfully removed and the sampling adequately averaged the palaeosecular variation. The paleosecular variation parameters values obtained in this study correlate with those determined for the Cretaceous Normal Superchron, between 125 to 84 Ma. The new paleomagnetic pole position (222.0° E, 88.1° S,  $N = 24$ ,  $K = 35.68$ ,  $A_{95} = 5.0^\circ$ ) agrees well (within uncertainties) with the reference poles determined from Besse and Courtillot (2002), and disagree with those reported in previous studies. The new results should be considered for estimating the Cretaceous paleomagnetic poles for stable South America.

Key Words: Ponta Grossa Dike Swarm, South America, Paleomagnetism, Cretaceous.

term evolution of the geomagnetic field, related to the constant polarity superchron, the polarity reversal frequency patterns and paleosecular variation. The fluctuation of earth's magnetic field elements is closely connected to conditions in the Earth's liquid core and at the core-mantle boundary. Paleomagnetic data provide an invaluable source of information on the Earth's liquid core and deep interior.

There are two clear intervals in the geological past when the Earth's magnetic field remained with constant polarity for a considerable length of time: from about 125 to 84 Ma the polarity was normal (so-called the Cretaceous Normal Superchron—CNS) and from about 310 to 260 Ma the polarity was reversed (so-called the Permo-Carboniferous Superchron—PCRS). During the last decades, many investigations were devoted to study the morphology of the earth's magnetic field during the Cretaceous (Biggin *et al.*, 2008). Namely, most important question is related to the variability during and around the CNS. The particularity of this interval (125 to 84 Ma after Cande and Kent, 1995 and Tarduno *et al.*, 2002) is that Earth's magnetic field did not reverse polarity. Knowledge of the geomagnetic field behaviour just prior to CNS is patchy and largely unknown. Thus, more accurate paleomagnetic studies giving information about the past behavior of the geomagnetic field are strongly needed.

High quality paleomagnetic reference poles are required to distinguish true polar wander effects from relative hotspot motion, and to

constrain major geodynamic events (Torsvik *et al.*, 2002; Somoza and Zaffarana, 2008). Major tectonic events characterize the mid- and late Cretaceous, with the final stages of Gondwana breakup, volcanic plateau emplacement and fast seafloor spreading rates (e.g., Taylor, 2006; Seton *et al.*, 2009).

The present study is aimed to determine precise Early Cretaceous paleomagnetic pole positions for stable South America, and contribute to the study of the fluctuations of the Earth's magnetic field just prior to the Cretaceous Normal Superchron. A preliminary paleointensity study was already reported from the Ponta Grossa dikes, analyzing 3 sites with 11 samples (Cejudo *et al.*, 2009). The present study expands on the initial reconnaissance study, based on 335 standard paleomagnetic cores belonging to 29 dikes.

### Geological Setting and Sampling

The Parana-Etendeka area represents one of the largest known continental flood basaltic provinces. It is constituted of volcanic and sub-volcanic rocks, with the majority being tholeiitic basalts and andesites with subordinate rhyolites, covering an area of around 1.2 ×

10<sup>6</sup> km<sup>2</sup> in southern Brazil (mainly), northern Argentina, Uruguay and Paraguay. Based on available radiometric data, it appears that these huge magmatic eruptions occurred between 133 and 132 Ma (Renne *et al.*, 1992, 1996).

Intra-continental volcanism that crop outs around the basaltic traps at the present time is younger, and comprises basaltic and andesitic dikes. The most important mafic dike swarms in Brazil occur in the Ponta Grossa (PG) region (Figure 1) and are associated with the flood basalt suites of the Paraná basin (Piccirillo *et al.*, 1990; Brandt *et al.*, 2010). The region is cut by hundred of dikes, predominantly basaltic and andesitic composition. There is now a general agreement that PG dikes were probably feeders of the stratovolcanoes built in northern Paraná (Sial *et al.*, 1987). Renne *et al.* (1996) reported a comprehensive geochronological study provided numerous 40Ar/ 39Ar high quality plateau ages. The age-probability distribution for the dominant pulse (131.4 ± 0.4 to 129.2 ± 0.4 Ma) shows a pronounced peak at 130.5 Ma. Thus, Ponta Grossa dikes are younger than the southern Paraná Magmatic Province lavas, which occurred at 133-132 Ma (Renne *et al.*, 1996).

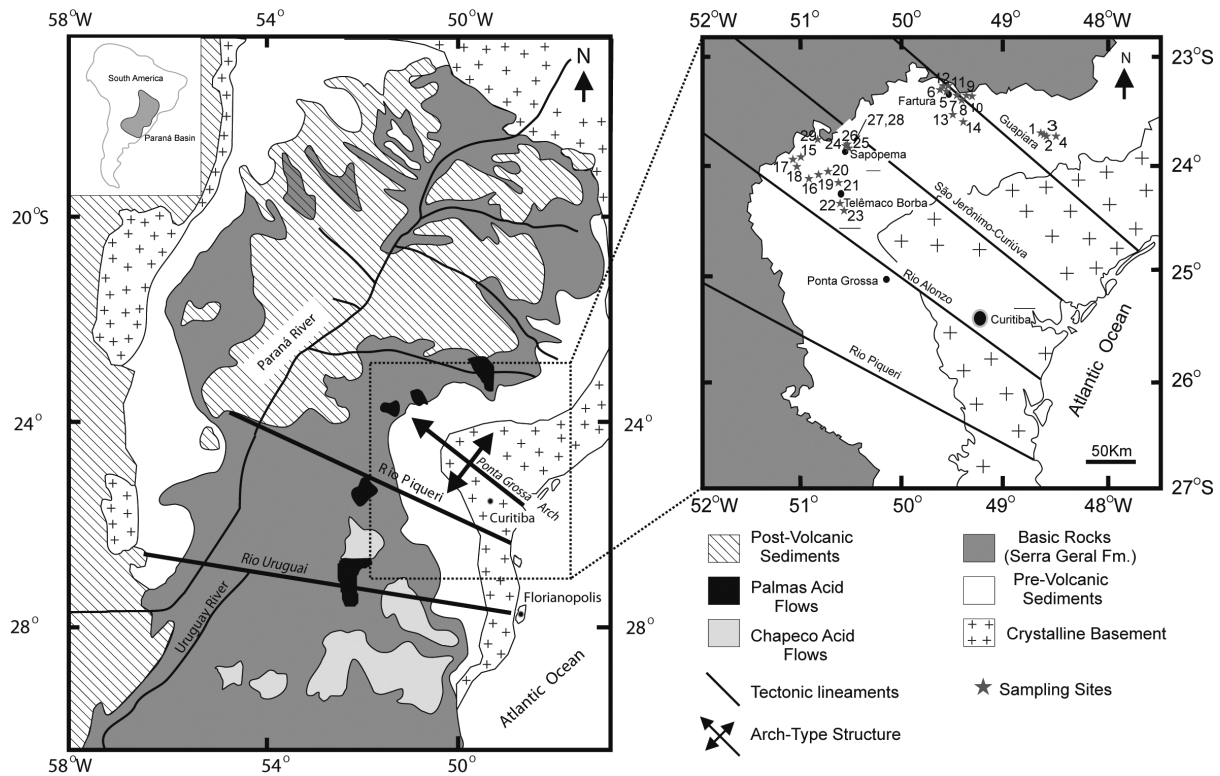


**Figure 1.** Simplified geologic map of Southern Brazil showing the location of studied sites (adopted from Brandt *et al.*, 2009 and Cejudo *et al.*, 2009).

We obtained 235 standard paleomagnetic cores belonging to 29 sites distributed along road outcrops in Ponta Grossa region, Southern Brazil (Figure 1). The samples were distributed throughout each dike both horizontally and vertically. In general, samples were obtained at least 30 cm distance from the dike edge (when possible). Cores were obtained with a gasoline-powered portable drill, and then oriented in most cases with both magnetic and sun compasses.

### Laboratory Procedures

Magnetic experiments were carried out to find out the carriers of remanent magnetization, to estimate their domains states and grain sizes and to obtain information about their paleomagnetic stability. From each of the 29 studied dikes, one sample was selected for these experiments, which included the measurement of low-field susceptibility versus temperature ( $k$ - $T$ ) curves, the determination of hysteresis parameters and the measurement of isothermal remanent magnetization (IRM) acquisition curves. All hysteresis measurements were carried out with the AGFM-Micromag apparatus, while continuous thermomagnetic curves were obtained using Bartington susceptibility bridge equipped with furnace.

Thermomagnetic curves were measured in air, heating the samples up to 600°C and cooling them down to room temperature. Curie

points ( $T_c$ ) were determined using the Prevot (1983)'s method. The most representative behaviour is reported on Figure 2a. It displays irreversible curves with a single ferromagnetic phase with a high Curie temperature near 550°C, which corresponds to low-Ti titanomagnetite or slightly Al- or Mg-substituted magnetite. We considered a curve to be reversible if the difference between initial magnetization before heating had started and final magnetization after cooling had been completed was less than  $\pm 10\%$ .

Hysteresis parameters  $J_s$  (saturation magnetization),  $J_{rs}$  (saturation remanence),  $H_c$  (coercivity) and  $H_{cr}$  (coercivity of remanence) were obtained from hysteresis (Figure 2b) and backfield curves. Analysis of the measurements was performed with the RockMagAnalyzer 1.0 software (Leonhardt, 2006). The obtained values point that studied samples can be match to the PSD (pseudo-single-domain) magnetic grains. This behavior might be also explained by a mixture of single-domain (SD) and multi-domain (MD) particles (Dunlop, 2002). IRM acquisition curves (Figure 2b) show that more than 95% of saturation magnetization (SIRM) was reached with applied fields of less than 150 mT. Thus IRM measurements point to low-coercivity phases as main remanence carriers.

Remanent magnetization measurements were performed at the 'Laboratorio Interinstitucional de Magnetismo Natural' in Campus

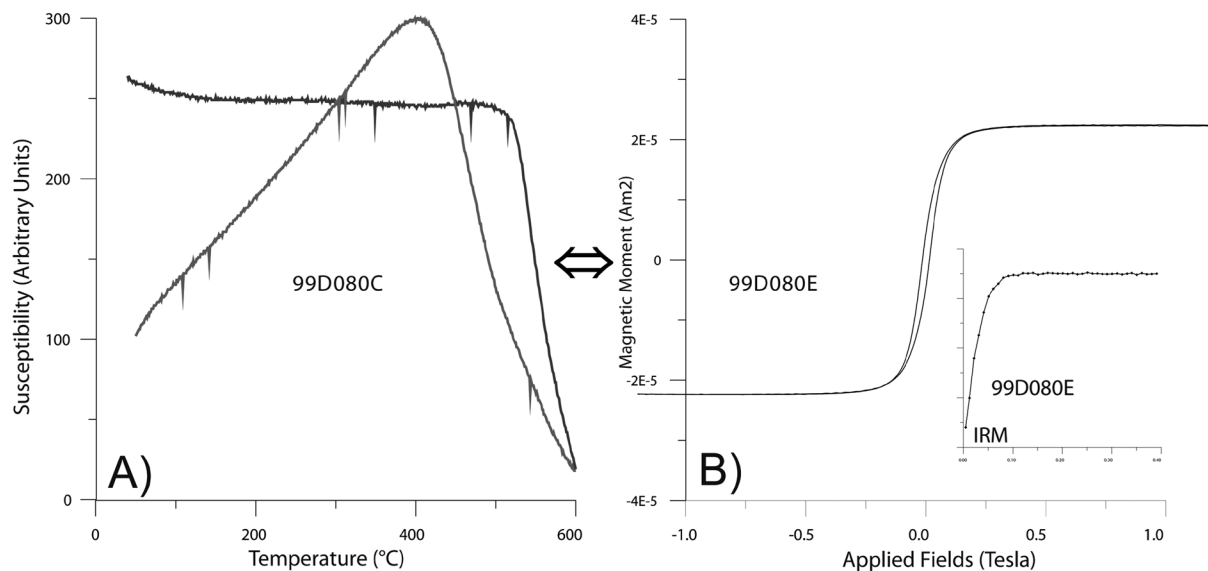


**Figure 2.** a) Susceptibility versus temperature (in air) curve of representative samples. b) Typical examples of hysteresis loop (corrected for dia/paramagnetism) of small chip samples from the studied volcanic units and associated IRM (isothermal remanent magnetization) curve.

Morelia (UNAM) with a spinner JR6 (nominal sensitivity  $\sim 10^{-9}$  Am<sup>2</sup>) magnetometer. Most of samples were cleaned by means of alternating field demagnetization using a LDA-3 demagnetizer, with 95 mT as maximum fields available. Eleven sites displayed a single paleomagnetic component (Figure 3, samples 99D015A), whereas in the remaining ones a viscous present-day normal-polarity overprint could also be observed that was easily removed (sample 99D010B). Some dikes however yielded relatively strong secondary components (sample 99D115A), which were removed after applying around 60 mT alternating fields. The origin of this overprint is probably related to hydrothermal alteration.

The direction of the characteristic magnetization (ChRM) was determined by the least squares method (Kirschvink, 1980), with 4 to 9 points being taken for the principal component analysis. The directions obtained were averaged by volcanic unit and the statistical parameters calculated assuming a Fisherian distribution.

### Main Results and Discussion

17 sites show normal polarity remanences, 10 sites show reverse polarities and one site have an outlier oblique direction, with negative inclination, separated 79° of the mean normal direction (calculated before exclude it; Figure 4). The mean paleomagnetic direction for the

**Table 1.** Paleomagnetic results of studied samples. *D, I* : declination and inclination of the site mean directions; *N* is number of specimens used; *k* and *a95* are Fisherian statistical parameters; VGP Long, VGP Lat : longitude and latitude of the virtual geomagnetic poles.

Site	Lat (south)	Long (west)	N	D	I	k	a95	Polarity	VGP Long [°E]	VGP Lat [°S]
PG02	24°11.423	48°32.856	7	187,4	42,6	72	7,2	R	227,4	-83,2
PG03	24°11.325	48°32.235	7	167,6	52,5	149	5,1	R	359,3	-76,0
PG04	24°11.269	48°32.654	7	202,8	22,3	162	5,6	R	195,8	-65,0
PG05	23°23.292	49°33.018	8	4,8	-38,9	748	2,8	N	204,6	-85,4
PG06	23°23.524	49°32.753	4	182,3	40,8	47	11,6	R	219,6	-87,9
PG07	23°23.356	49°32.468	5	184,8	19,9	191	5,6	R	150,5	-76,1
PG08	23°23.825	49°32.112	8	191,8	22,3	342	3,3	R	176,0	-73,7
PG09	23°20.072	49°28.498	7	19,7	-50,6	68	7,4	N	249,4	-70,8
PG10	23°21.226	49°28.786	8	339,7	-45,9	79	6,8	N	24,2	-71,3
PG11A	23°22.094	49°29.099	4	226,1	-50,5	58	9,6	O	174,4	-19,8
PG11B	23°22.094	49°29.099	4	15,4	-27,3	299	5,3	N	191,8	-73,0
PG12	23°22.511	49°29.638	6	179,2	30,2	125	6,1	R	124,4	-82,8
PG13	23°26.102	49°26.026	7	352,4	-43,8	258	4,2	N	21,5	-82,8
PG14	23°29.195	49°19.562	6	349,8	-41,8	192	4,8	N	34,9	-80,6
PG15	24°04.002	51°03.810	5	165,2	50,6	61	9,9	R	6,6	-75,0
PG16	24°11.103	51°04.012	5	169,2	43,9	106	7,5	R	27,9	-80,1
PG17	23°59.824	51°05.091	6	178,2	47,2	39	11,5	R	328,9	-85,3
PG18	24°08.105	51°00.181	7	342,9	-45,4	48	9,3	N	25,3	-74,3
PG19	24°09.324	50°58.474	6	12,9	-48,1	69	8,2	N	245,2	-77,5
PG20	24°13.512	50°55.681	6	18,6	-49,9	63	8,5	N	244,6	-72,3
PG21	24°15.715	50°53.593	5	14,6	-50,9	59	7,9	N	252,0	-75,2
PG22	24°26.463	50°44.253	6	11,4	-30,9	47	9,2	N	185,3	-76,8
PG23	24°25.091	50°42.341	5	8,2	-47,7	143	5,6	N	251,9	-81,5
PG24	23°50.687	50°37.158	6	4,6	-32,1	84	7,4	N	134,0	-82,3
PG25	23°50.977	50°37.057	6	359,6	-34,7	66	8,5	N	124,8	-85,2
PG27	23°51.950	50°36.975	5	356,2	-35,4	38	10,8	N	89,3	-84,4
PG28	23°52.474	50°36.601	6	1,7	-41,8	43	9,2	N	227,5	-88,4
PG29	23°54.231	50°35.388	1	344,5	-47,1	N.D	N.D	N	18,5	-75,4

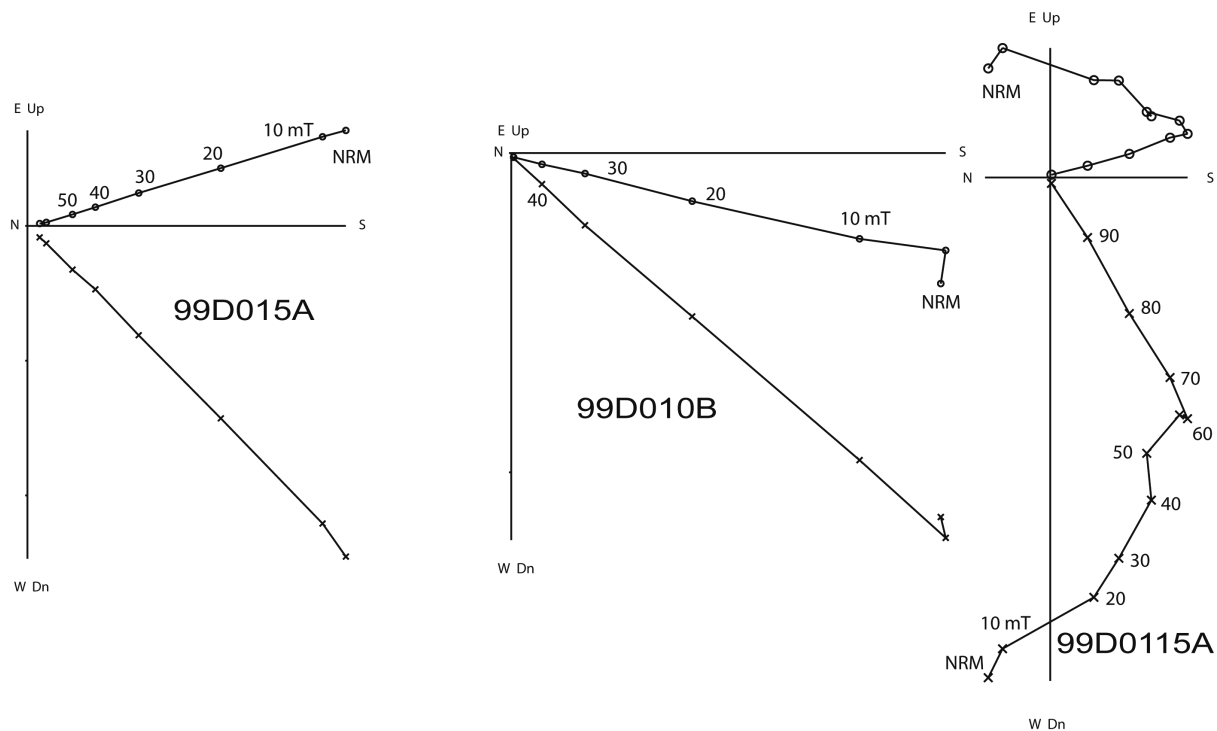


**Figure 3.** Orthogonal vector plots of stepwise alternative field demagnetization of three representative specimens.

normal polarity sites is  $I = -42.6^\circ$ ,  $D = 2.2^\circ$ ,  $k = 46.9$ ,  $a_{95} = 5.3^\circ$ ,  $N = 17$  ( $k$  is precision parameter and  $N$  number of sites), while reversely magnetized sites give a mean direction with  $I = 37.8^\circ$ ,  $D = 182.2^\circ$ ,  $k = 27.62$ ,  $a_{95} = 9.3^\circ$ ,  $N = 10$ . The reversal test as defined by McFadden and Lowes (1981) is accepted at the 95% confidence level and the reversal test from McFadden and McElhinny (1990) is positive with classification B ( $gc = 9.58^\circ$ ;  $go = 4.8^\circ$ ). This ensures that the secondary remanent magnetizations were successfully removed and the sampling adequately averaged the palaeosecular variation.

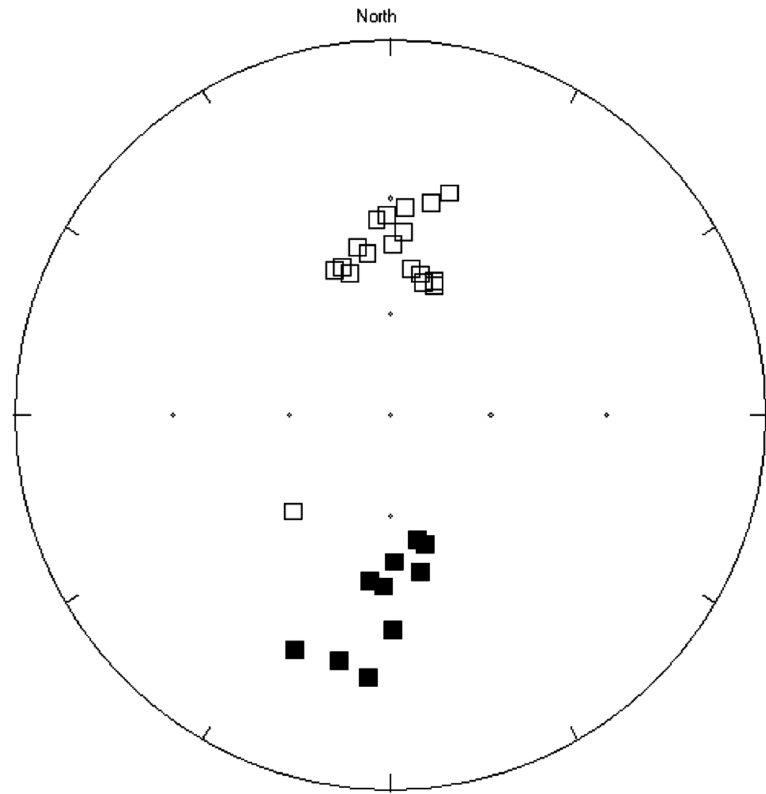
For both sets, the quantil-quantil (Q-Q) plot for declinations using the uniform model is approximately linear, passing through the origin with a slope near  $45^\circ$  (Figure 5). The Q-Q Co-Inclination plot with exponential model is also linear, with a slope that gives an estimated  $k = 58.82$ . The Q-Q plot for two variables is approximately linear, passing through the origin and with a slope that give an estimate  $k = 42.16$ . The three  $k$  estimate values are statistically undistinguishable at 95% level using an F-test. These graphical tests suggest that the underlying distributions are fisherian.

The distribution of the site-mean VGPs is somewhat elongated (Figure 6), with

maximum elongation direction along the  $24^\circ$ - $204^\circ$  meridian. The eigenvalues of the VGP orientation matrix are  $t_1 = 25.714$ ;  $t_2 = 0.987$ ;  $t_3 = 0.299$ , then the elongation index is 3.3. Similar configuration was also found for coeval VGPs (Mena *et al.*, 2006, 2011). However, we consider the elongation not significant, since the VGP distribution yields a reasonably good fit with fisherian distribution when probability plots as well as formal testing procedures are used.

The VGPs quantil-quantil (Q-Q) plots are consistent with a fisherian distribution (Figure 7), with slopes that give estimated  $k = 43.5$  from colatitudes and  $k = 73.1$  from two variables. Using an F-test these values are statistically undistinguishable, at 95% confidence level, of the value  $k = 39.6$  estimate with the VGPs. Employing formal testing procedures, we obtain the following results for the modified statistics of Kolmogorov-Smirnov and Kuiper ( $Dn^*$ ,  $Vn^*$ ,  $MU(Vn)$ ,  $ME(Dn)$  and  $MN(Dn)$ ; Fisher *et al.*, 1987): Longitude test:  $Dn^* = 0.8677$ ;  $Vn^* = 1.2862$ ;  $MU(Vn) = 1.1780$ ; colatitude test:  $Dn^* = 0.6381$ ;  $Vn^* = 1.0538$ ;  $ME(Dn) = 0.6162$ ; Two-variable test:  $Dn^* = 0.7390$ ;  $Vn^* = 1.3542$ ;  $MN(Dn) = 0.7408$ . All values suggesting no departure from the Fisher model.

**Figure 4.** Stereoplot for site mean paleodirections corresponding to all 28 sites where reliable results are obtained.



Considering the PGVs from sites with  $\alpha_{95} < 10^\circ$  (excluding PG6, PG17 and PG27 and the oblique site PG11a) the paleomagnetic pole (PP) is located at  $222.0^\circ$  longitude E,  $88.1^\circ$  latitude S,  $N = 24$ ,  $K = 35.68$ ,  $A_{95} = 5.0^\circ$ . The

inclusion of all sites into the mean calculation gives:  $222.4^\circ$  longitude E,  $88.4^\circ$  latitude S,  $N = 27$ ,  $K = 39.61$ ,  $A_{95} = 4.5^\circ$ , which is not significantly different.

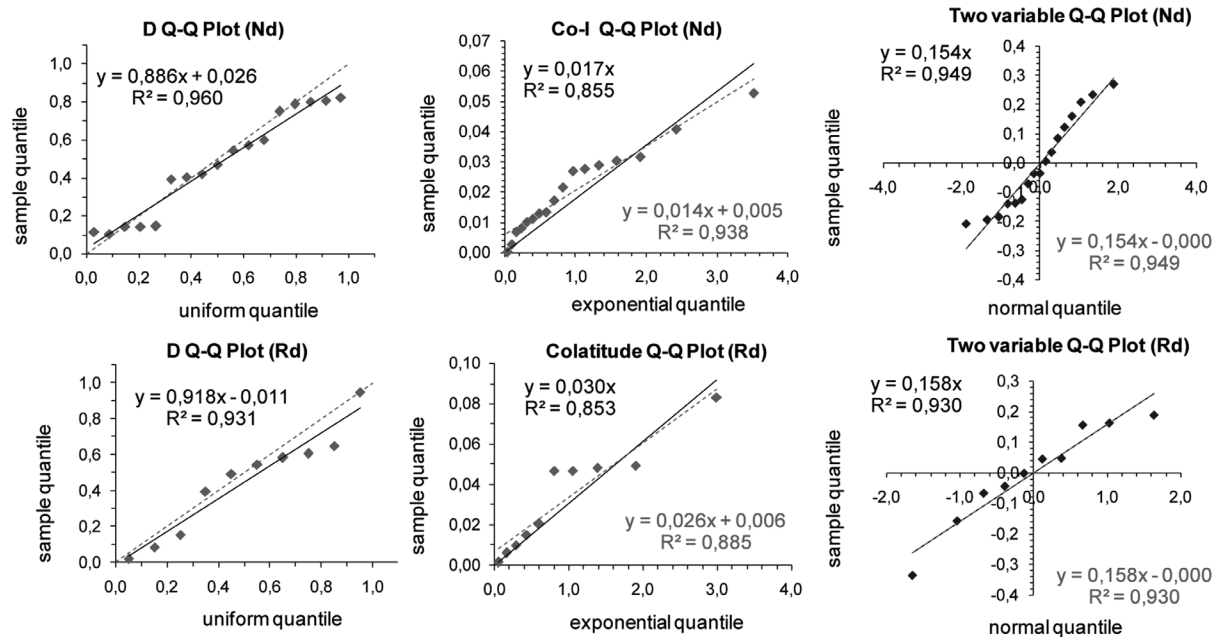


**Figure 5.** Probability plots for checking goodness of fit of the paleodirections to the Fisher distribution.

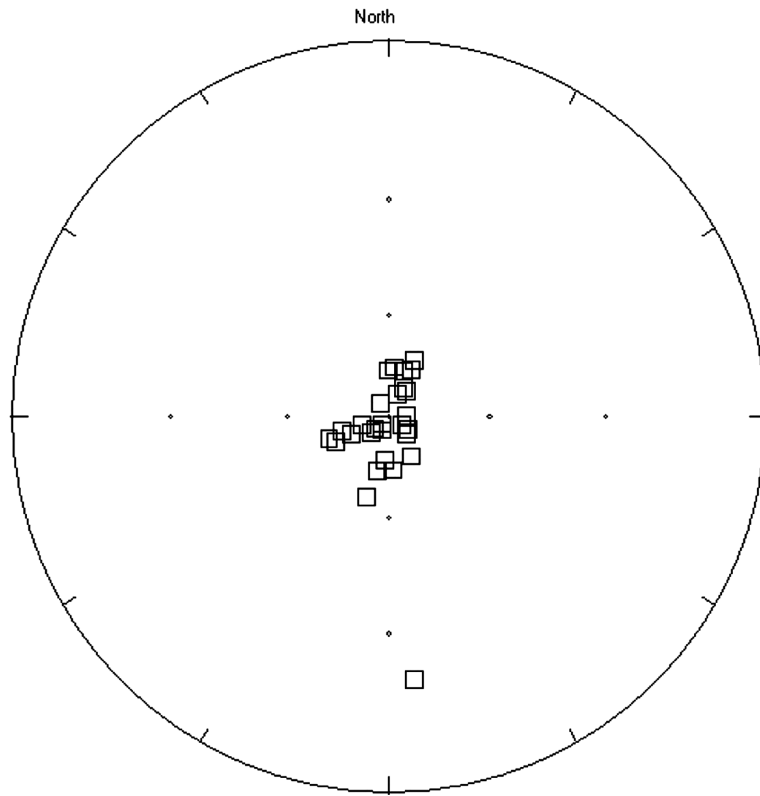


**Figure 6.** South VGPs distribution from 28 sites.

The mean paleomagnetic pole obtained in this study is shown in the present geographical reference frame in Figure 8 and listed in Table 2 together with previously published South American poles. In general, the pole obtained in this study, agrees reasonably well with other pole positions, in particular with Misiones (Argentina), Central Paraná Magmatic Province, Florianopolis Dikes (Brazil), Los Adobos (Geuna *et al.*, 2000) poles. However, some other similar age paleomagnetic poles (Central and Northern Paraná Basin in Brazil and Arapey Formation in Uruguay) are clear outliers. As initially suggested by Ernesto *et al.* (1996) and recently confirmed by

Goguitchaichvili *et al.* (2013), this may be due to some local tectonic rotations or insufficient sampling to average the paleosecular variation as well as to unrecognized structural disturbances. Overall, the Ponta Grossa poles are significantly different from the pole position estimated from the hotspot reconstruction (Muller *et al.*, 1993). This fact is attributed by several authors (i.e. Alva-Valdivia *et al.*, 2003, Cervantes *et al.*, 2010, Goguitchaichvili *et al.*, 2013) as cause of the true polar wander or hotspot motion. Somoza and Zaffarana (2008) analyzed the mid-Cretaceous poles for South America, concluding that there is no detectable motion with respect of the paleomagnetic

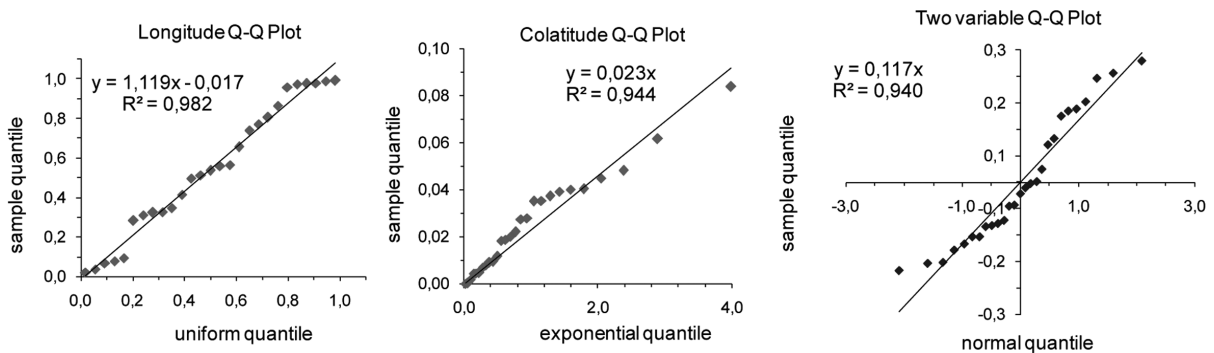


**Figure 7.** Probability plots for checking goodness of fit of the VGPs to the Fisher distribution.

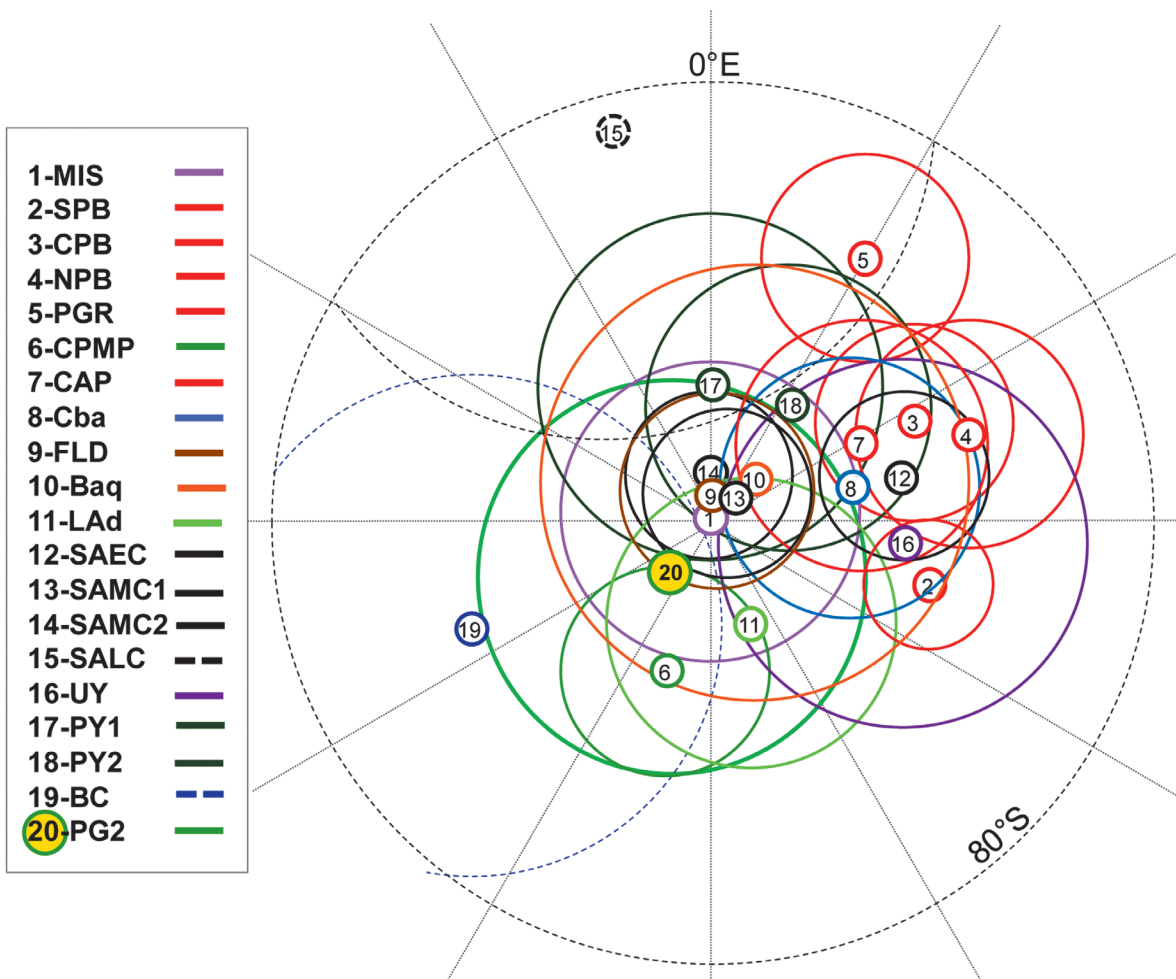
**Table 2.** Selected Cretaceous paleomagnetic poles. P= number assigned to paleomagnetic pole (PP) in Figures X; long E, lat S, A95= longitude, latitude and semi angle of 95% confidence of the PPs.

Table 4. Selected Cretaceous PPs.							
	Locality	P	Long (°E)	Lat (°S)	$\alpha_{95}$	Age (Ma)	References
MIS:	Misiones	1	339.1	89.7	4.2	?	Mena <i>et al.</i> (2011)
SPB:	Southern Paraná Basin	2	106.2	84	1.5	~133	Raposo and Ernesto (1995)
CPB:	Central Paraná Basin	3	64.4	84.1	2.3	~132	Raposo and Ernesto (1995)
NPB:	Northern Paraná Basin	4	71.4	83	2.4	132	Ernesto <i>et al.</i> (1999)
PGR:	Ponta Grossa dikes (Brazil)	5	30.3	82.4	2	131–129	Raposo and Ernesto (1995)
CPMP:	Central Paraná Magmatic Province, Brazil	6	197.9	85.7	2.6	133–132	Alva-Valdivia <i>et al.</i> (2003)
CAP:	Central Alkaline Province, Paraguay	7	62.3	85.4	3.1	130–127	Ernesto <i>et al.</i> (1996)
Cba:	Sierras Pampeanas, Córdoba, Argentina	8	75.9	86	3.3	~130	Geuna and Vizán (1998)
FLD:	Florianopolis dikes, Southern Brazil	9	3.3	89.1	2.7	128–119	Raposo <i>et al.</i> (1998)
Baq:	Baqueró Group	10	42.7	88.2	5.5	119	Somoza <i>et al.</i> (2005)
LAd:	Fm. Los Adobes	11	159	87	3.8	130–112	Geuna <i>et al.</i> (2000)
SAEC:	Mean South America Early Cretaceous	12	76.4	84.7	2	135–130	Somoza and Zaffarana (2008)
SAMC1:	Mean South America Middle Cretaceous	13	33.8	89.1	2.4	125–100	Somoza and Zaffarana (2008)
SAMC2:	Mean South America Middle Cretaceous	14	354.1	88.7	2.3	125–100	Somoza and Zaffarana (2008)
SALC:	Mean South America Late Cretaceous	15	345.1	80.6	4.3	85	Somoza and Zaffarana (2008)
UY:	Fm. Arapey	16	95.8	84.8	4.2	~130	Solano <i>et al.</i> (2010)
PY1:	Fm. Alto Paraguay 18	17	359.2	86.2	4.3	~134	Goguitchaichvili <i>et al.</i> , 2012
PY2:	Fm. Alto Paraguay 16	18	34.1	86.1	3.6	~134	Goguitchaichvili <i>et al.</i> , 2013
BC	Reference poles at 135 Ma	19	246.5	83.2	5.5	135	Besse and Courtillot (2002)
PG2	Ponta Grossa	20	222.0	88.1	5		This study

axis for the interval 125 to 100 Ma. Somoza and Zaffrana (2008)'s study also shows that the corresponding paleolatitudes are inconsistent with true polar wander, supporting that the angular discrepancies between the paleomagnetic and fixed hotspot reference frames are due to relative motion of the Atlantic hotspots. The apparent polar standstill of South America has been documented for Eurasia and possibly for the Pacific plate during mid-Cretaceous times (Sager, 2006).

The location of our paleomagnetic poles significantly differs from early Ponta Grossa poles obtained by Raposo and Ernesto (1995). However, these new poles agree well (within uncertainties) with the reference poles given by Besse and Courtillot (2002). This attests that our results should be considered as most precise determination of Cretaceous paleomagnetic pole positions for stable South America.

The VGPs scatter was calculated according to  $S_p$  (Cox, 1969) where  $S_p$  is the total angular



**Figure 8.** Paleomagnetic poles with 95% confidence circles for Ponta Grossa dikes and previously published Cretaceous PPs with their confidence limits. 1. Misiones (Mena *et al.*, 2011), 2. Southern Paraná Basin (Raposo and Ernesto, 1995), 3. Central Paraná Basin (Raposo and Ernesto, 1995), 4. Northern Paraná Basin (Ernesto *et al.*, 1999), 5. Ponta Grossa Dikes (Raposo and Ernesto, 1995), 6. Central Paraná Magmatic Province (Alva-Valdivia *et al.*, 2003), 7. Central Alkaline Province, Paraguay (Ernesto *et al.*, 1996), 8. Sierras Pampeanas (Geuna and Vizán, 1998), 9. Florianópolis Dikes (Raposo *et al.*, 1998), 10. Baqueró Group (Somoza *et al.*, 2005), 11. Los Adobos (Geuna *et al.*, 2000), 12. Mean Early Cretaceous (Somoza and Zafarana, 2008), 13. Mean Middle Cretaceous (Somoza and Zafarana, 2008), 14. Mean Cretaceous (Somoza and Zafarana, 2008), 15. Mean Late Cretaceous, (Somoza and Zafarana, 2008). 16. Arapey (Solano *et al.*, 2010), 17. Alto Paraguay 18 (Gogutchichvili *et al.*, 2012), 18. Alto Paraguay 16 (Gogutchichvili *et al.*, 2013), 19. Reference Poles at 135 Ma (Besse and Courtillot, 2002), Ponta Grossa (This study).

dispersion,  $D_i$  is the angular distance of the  $i$ -th VGP to the PP and  $N$  is the number of sites used in the calculation. Thereby  $S_p=12.9^\circ$ . The paleosecular variation (PSV) was estimate according to McElhinny and McFadden (1997) by where  $S_w = 81/K^{-1/2}$  is the within-site scatter,  $K$  being Fisher concentration parameter for poles estimate from direction concentration parameter ( $k$ ) according to  $K = 8k(5 + 18\sin^2 \lambda + 9\sin^4 \lambda)$ ,  $\lambda$  is the site paleolatitude, and  $n_i$  is the number of directions from  $i$ -th site. The calculated PSV is  $S_b=12.3^\circ$ , with a 95% confidence interval  $[10.3^\circ; 15.2^\circ]$ , which agrees well with the expected value for this latitude. The  $S_b$  values here obtained agree well with the selected data reported for the Cretaceous Normal Superchron (Biggin *et al.*, 2008) between 125 to 84 Ma. This supports that the Earth's magnetic field maintained similar characteristics before and during CNS, in disagreement with previous studies.

### Acknowledgment

The financial support for this work was provided by UNAM DGAPA PAPIIT projects IN-105215, 107114 and IA-104215, as well by CONACYT project 129653. This work was also funded by CGL2012-32149 project (Ministerio de Economía y Competitividad, Spain) and the European Regional Development Fund (ERDF).

### Bibliography

- Alva-Valdivia L.M., Goguitchaichvili A., Urrutia-Fucugauchi J., Riisager J., Riisager P., 2003, Paleomagnetic poles and paleosecular variation of basalts from Paraná Province, Brazil: geomagnetic and geodynamic implications., *Phys. Earth Planet. Inter.*, 138, 183-196.
- Besse J., Courtillot V., 2002, Apparent and true polar wander and the geometry of the geomagnetic field over the last 200 Myr, *J. Geophys. Res.*, 107(B11), 1-31.
- Biggin A.J., van Hinsbergen D.J., Langerais C.G., Straathof G.B., Deenen M.H.L., 2008, Geomagnetic secular variation in the Cretaceous Normal Superchron and in the Jurassic, *Physics Earth Planet. Int.*, 169, 3-19.
- Brandt D., Hartmann G.A., Yokoyama E., Catelani E.L., Trindade R.I.F., 2009, Paleointensity data from Early Cretaceous Ponta Grossa dikes (Brazil) using a multisample method, *Earth, Planets Space*, 61, 41-49.
- Cande S.C., Kent D.V., 1995, Revised calibration of the geomagnetic polarity time scale for the Late Cretaceous and Cenozoic, *J. Geophys. Res.*, 100(B4), 6093-6095.
- Cejudo Ruiz R., Goguitchaichvili A., Morales J., Trindade R.I.F., Alva Valdivia L.M., Urrutia-Fucugauchi J., 2009, Absolute Thellier paleointensities from Ponta Grossa dikes (southern Brazil) and the early Cretaceous geomagnetic field strength. *Geofísica Internacional*, 48, 243-252.
- Cox A., 1969, Research note: Confidence limits for the precision parameter,  $K$ , *Geophys. J. Roy. Astron. Soc.*, 17, 545-549.
- Dunlop D.J., 2002, Theory and application of the Day plot (Mrs/Ms versus Hcr/Hc), Theoretical curves and tests using titanomagnetite data, *J. Geophys. Res.*, 107.
- Ernesto M., Raposo I.B., Marques L., Renne P., Diogo L., Min M., 1999, Paleomagnetism, geochemistry and  $^{40}\text{Ar}/^{39}\text{Ar}$  dating of the Northeastern Paraná Magmatic Province., *J. Geodyn.*, 28, 321-340.
- Ernesto M., Comin-Chiaramonti P., Gomes C.B., Castillo A.M.C., Velazquez J.C., 1996, Palaeomagnetic data from the Central Alkaline Province, eastern Paraguay, Alkaline magmatism in Central-Eastern Paraguay. University of Sao Paulo: 85-102.
- Ernesto M., Pacca I.G., Hyodo F.Y., Nardy A.J.R., 1990, Paleomagnetism of the Mesozoic Serra Geral Formation, southern Brazil, *Phys. Earth Planet. Inter.*, 64, 153-175.
- Fisher N.I., Lewis T., Embleton B.J.J., 1987, Statistical analysis of spherical data, Cambridge University Press.
- Kirschvink J.L., 1980, The Least-Squares Line and Plane and the Analysis of Paleomagnetic Data. *Geophysical Journal of the Royal Astronomical Society*, 62, 3, 699-718.
- McElhinny M.W., McFadden P.L., 1997, Paleosecular variation over the past 5 Myr based on a new generalized database, *Geophys. J. Int.*, 131, 240-252.
- McFadden P.L., McElhinny M.W., 1990, Classification of the reversal test in paleomagnetism, *Geophys. J. Int.*, 103, 725-729.

- McFadden P.L., Lowes F.J., 1981, The discrimination of mean directions drawn from Fisher distributions, *Geophys. J. R. Astr. Soc.*, 67, 19-33.
- Mena M., Goguitchaichvili A., Solano M.C., Vilas J.F., 2011, Paleosecular variation and absolute geomagnetic paleointensity records retrieved from the Early Cretaceous Posadas Formation (Misiones, Argentina), *Studia Geophysica et Geodaetica*, 55, 279-309.
- Mena M., Orgeira M.J., Lagorio S.L., 2006, Paleomagnetism, rock-magnetism and geochemical aspects of early Cretaceous basalts of the Paraná Magmatic Province, Misiones, Argentina, *Earth Planets Space*, 58, 1283-1293.
- Leonhardt R., 2006, Analyzing rock magnetic measurements: The RockMagAnalyzer 1.0 software, *Computers and Geosciences*, 32, 9, 1420-1431.
- Piccirillo E.M., Melfi A.J., 1988, The Mesozoic flood volcanism from the Paraná basin (Brazil), Petrogenetic and geophysical aspects, Iag-Usp, São Paulo, Brazil, 600 pp.
- Prévot M., Mankinen E.A., Grommé S., Lecaille A., 1983, High paleointensities of the geomagnetic field from basalts from the mid-Atlantic ridge. *J. Geophys. Res.*, 88, 2316-2326.
- Raposo M.I.B., Ernesto M., Renne P.R., 1998, Paleomagnetism and  $^{40}\text{Ar}/^{39}\text{Ar}$  dating of the Early Cretaceous Florianópolis dike swarm (Santa Catarina Island), Southern Brazil, *Earth Planet. Sci. Lett.*, 108, 275-290.
- Raposo M.I.B., Ernesto M., 1995, An Early Cretaceous paleomagnetic pole from Ponta Grossa dykes (Brazil): implications for the South America Mesozoic APWP, *J. Geophys. Res.*, 100, 20095-20109.
- Renne P.R., Decart K.; Ernesto M., Féarud G. Piccirillo E.M., 1996, Age of the Ponta Grossa dike swarm (Brazil), and implications to Paraná flood volcanism. *Earth Planet. Sci. Lett.*, 144, 199-212.
- Renne P.R., Ernesto M., Pacca I.G., Coe R.S., Glen, J.M., Prévot M. and Perrin M. (1992), The Age of Paraná Flood Volcanism, Rifting of Gondwanaland, and the Jurassic-Cretaceous Boundary, *Science* 258, 975-979.
- Sager, W.W., 2006. Cretaceous paleomagnetic apparent polar wander path for the Pacific plate calculated from Deep Sea Drilling Project and Ocean Drilling Project Program basalt cores. *Phys. Earth Planet. Inter.*, 156, 329-349.
- Seton M. Gaina C. Muller R.D., Heine C., 2009, Mid-Cretaceous seafloor spreading pulse: Fact or fiction?, *Geology*, 37, 687-690.
- Sial A.N., Oliveira E.P., Choudhuri A., 1987, Mafic dyke swarms of Brazil. In: H.C. Halls and W.F. Fahrig (Editors), Mafic Dyke Swarms in Brazil. *Geol. Assoc. Can. Spec. Pap.*, 34, 467-481.
- Somoza R., Zaffarana C.B., 2008, Mid-Cretaceous polar standstill of South America, motion of the Atlantic hotspots and the birth of the Andean cordillera. *Earth Planet. Sci. Lett.*, 271, 267-277.
- Tarduno J.A., Cottrell R.D., Smirnov A.V., 2002, The Cretaceous superchron geodynamo: observations near the tangent cylinder. PNAS, 99, 14020-14025.
- thermomagnetic study on rift valley pillow basalts from the mid-Atlantic ridge. *J. Geophys. Res.*, 88, 2316-2326.
- Taylor B., 2006. The single largest oceanic plateau: Ontong Java-Manihiki-Hikurangi. *Earth Planet. Sci. Lett.*, 241, 372-380.
- Torsvik T.H., Van der Voo R., Redfield T.F., 2002, Relative hotspot motion versus true polar wander. *Earth Planet. Sci. Lett.* 202, 185-200.

## Modeling sea-level change, inundation scenarios, and their effect on the Colola Beach Reserve – a nesting-habitat of the black sea turtle, Michoacán, Mexico

Yuritzi Calvillo García, María Teresa Ramírez-Herrera\*, Carlos Delgado-Trejo, Gabriel Legorreta-Paulin and Néstor Corona

Received: April 01, 2014; accepted: December 02, 2014; published on line: March 31, 2015

### Resumen

Los efectos del cambio climático variarán regionalmente. Sin embargo, la temperatura media aumentará en todo el mundo, y el consiguiente aumento del nivel del mar afectará a la mayoría de las playas de la costa y en consecuencia a todas las poblaciones de tortugas marinas en el corto, mediano y largo plazo. Se necesitan modelos de la inundación esperada en la playa y de la pérdida del hábitat de anidación debido al aumento del nivel del mar para evaluar los cambios costeros y la conservación de las áreas de anidación de las tortugas marinas. La playa de Colola en Michoacán, México, es la principal zona de anidación de la tortuga marina negra (*Chelonia mydas agassizii*), también conocida como la tortuga verde del Pacífico Oriental, una especie incluida en la lista de peligro de extinción. Aquí evaluamos los efectos del cambio del nivel del mar en esta playa con tres escenarios diferentes. Con este fin, realizamos un levantamiento topográfico en detalle de la playa de Colola para producir un modelo de elevación digital

(DEM) y el modelo de inundación esperada en la playa que acompaña a aumentos del nivel del mar de 0,5 m, 1,40 m y 5 m; registramos los sitios de anidación de la tortugas marinas y sus áreas utilizando sistemas de posicionamiento global (GPS), y finalmente modelamos estos escenarios usando sistemas de información geográfica (SIG), imágenes de satélite y un modelo de elevación digital. Los modelos producidos sugieren que los aumentos de 0,5 m y 1,40 m afectarían a la zona de la playa Colola reduciéndola. Mientras que un aumento del nivel del mar de 5 m tendría un efecto dramático, con la pérdida del 54% de la playa y zona de anidación. Este enfoque y escenarios previstos a través de levantamiento topográfico detallado y modelado con SIG deben ayudar en la creación de estrategias para la conservación de las poblaciones de tortugas marinas en esta reserva y en otros lugares.

Palabras Clave: Cambio climático, aumento del nivel del mar, inundación de la playa, modelación SIG, tortuga marina, *Cheloniemydas agassizii*.

Y. Calvillo García  
Instituto de Investigaciones  
sobre los Recursos Naturales  
Universidad Michoacana  
de San Nicolás de Hidalgo

Laboratorio Universitario de Geofísica Ambiental  
Centro de Investigaciones en Geografía Ambiental  
Universidad Nacional Autónoma de México  
Circuito exterior, Cd. Universitaria  
04510 México D.F., México  
[tramirez@igg.unam.mx](mailto:tramirez@igg.unam.mx)

M. T. Ramírez-Herrera\*  
Laboratorio Universitario de Geofísica Ambiental and  
Instituto de Geografía  
Universidad Nacional Autónoma de México  
Ciudad Universitaria  
Delegación Coyoacán, 04510  
México D.F., México  
\*Corresponding author: [tramirez@igg.unam.mx](mailto:tramirez@igg.unam.mx)

C. Delgado-Trejo  
Instituto de Investigaciones  
sobre los Recursos Naturales  
Universidad Michoacana  
de San Nicolás de Hidalgo

G. Legorreta-Paulin  
Instituto de Geografía  
Universidad Nacional Autónoma de México  
Ciudad Universitaria  
Delegación Coyoacán, 04510  
México D.F., México

N. Corona  
Centro de Estudios de Geografía Humana  
El Colegio de Michoacán  
La Piedad Michoacán, México

## Abstract

The effects of climate change will vary regionally. However, the mean temperature will rise worldwide, and the concomitant rise in sea level will affect most coastal beaches and consequently all populations of sea turtles in the short, medium and long term. Models of expected beach inundation and loss of nesting habitat due to sea-level rises are required to assess coastal changes and the conservation of the sea-turtle nesting areas. Colola Beach in Michocán, Mexico, is the main nesting area of the black sea-turtle (*Chelonia mydas agassizii*), also referred as Eastern Pacific green turtle, a species listed as being in danger of extinction. We assessed the effects of sea-level change in this beach using three different scenarios. With this purpose, we surveyed the topography of Colola Beach in detail to produce a digital elevation model (DEM) and modeled beach

inundation expected to accompany sea-level rises of 0.5 m, 1.40 m and 5 m; recorded sea-turtle nesting sites and areas using global positioning systems (GPS), and finally modeled using geographic information systems (GIS), satellite images and a digital elevation model. The produced models suggest that rises of 0.5 m or 1.40 m would affect the Colola beach area by reducing it. Most significantly, a sea-level rise of 5 m would have a dramatic effect, with the loss of 54% of the beach and nesting area. This approach and predicted scenarios through detailed topographic survey and GIS modeling should assist in creating strategies for the conservation of the sea turtle populations in this beach reserve and elsewhere.

**Keywords:** Climate change, sea-level rise, beach inundation, GIS modeling, sea turtle, *Cheloniemydas agassizii*

---

## Introduction

It is expected that climate change will directly affect individual organisms, populations, species distribution and ecosystem function (IPCC, 2002). The rise in sea level is probably the most important anthropogenic effect of climate change in the present century (Grinsted *et al.*, 2009). It threatens to inundate and erode beaches, i.e. the principal nesting areas of sea turtles, where infrastructure or natural obstacles hinder the landward retreat of the beaches (Drews and Fonseca, 2009).

The life cycle and biology of sea turtles are closely linked to their terrestrial environment. Changing conditions in nesting and foraging beach areas, which can limit their potential for growth and reproduction, are severe threats for populations that are already under pressure at the global level owing to high mortality as a result of fisheries, over-exploitation and habitat modification (Lutcavage *et al.*, 1997).

Sea turtles are an ancient species group whose adaptive capacity is determined by the speed and geographic scale at which their environment changes. True, they survived the four great glaciations of the Pleistocene and many other, albeit lesser, events that caused the extinction of the great mammals, and they have retained physiological mechanisms that have allowed them to mitigate the effect of events whose cycles are of short or medium

term. However, the likely effects of processes associated with the present accelerated increase in temperature are unknown.

In all sea turtle species, reproductive success depends mainly on the availability of terrestrial habitat. Sea turtles can emerge onto the beaches to deposit several batches of eggs during the course of a nesting season (Miller, 1997). The loss of beach nesting habitat up to 2080 through a sea level rise of 4.2 mm per year suggests potentially adverse effects on their reproductive success and hence on their survival (Church *et al.*, 2001; IPCC, 2007).

Sea turtle species are of interest for conservation and they are increasingly seen to be affected by a series of natural and anthropogenic hazards. However, despite the many efforts in the past two decades to understand and mitigate the threats to these turtles (Lutcavage *et al.*, 1997; Watson *et al.*, 2005), until recently little attention has been paid to the threat posed to this group by climate change (Mrosovsky *et al.*, 1984; Davenport, 1989).

The place where the turtles make their nests can affect their reproductive success: the fitness for survival and the success of their progeny (Bjordal and Bolten, 1992). Although it is not entirely clear why some beaches are favored by turtles for egg-laying, Mortimer (1982) identifies the following general requirements for a nesting beach.

1. The beach must be accessible from the sea.
2. The beach must be high enough to prevent the inundation of the eggs through wave action or through a rise in the water table.
3. The substratum must allow the diffusion of gases.
4. The substratum must be humid and sufficiently fine-grained to prevent the collapse of the nest chamber during its construction.

The slope of the beach is a function of various factors that include the geomorphology of the zone, wave action, storms and the grain size of the sand (Bird, 1996). The rise in sea level and an increase in the frequency and intensity of hurricanes will increasingly affect beaches.

Studies of changes in sea level through global warming predict a range of scenarios. Rises of 0.18 to 0.59 m are expected by the end of the 21st century (IPCC, 2007). A rise in temperature of between 1.5° and 5°C will bring a possible rise of 0.20 to 1.65 m in sea level (Lara, 2008). Predictions have included a rise of 0.75 to 1.90 m for the period of 1990 to 2100, (Vermeer and Rahmstorf 2009), of 0.26 to 0.39 m by 2025, and of 0.91 to 1.36 m by 2075 (Hoffman *et al.*, 1983).

The World Wildlife Fund (Fish and Drews, 2009) estimates that climate change will adversely affect marine turtle populations as follows:

1. Mortality of the young through desiccation or flooding of the incubatory substratum through a rise in the water table.
2. Loss of the nesting habitat through erosion and sea inundation of the beaches.
3. Distortion in the sex ratio of the young, through failure to produce males.

Studies of sea-level rises on beaches used for nesting by marine turtles (Delgado and Alvarado, 2005) have shown a loss of ~70% of the reproductive population of the black sea-turtle (*Chelonia agassizi* = *Chelonia mydas agassizi*), also referred to as Eastern Pacific green turtle, a species classified as endangered (World Conservation Union, 2001). The Official Mexican Norm NOM-59-SEMARNAT (Official memorandum 6 March 2002) lists it in the category "in danger of extinction". Sea turtles are of great tourist economic value and are highly vulnerable to human activity, at least during nesting. Their inclusion in most lists

of threatened species or those in danger of extinction reflects their over-exploitation by humans (Pritchard, 1997).

In Mexico, the loss of nesting habitat through rises in mean sea level has not been evaluated. Models of local beach inundation by sea-level rise are important in determining the risk; the present study is one of the first attempts to test it in Mexico. This study considers a range of scenarios involving sea-level rise caused by global warming, and evaluates the likely effects of the loss of beach nesting habitat in Colola Beach, Michoacán, Mexico.

### Study area

Colola Beach (18°17'47" N, 103°24'3" W) is the principal nesting area of the black turtle (*Chelonia mydas agassizii*). It is located along the Pacific coast of Mexico, a tectonically active coast. The Pacific coast in Michoacán is bordered inland by rough topography of the folded and fault-blocked mountains of the Sierra Madre del Sur and by narrow beaches (Figure 1). Colola beach is 4.8 km long and an average 150 m wide, reaching more than 200 m width in some sectors. It extends in NW-SE direction, with two minor rivers (arroyos) flowing to the east and west of the beach, and a rocky granite outcrop defines its western end, while the village of Colola is at its eastern end. The beach sand here is relatively coarse grained and the most abundant minerals include biotite, magnetite and zircon (Alvarado and Figueroa, 1989). The Colola beach morphology is characterized by a steep slope (Figure 1). Although the beach morphology is highly dynamic and its characteristics change seasonally, we summarize here the general characteristics of this beach. The lower and seaward sector of the beach, the beach face, is steep and shows variable slope, ranging from 10° to 30°; it remains wet because of the influence of waves depending on the month of the year, when wave conditions, wind direction and intensity change. Landwards and up-profile, the backshore, shows a berm, characterized by a gentle slope, and marks the boundary between beach face and the beach mid-platform. The beach mid platform is flat and is the most extensive area barren of vegetation. Above the mid platform, there is an area with gentle slope and patches of vegetation (*Distichlis spicata* and *Ipomoea pes-caprae*) (Perez, 2008). The higher area of the beach is the upper beach limiting with the vegetation. The predominant vegetation is low deciduous forest, medium semi-evergreen forest, mangrove, bushy scrub of coastal dunes, and palms (Alvarado and Huacuz, 1996). Climate is warm humid with storms and strong

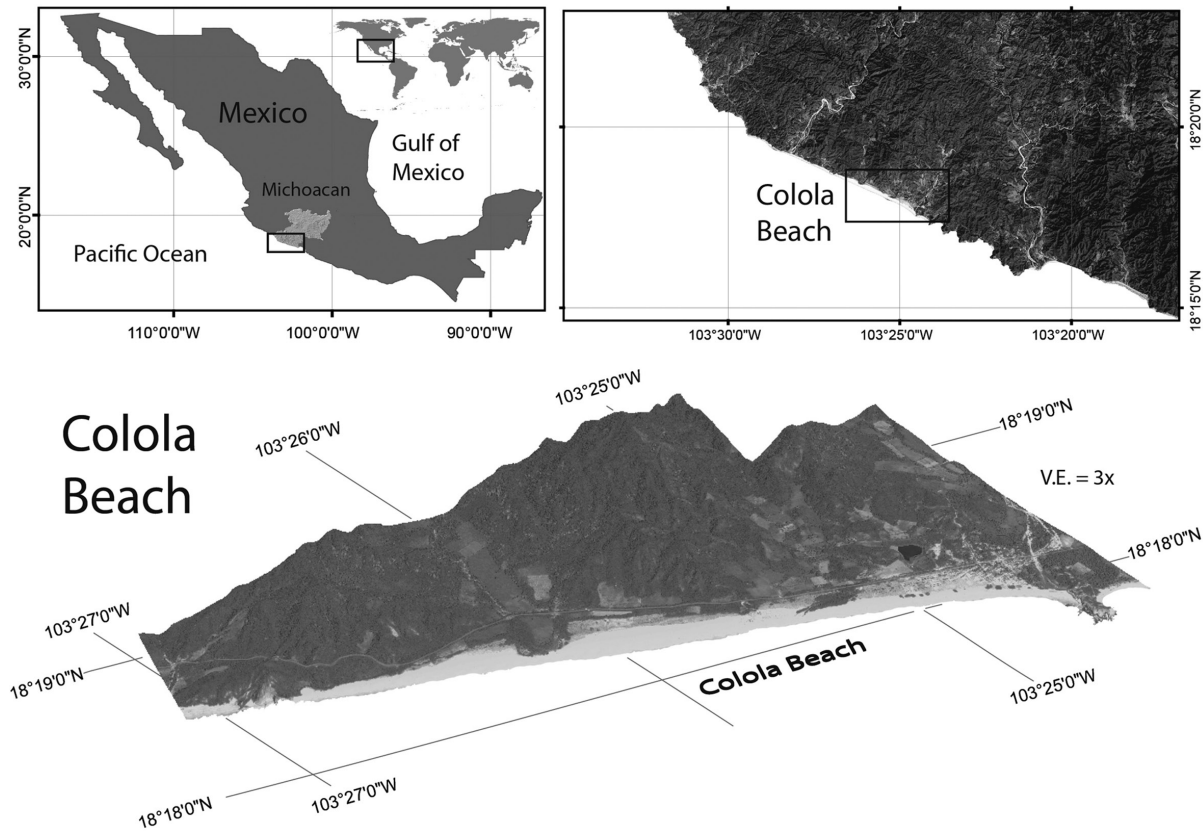


**Figure 1.** Location of Colola Beach, Michoacán, Mexico.

winds and rainfall during July-October, and a prolonged dry period from November to July (Alvarado and Huacuz, 1996). Major hurricane and tropical storm activity prevails during June to November in the Eastern North Pacific (NHC, 2013). The black sea-turtle breeding season coincides from August to March, with the hurricane and tropical storm activity, which suggests that morphologic changes along-beach and on the beach profile occur seasonally. Two zones are favored for turtle nesting: the middle zone of the beach profile, around 100 m from the beach tide front, and alongshore on the western and central sectors of Colola beach (Fuentes *et al.*, 2010).

## Methods

### *Digital elevation model*

The elevation of the terrain was determined by surveying the topography of Colola Beach with a SOKKIA total station SET 630RK. Data were recorded with vertical and horizontal accuracy of 3 mm from equidistant points at >11 m and

maxima of <40 m distance, and random points with known elevations (Weibel and Heller, 1991). The coastline was plotted by visual interpretation from a Google Earth satellite image for October 31, 2005 (Google Earth, 2011).

### *Interpolation*

The collected three-dimensional coordinates were imported in the ArcGIS environment (ArcGIS, 2013) and plotted to a ground control points shape file. The ground control points were used as sample points to generate a 20 cm pixel size digital elevation model (DEM). The DEM was generated by the interpolation method known as inverse distance weighting (IDW) using the Topo to Raster tool in ArcGIS. This is a local deterministic interpolation technique that has been found to be good for interpolation of geomorphologically smooth areas and is as accurate as other interpolation techniques (Aguilar *et al.*, 2005; Arun, 2013). This interpolator assumes that each point in the data set has a local influence that decreases with distance, and hence the values of the

points near the node that is processed have more importance or weight in the estimation of the value that will be assigned to it, than have the points that are further away (Burrough and Mcdonnell, 1998). Normally, the search is made considering a number of points or a radius (in a circle around the cell under consideration).

Once the digital elevation model had been obtained, we simulated possible sea inundation of Colola Beach under three different scenarios of sea-level rise (0.50 m, 1.40 m and 5.0 m) based on present predictions of 0.5 m within the next 50 years and of 1.40 m in 100 years (Vermeer and Rahmstorf, 2009). The 5.0 m sea level rise is a hypothetical scenario with no precise date of when it might happen.

#### *Position of individual nesting sites*

The black sea-turtles nest mainly in the mid platform of the beach, which is a warm area far from the high tide mark and free of vegetation (Pérez, 2008). To plot the spatial distribution of the turtle nests, we sampled 300 nests with a portable global positioning system (GPS Garmin) along the length of the beach and across its width. The positioning of these points was superimposed on the inundation models to determine the probable impact of sea-level rise under the different scenarios proposed. Topographic profiles across the Colola Beach and the beach areas lost due to possible inundation scenarios were measured using the DTM.

## **Results**

The DEM, topographic profiles, and plot of nesting sites in the Colola Beach show that most of the nesting sites are located in the mid- and high-beach. The beach slope although variable alongshore, tends to be steep ( $10^{\circ}$  to  $30^{\circ}$ ) in the beach front facing the sea (Figure 2). The effects of different sea-level rise scenarios and inundation of the beach are illustrated on six crossed beach profiles traced from west to east on Colola beach (Figure 2). It is evident that

the effect of a 0.5 m sea level rise is apparently smaller along shore. While a sea level rise of 1.4 m would affect mostly the foreshore along the Colola beach. Instead, a sea level rise scenario of 5 m would have a significant flooding effect in the beachfront and mid-platform of most of Colola beach, with more dramatic effect on the westernmost and easternmost sectors of this beach (Figure 2).

The simulations of beach inundation in Colola suggest that a rise of 0.50 m in sea level, predicted to occur within 50 years (Vermeer and Rahmstorf, 2009), would affected the beachfront and produce 2 % of area lost (Table 1). Although variable, the steep beach profile ( $10^{\circ}$  to  $30^{\circ}$ ) in the lower and seaward sector of the beach, the beach face, prevents from a larger damage and loss of the sea-turtle nesting area (Figure 3).

Modeling of a rise in sea level of 1.40 m, predicted for the next 100 years, suggests a significant loss of beach area (9%). Since the black sea-turtle tends to nest in the mid- and high-beach, the steep slope of the beachfront aids in preventing a major loss of nesting area (Figure 4, Table 1).

The model of beach inundation by sea-level rise of 5 m shows a considerable loss of beach, sparing only isolated patches. Two rivers reach the sea at Colola Beach, and the rising seawater would encroach on their channels and thereby leave the turtles with practically half of the current nesting area (Figure 2 and 5). The projected loss of beach area is about 54% (Table 1). Although in this scenario some nesting individual sites would not be affected, the main nesting area, in the mid platform of the beach, would be completely lost (Figure 6). Since Colola is a wide beach (150 m average width), only those areas landwards and near the vegetation would be the least affected, but high tides and the proximity of the coastline would result in deleterious effects in these areas also (Figure 5).

**Table 1.** Predicted loss of nesting area with different rise in sea level scenarios.

<b>Sea-level rise scenarios (m)</b>		<b>0.50</b>	<b>1.40</b>	<b>5.0</b>
<b>Predicted loss of beach area</b>	Area (ha)	1.24	5.01	31.95
	Percentage (%)	2	9	54

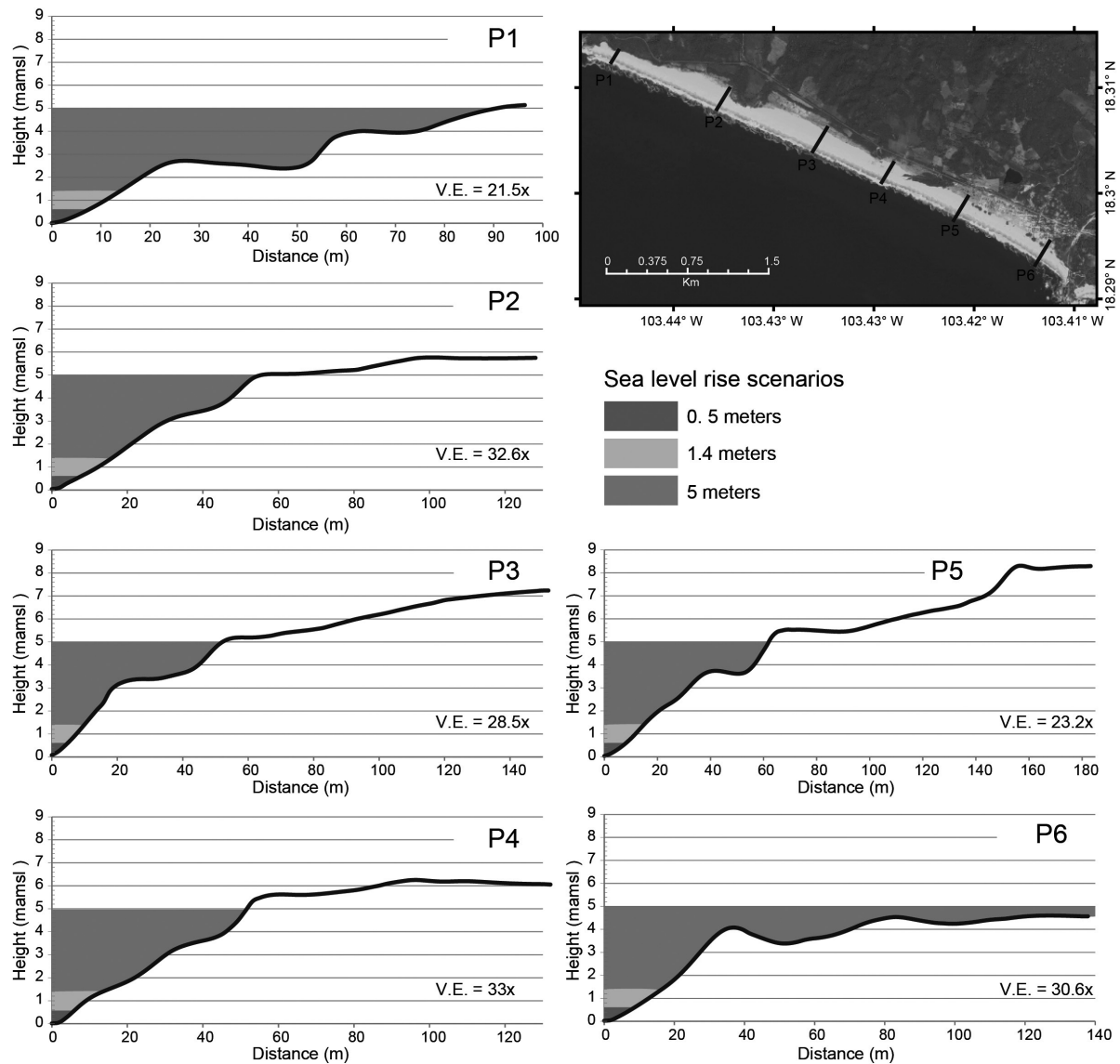


**Figure 2.** Topographic profiles of Colola Beach. Symbols: mamsl - meters above mean sea level; V.E. - vertical exaggeration.

## Discussion and Conclusions

### *Tectonic uplift vs. sea level rise*

The Michoacán coast is located in a tectonically active margin. This coast is subject to tectonic uplift (Ramírez-Herrera and Urrutia-Fucugauchi, 1999, Ramírez-Herrera *et al.*, 2011). The estimated rate of coastal uplift, based on marine terrace ages, for the neighbor areas in Michoacan-Guerrero coast is ca. 6.6 +/- 2 m/ka (Ramírez-Herrera *et al.*, 2011). We extrapolated this uplift rate to compare with our modeled sea level flooding scenarios at the Colola beach. The

scenario for next 100-year indicates a 1.4 m sea level rise, with an estimated uplift rate of 0.6 +/- 2 m, i.e. a value considerably lower than the projected sea level rise. In this scenario, even when considering tectonic uplift of this coast, the beach areas where turtles nest are foreseen to be inundated by sea level rise. In the second scenario, in 50 years, 0.5 m sea level rise compared with estimated uplift rates of 0.3 +/- 2 m/50 yr, again the sea level rise value is still higher than tectonic uplift. Thus, even in this tectonically active coast, sea level rise scenarios suggest inundation of beach areas where sea-turtles nest.

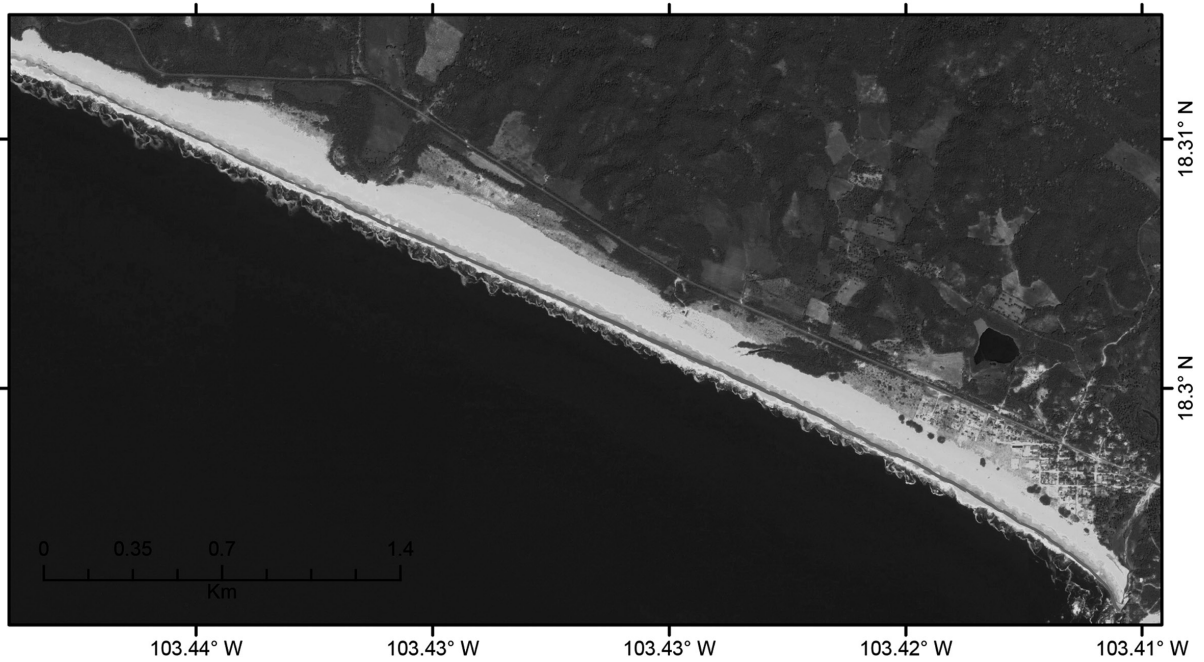


**Figure 3.** Model shows a sea-level rise scenario of 0.50 m at Colola Beach, Michoacán, Mexico, as predicted within 50 years. Inundated areas are shown in red color.

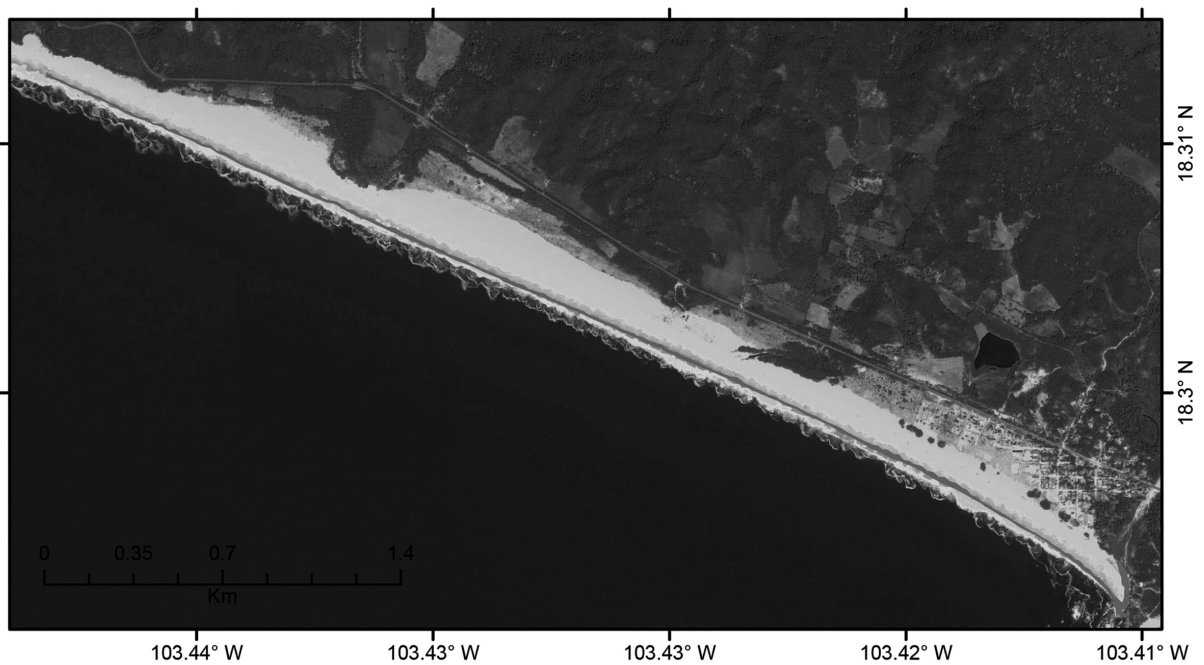


**Figure 4.** Model shows a sea-level rise scenario of 1.40 m at Colola Beach, Michoacán, Mexico, as predicted within 100 years. Inundated areas are shown in red color.

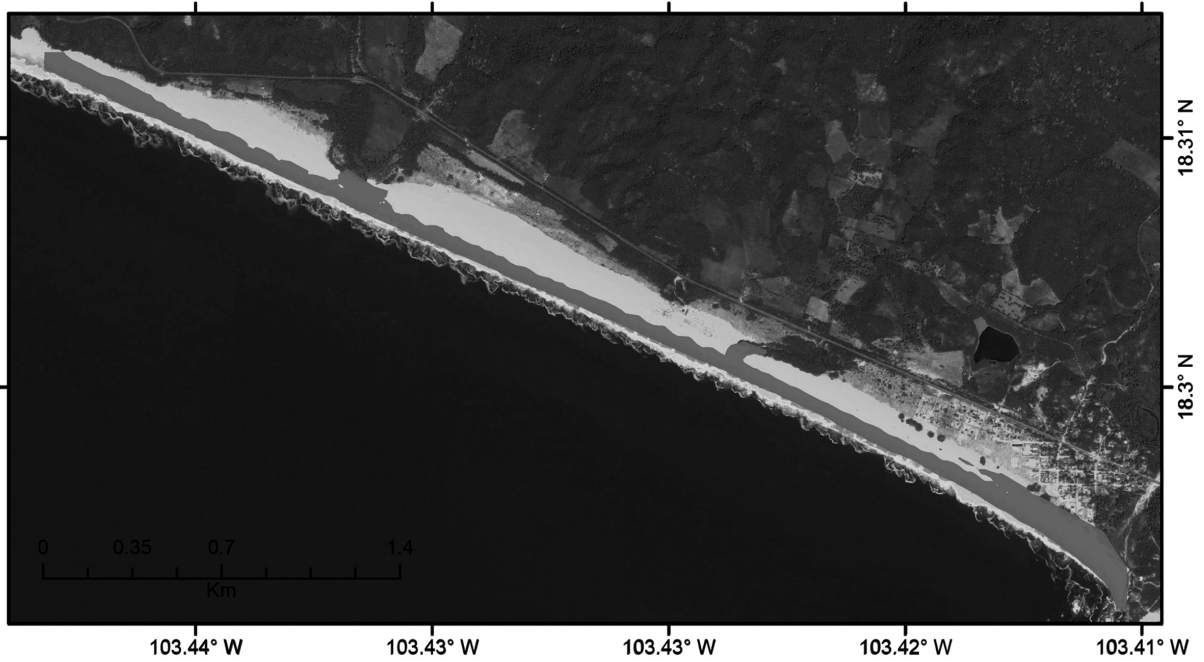


**Figure 5.** Model shows a sea-level rise scenario of 5 m at Colola Beach, Michoacán, Mexico. Inundated areas are shown in red color.

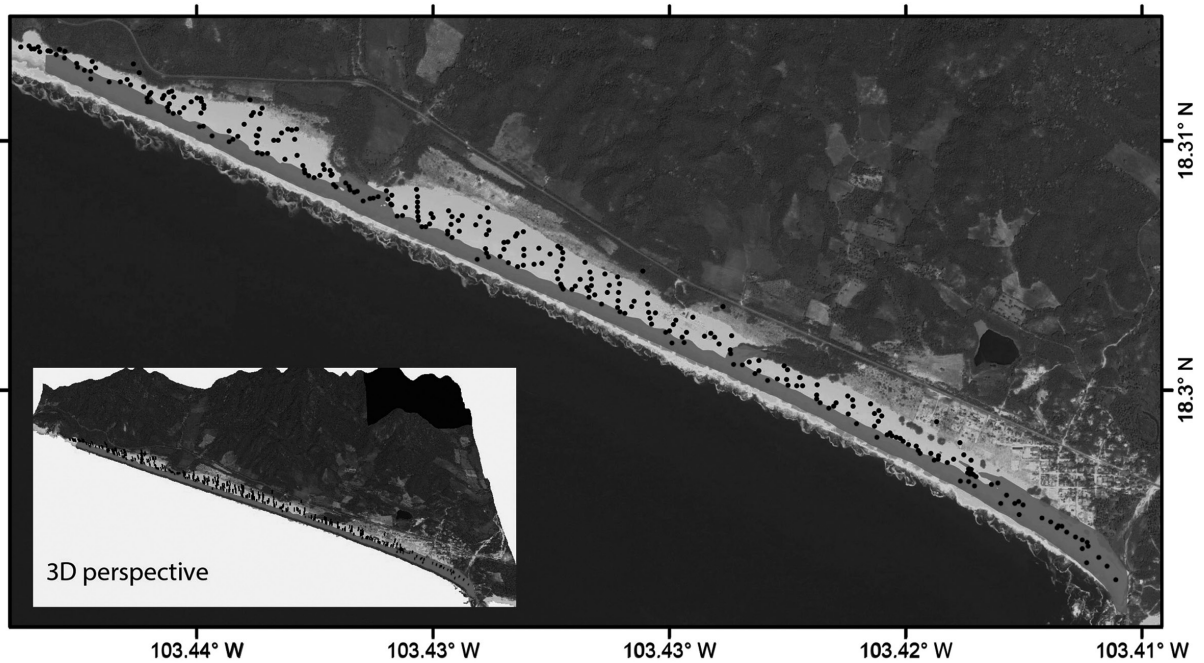


**Figure 6.** Model of Colola Beach showing a 5 m rise in sea level (inundated areas shown in red) and the positions of turtle nests (black dots). Insert shows 3D perspective.

### Sea-level rise modeling

Models that simulate sea-level rises in nesting areas of marine turtles are of great importance in establishing mitigation procedures for the conservation of these species. Our models indicate that an increase in sea level by 0.50 m or 1.40 m would affect the Colola Beach, reducing significantly the beach in 2% and 9% of area loss. Sea turtles prefer to nest in the warm middle platform of the beach; due to the steep profile of the Colola beach the nesting area is apparently affected in a lower extent. Mortimer (1982) and Pereira (2002) consider the selection of nesting area to arise from the biology of the species and the patterns of behavior that have evolved from this. At Colola the selection may also be attributable to a preference for areas that are free from vegetation and that have humidity that favors nest construction. Extreme humidity or dryness in the sand can lead to a collapse of the nest during construction with failure of the nesting operation. Turtles avoid sites low on the beach because of the high humidity and salinity that impede nest building, and also because of inundation produced by tides.

While the impacts of sea level rise scenarios under 0.50 and 1.40 m appear to be less significant in relation to the loss of nesting Colola area, Fuentes *et al.* (2010) mentions that the salt intrusion into the water table in beaches can be a significant factor, product of the increment of the average sea level. Saline intrusion into the water table at the beach can be a significant threat then to the black turtle because the females lay their nests at a depth of between 0.70 and 1.0 m deep, which can be reached by the water table under storms and high waves conditions. Moreover, the Bruun Rule (Bruun, 1988) predicts that by the year 2100 the shoreline would be horizontally retracted 50 to 100-fold relative to the vertical sea level rise, then the regression of the beaches, such as in Australia can mean between 4.5 to 88 m (CSIRO, 2002). Consequently, climate change may accelerate the current global trend of beaches receding. This may to some extent affect beach ecosystems if the retraction of the beaches is just the only change, however, if this is accompanied by changes in habitat (such as dunes, grain size, area of beach and slope) or loss of habitat (narrowing of beaches), great ecological changes may occur in a particular beach (Jones, 2012). These would have dire consequences for the turtle population. For instance, neighbor beaches to the Colola beach Reserve, that are habitats to other species of marine turtles, though might suffer a more

dramatic effect due to their low slope (e.g. La Llorona beach).

Remarkably, the simulation of a 5 m rise in sea level suggests a significant loss of beach area (54%). With the rise in sea level, the sea water would probably flow up the river channels, since these are lower than the surrounding sand; this scenario would leave only patches of beach above water level and consequently sea turtles would be left with virtually no nesting areas. Moreover, beach erosion, a concomitant effect of sea-level rise, is a potential threat that might increase the loss of beach and consequently the nesting habitat for the black sea-turtle.

Another consideration is that the differential distribution of nesting females on a beach may reflect the strong philopatry of marine turtles; if a larger number of offspring are produced in a certain site on the beach, it is probable that in those sites the high percentages of survival of the nesting females and of the young that are produced there determine future differential selection of nesting sites. If nesting sites do not have the characteristics necessary for success, this may result in a reduction of the population size.

At the global level, a rise in sea level has the potential to endanger the availability of nesting beaches in low beaches, island beaches (Nicholls, 1998; Fish *et al.*, 2005; Baker *et al.*, 2006; Jones *et al.*, 2007; Mazaris *et al.*, 2009). A sea level rise of 0.9 m could flood up to 40% of the nesting beaches of the green turtle (*Chelonia mydas*) on the north-eastern island of Hawaii (Baker *et al.*, 2006), and 50% of those of the hawksbill turtle (*Eretmochelysimbricata*) in Barbados (Fish *et al.*, 2008) and 51% in Bonaire (Fish *et al.*, 2008). On Colola Beach a rise of 5 m could flood 25% of the nesting area. Other nesting areas must also be studied, in view of the migratory nature of marine turtles.

Different models of possible rises in sea level and concomitant sea inundation of the beach must be considered to manage adequately turtle nesting areas. Owing to the physical characteristics of Colola Beach, the nesting areas are likely to be affected within the next 100 years by sea-level rise. Even more, a rise of 5 m would reduce the beach to isolated patches and leave the turtles virtually with few nesting areas, depending on the ability of the beach to recede as sea level rises. Strategies of adaptation to climate change may allow the preservation of nesting areas of the marine turtle population.

## Acknowledgements

We thank J. A. Navarrete-Pacheco and A. D. Flores Domínguez for help with GIS, and A. Grant for English editing. We thank three anonymous reviewers and the editor Professor Cinna Lomnitz for a thorough review and valuable comments that help improving this manuscript. Ramírez-Herrera acknowledges CONACYT-SEP grant No. SEP-CONACYT-129456.

## References

- Aguilar F.J., Agüera Güera M.A., Aguilar Carvajal F., 2005, Effects of terrain morphology, sampling density, and interpolation methods on grid DEM accuracy. *Photogrammetric Engineering & Remote Sensing*, 71, 805–816.
- ArcGIS 2013, Online data available at: <http://www.arcgis.com/home/> (accessed 30.01.14).
- Alvarado J., Figueroa A., 1989, Ecología y Conservación de las Tortugas Marinas en Michoacán, México (segunda parte), Cuadernos de Investigación, U.M.S.N.H, 5, 68 pp.
- Alvarado J., Huacuz D., 1996, Guía ilustrada de los anfibios y reptiles más comunes de la reserva Colola-Maruaata en la costa de Michoacán, México. U.M.S.N.H. Facultad de Biología. Morelia, Michoacán, 90 pp.
- Arun P.V., 2013, A comparative analysis of different DEM interpolation methods. *The Egyptian Journal of Remote Sensing and Space Sciences*, 6, p. 133–139.
- Baker J.D., Littnan C.L., Johnston D.W., 2006, Potential effects of sea level rise on the terrestrial habitats of endangered and endemic megafauna in the Northwestern Hawaiian Islands. *Endangere Species Research*, 2, p. 21–30.
- Bird E.C., 1996, Beach management, John Wiley & Sons, Ltd. Chichester, 281pp.
- Bjorndal A.K., Bolten B.A., 1992, Spatial Distribution of Green turtle (*Chelonia mydas*) Nest at tortuguero, Costa Rica. *Copeia*. 1, p. 45-53.
- Burrough P.A., McDonnell R.A., 1998, Principles of Geographical Information Systems. Oxford University Press, New York. p. 333–335.
- Brunn P., 1988, The Brunn Rule of erosion by sea level rise? A discussion of large-scale two and three-dimension usages. *Journal Coastal Research*, 4, p. 627-648.
- Church J., Gregory J.M., Huybrechts P., Kuhn M., Lambeck K., Nhuan M.T., Qin D., Woodworth P.L., 2001, Changes in sea level. In: Houghton, J.T., Ding Y, Griggs D.J., Noguer M., Vander Linden P.J., Dai X., Maskell K., Johnson C.A., (Eds.), *Climate change 2001. The scientific basis. Contribution of Working Group I to the Third Assessment Report of the Intergovernmental Panel on Climate Change*. Cambridge University Press, Cambridge, p. 639–694.
- Commonwealth Scientific and Industrial Research Organisation (CSIRO), 2002, *Climate Change and Australia's Coastal Communities*. [www.dar.csiro.au/publications/coastalbroch](http://www.dar.csiro.au/publications/coastalbroch).
- Davenport J., 1989, Sea turtles and the greenhouse effect. *British Herpetological Society Bulletin*, 29, p. 11–15.
- Delgado C., Alvarado J., 2005, Tortugas marinas de Michoacán. *Historia Natural y Conservación, México*, 152 pp.
- Drews C., Fonseca A., 2009, Aumento del nivel del mar por cambio climático en Playa Grande, Parque Nacional Las Baulas, Costa Rica. Simulación de inundación basada en un modelo de elevación digital de alta resolución e implicaciones para el manejo del parque. Informe técnico, WWF / Stereocarto, San José, Costa Rica, 20 pp.
- Fish M.R., Cote I.M., Gill J.A., Jones A.P., Renshoff S., Watkinson A.R., 2005, Predicting the impact of sea-level rise on Caribbean sea turtle nesting habitat. *Conservation Biology*, 19, p. 482–491.
- Fish M.R., Cote I.M., Horrocks J.A., Mulligan, B., Watkinson A.R., Jones A.P., 2008, Construction setback regulations and sea level rise: mitigating sea turtle nesting beach loss. *Ocean & Coast Management*, 51, p. 330–341.
- Fish M.R., Drews C., 2009, Adaptación al cambio climático: opciones para las tortugas marinas. Informe de WWF, San José, Costa Rica. 20 pp.

- Fuentes M, Limpus C.J., Hamann M., Dawson J., 2010, Potential impacts of projected sea-level rise on sea turtle rookeries. *Aquatic Conservation-Marine and Freshwater Ecosystems*, 20, p. 132-139.
- Google Earth, 2011, "Playa Colola". 18 18' 01-19" N and 103 25' 32.25" W. Google Earth. 31 October 2005. (Retrieved 21 December 2011).
- Grinsted A., Moore J.C., Jevrejeva S., 2009, Reconstructing sea level from paleo and projected temperatures 200 to 2100AD. *Climate, Dynamics*. <http://dx.doi.org/10.1007/s00382-008-0507-2>. 461-472.
- Hoffman J.S., Keyes D., Titus J.G., 1983, Projecting Future Sea Level Rise; Methodology, Estimates to the Year 2100, and Research Needs, Environmental Protection Agency, Washington. p. 115-121.
- Intergovernmental Panel on Climate Change (IPCC) 2002, Cambio Climático y biodiversidad. Documento técnico del Grupo Intergubernamental de Expertos sobre el Cambio Climático, Ginebra, Suiza, 84 pp.
- Intergovernmental Panel on Climate Change (IPCC), 2007, Cambio climático. Informe de síntesis. Contribución de los Grupos de trabajo I, II y III al Cuarto Informe de evaluación del Grupo Intergubernamental de Expertos sobre el Cambio Climático, Ginebra, Suiza, 104 pp.
- Jones A.R., Gladstone W., Hacking N.J., 2007, Australian sandy beach ecosystems and climate change: ecology and management. *Australian Zoologist*, 34, p. 190-202.
- Jones A.R., 2012, Higher-level Ecological Relationships to Climate Change. In Ecological Consequences of Climate Changes. Erick a. Beever and Jerrold L. Belant editors. CRC press 2012.
- Lara L.R., 2008, Los cambios ambientales globales y la vulnerabilidad de los sectores de México. En: Azuz Adeath I.A. (Eds.), Infra estructura y Desarrollo Sustentable. Gobierno del Estado de B.C. CETYS Universidad, 15 pp.
- Lutcavage M.E., Plotkin P., Witherington B., Lutz P.L., 1997, Human impacts on sea turtle survival. In: Lutz, P.L., Musick, J.A. (Eds.), *The Biology of Sea Turtles*. CRC Press, Boca Raton, Florida, p. 387-409.
- Mazaris A.D., Mastinos G., Pantis J.D., 2009, Evaluating the impacts of coastal squeeze on sea turtle nesting. *Ocean and Coast Management*, 52, p. 139-145.
- Miller J.D., 1997, Reproduction in sea turtles. In: Lutz PL, Musick JA (Eds.) *The biology of sea turtles*. CRC Press, Boca Raton, Florida, 1, p. 51-81.
- Mortimer J.A., 1982, Factors influencing beach selection by nesting sea turtle. K.A. Bjorndal (Eds.), Smithsonian Institution. Press, Washington, D.C. p. 45-52.
- Mrosovsky N., Dutton P.H., Whitmore C.P., 1984, Sex ratios of two species of sea turtle nesting in Suriname. *Canadian Journal of Zoology*, 67, p. 2227-2239.
- National Hurricane Center (NHC), Hurricane Research Division; Central Pacific Hurricane Center. The Northeast and North Central Pacific hurricane database 1949-2012. United States National Oceanic and Atmospheric Administration's National Weather Service. (Retrieved August 21, 2013).
- Nicholls R.J., 1998, Coastal vulnerability assessment for sea level rise: evaluation and selection of methodologies for implementation. Technical Report R098002, Caribbean Planning for Adaption to Global Climate Change, 44 pp.
- Norma Oficial Mexicana NOM-059-ECOL-2001, 2002, Protección ambiental-especies nativas de México de flora y fauna silvestres-Categorías de riesgo y especificaciones para su inclusión, exclusión o cambio-Lista de especies en riesgo. Miércoles 6 de marzo de 2012, DIARIO OFICIAL, Segunda Sección, 153 pp.
- Pereira Y., 2002, Proceso de anidamiento de *Chelonia mydas* en Cayo Real, Archipiélago de los Canarreos, Cuba. Universidad de la Habana, Centro de Investigaciones Marinas, Trabajo de diplomado, 48 pp.
- Perez C.A., 2008, Éxito de anidación de tortuga negra (*Chelonia agassizii*, Bocourt 1868) en la playa de Colola, Michoacán, México. Tesis de licenciatura. UMSNH. Morelia, México. 42 pp.
- Pritchard P.C.H., 1997, Evolution, Phylogeny and Current Status, in: *The biology of sea turtles*. CRC Marine Sciences Serie, CRC Press, Inc, p.1-28.

Ramírez-Herrera M.T., Urrutia-Fucugauchi J., 1999, Morphotectonic zones along the coast of the Pacific continental margin, southern Mexico. *Geomorphology*, 28, 237–250.

Ramírez-Herrera M.T., Kostoglodov V., Urrutia-Fucugauchi J., 2011, Overview of Recent Coastal Tectonic Deformation in the Mexican Subduction Zone, *Pure and Applied Geophysics*, DOI 10.1007/s00024-010-0205-y.

Vermeer M., Rahmstorf S., 2009, Global sea level linked to global temperature. *Proceedings of the National Academy of Science of the United States*, 51, p. 21527–21532.

Watson J.W., Epperly S.P., Shah A.K., Foster D.G., 2005, Fishing methods to reduce sea turtle mortality associated with pelagic longlines. *Canadian Journal of Fisheries and Aquatic Sciences*, 62, p. 965–981.

Weibel R., Heller M., 1991, Digital terrain modeling. In: Maguire, D.J. (In:) Godchild, M.F. y Rhind, D.W. (Eds.), *Geographical Information Systems*. Longman, Scientific & Technical, 1, p. 45-54.

World Conservation Union, 2001, Ruling of the IUCN red list standards and petitions subcommittee on petitions against the 1996 listings of four marine turtle Species. *Newsletter of the species survival commission*, 36, p. 31-34.

## Early warning from seismic ionospheric anomaly of the 24 May 2014, $M_w = 6.4$ Aegean-Sea earthquake: two-dimensional principal component analysis (2DPCA)

Jyh-Woei Lin

Received: June 06, 2014; accepted: August 27, 2014; published on line: March 31, 2015

### Resumen

Se utilizó el análisis de componentes principales de dos dimensiones (2DPCA) para determinar el contenido total de electrones de la ionosfera (TEC), una anomalía de dos dimensiones después del terremoto Egeo-Sea en 09:25:03 (UT) el 24 de mayo del 2014 ( $M_w = 6.4$ ). Posterior al terremoto la anomalía TEC fue la más intensa y se localizó en 9:30-09:35 (UT). Ésta es una razón potencial para la formación de la anomalía TEC, lo que podría ser una fluctuación fuera de lo normal. Por ejemplo, la variación de la densidad de los electrones se elevó a alta velocidad de la onda de choque acústico con la velocidad de al menos 1.818,18 km/h.m/s, dada por el movimiento principal del terremoto. El tiempo de duración de la anomalía TEC era de al menos cinco minutos. El tsunami fue causado por un terremoto con epicentro en el mar, la fluctuación anómala podría ser un signo precoz para las regiones lejanas del epicentro cuando comenzó a propagarse, ya que el tsunami llegó a ellas más lentamente que las fluctuaciones anómalas.

Palabras clave: análisis de componentes principales de dos dimensiones (2DPCA), contenido total de electrones bidimensional (TEC), Aegean-Sea terremoto, ondas de choque acústicas.

### Abstract

Two-dimensional principal component analysis (2DPCA) has been used to determine ionospheric two-dimensional total electron content (TEC) anomaly after Aegean-Sea earthquake at 09:25:03(UT) on 24 May, 2014 ( $M_w = 6.4$ ). The TEC anomaly was more intense localized at 09:30 to 9:35 (UT) post the earthquake. Potential reason of the TEC anomaly, which might be a anomalous fluctuation e.g., electron density variation, is rising high speed acoustic shock wave with the speed of at least 1818.18 Km/h. m/s resulted by the mainshock of the earthquake. The duration time of the TEC anomaly was at least 5 minutes. The anomalous fluctuation could be an early warning for the regions far from the epicenter when it began to propagate because the tsunami arrived at the far regions very slower than anomalous fluctuation if the tsunami was caused by earthquake with epicenter in the sea.

Key words: Two-dimensional principal component analysis (2DPCA), two-dimensional total electron content (TEC), Aegean-Sea earthquake, acoustic shock waves.

---

J. W. Lin  
Dept. of Earth Science  
National Cheng Kung University  
No.1 University Road  
Tainan City, Taiwan  
Corresponding author: [pgjwl1966@gmail.com](mailto:pgjwl1966@gmail.com)

## Introduction

Ionospheric total electron content (TEC) anomalies associated with large earthquakes have been widely researched both as precursors and aftereffects (Artru & Lognonné, 2001; Garcia *et al.*, 2005; Hegai *et al.*, 2006; Liu *et al.*, 2009; Liu *et al.*, 2006; Lognonné *et al.*, 2006; Marchand *et al.*, 2008; Pulinets *et al.*, 2000; Pulinets & Boyarchuk, 2004; Pulinets, 2007; Singh, *et al.*, 2010; Zhao *et al.*, 2008). The exact causes of earthquake associated precursor TEC anomalies are not known; however, there are many possibilities including gravity waves generated by the solid-earth and sea, as well as lower atmospheric electric fields resulting from earthquake preparation processes that can be transferred into the ionosphere along geomagnetic lines (Pulinets, 2004). Regardless of the specific causes of earthquake-precursor TEC anomalies, their earthquake association has been established statistically using deviations from running TEC median values after eliminating other possible causes of TEC disturbance such as solar flare and geomagnetic storm activity (Lin, 2010). The TEC anomalies were most likely caused by acoustic gravity waves traveling from the earth's surface into the ionosphere (Artru *et al.*, 2001; Garcia *et al.*, 2005; Lognonné *et al.*, 2006; Marchand *et al.*, 2008; Pulinets *et al.*, 2000). The mechanism for this is thought to be earth's atmosphere acting as a natural amplifier. During an earthquake tiny amounts of kinetic energy are transferred from the solid earth to the lower atmosphere. If this kinetic energy is conserved, then given the exponential decline in atmospheric density with height, waves of great amplitude can result in the ionosphere. It has been estimated that millimeter disturbances at the earth's surface can be amplified to waves of amplitude 100 m at 100 km altitude (Artru, *et al.*, 2001; Lognonné *et al.*, 2006). A study by Lognonné *et al.* (2006) using ground based GPS receivers to detect post-seismic ionospheric disturbance found that the measurable impact of the gravity waves resulting from the Nov. 3. Denali, Alaska  $M=7.9$  earthquake produced small but detectable changes in the TECu count of 0.1% peak to peak. This disturbance was detected by 6 other satellites. Lognonné *et al.* (2006) also measured the effects of near field seismic waves for the Hokkaido Tokacho – Oki earthquake of Sept. 25, 2003. In that experiment, they found that acoustic waves could be detected as high as 800 km, they also measured the gravity wave impact for the same earthquake and got similar results to those for the Alaskan Denlai earthquake in terms of TECu disturbance. One issue, however, with all TEC

measurement is the nature of the ionosphere. The electron content of the ionosphere is highly dynamic plasma so that establishing anomalies and event association is not easy. For example, determining a running median of TEC content before large earthquakes to search for precursor TEC anomalies is difficult and may not always be reliable because TEC can be affected by many factors. Pulinets (2004) makes an extensive list of possible causes, including radon gas release, causing lower atmospheric electric fields which travel up into the ionosphere along geomagnetic lines. Freund (2003) suggests P-type semiconductor effect as the cause of lower atmosphere electric fields. Recent studies have shown that earthquake-related TEC anomalies are detectable using principal component analysis (PCA) (Lin, 2010, 2011). PCA is an alternative pure mathematical method for the measuring TEC anomalies. The method relies on exploiting signal delay between global positioning system (GPS) satellites and ground receiver stations without direct observation of ionospheric TEC. The long term period variance of ionospheric TEC (Lin, 2010) does not affect the outcome of the results using PCA and the potential influence of other factors such as solar flares and geomagnetic disturbance are eliminated using relevant Kp indexes statistically. While these PCA experiments were able to detect and even describe the spatial pattern or physical shape of earthquake-related TEC anomaly (Lin 2011), PCA might not be as useful as two-dimensional principal component analysis (2DPCA) in the detection of TEC anomalies when applying to two-dimensional TEC data. Therefore, the goal of this study is to examine the ionospheric TEC anomaly related to Aegean-Sea earthquake (40.313°N, 25.453°E) at 09:25:03UT on 24 May, 2014 ( $M_w = 6.4$ ) with the depth of 10.0km (U.S. Geological Survey) using 2DPCA. Possible causes of discovered anomaly will be discussed. It is expected that at the time 09:25 to 09:35 UT, ionospheric TEC behavior should be complicated showing large earthquake-related anomaly shortly after or during the mainshock like the results of Liu *et al.*'s work (2011) while tsunami did not occur to affect the ionosphere. The TEC data (two dimensional TEC data, **F-layer**) are derived NASA Global Differential GPS system (GDGPS) and global TEC maps (GIMs) in this study are derived using TEC data from ~100 real-time GDGPS tracking sites, augmented with additional sites that are available on 5 minutes basis. The integrated electron density data along each receiver-GPS satellite link is processed through a Kalman filter. Processing to estimate TEC value needs to consider some biases (influences) during restore of TEC

values from measurements of dual-frequency delays of GPS signals, which related with cycle slips, resolving of carrier phase ambiguity, determination hardware delays for phase, code measurements, tropospheric and multipath problems. The Kalman filter has been used to estimate the TEC with less bias (Kechine *et al.*, 2004; Ouyang *et al.*, 2008) (<http://www.gdgps.net/system-desc/index.html>).

## Method

### 2DPCA

For 2DPCA, let signals are represented by a matrix  $A$  (the dimension of  $n \times m$ ). Linear projection of the form is considered as followed (Sanguansat 2012),

$$y = Ax \quad (1)$$

Here  $x$  is an  $n$  dimensional project axis and  $y$  is the projected feature of signals on  $x$  called principal component vector.

$$S_x = E (y - Ey) (y - Ey)^T \quad (2)$$

Here  $S_x$  is the covariance matrix of the project feature vector.

The trace of  $S_x$  is defined;

$$J(x) = tr(S_x), \quad (3)$$

$$tr(S_x) = tr\{x^T G x\},$$

where  $G = E[(A - EA)^T (A - EA)] \quad (4)$

The matrix  $G$  is called signal covariance matrix. The vector  $x$  maximizing Eq. 4 corresponds to the largest (principal) eigenvalue of  $G$ , and let the largest eigenvalue be the most dominant component of the data, therefore largest eigenvalue is represented the principal characteristics of the data (Sanguansat 2012, Jeong *et al.*, 2009). 2DPCA can be removed small sample signal size (SSS) problem for two dimensional TEC data (Fukunnaga, 1991). The PCA converts the measurements into one-dimensional data before covariance matrix calculation (Yang *et al.*, 2004). The covariance matrix of PCA is based on an input matrix with the dimension of  $m \times n$ , which is reshaped from one-dimensional data (length of  $m$  multiplying  $n$ ). Reshaping data will cause computing error because PCA is a tool to deal with one-dimensional data. It means that the spatial structure and information can not be well preserved due to some original information loss when inverting to original dimension (Kramer, 1991) under the condition

of the matrix being small sample size (SSS). Such information loss is called SSS problem. However, the covariance matrix in 2DPCA is full rank for a matrix of low dimension. Therefore the curse of dimensionality and SSS problem (low dimensional data problem) can be avoided (Kong *et al.*, 2005; Sanguansat 2012). TEC data are examined to detect earthquake-related TEC anomaly and GIMs are only used to observe TEC situation in this study.

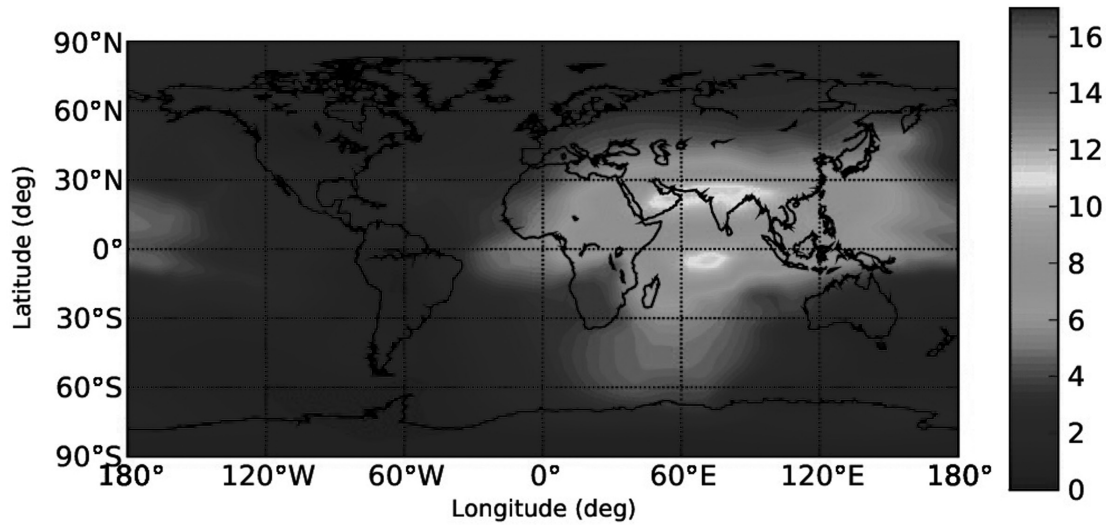
### TEC Data Processing 2DPCA

Figure 1(a) shows the GIMs during the time from 09:25 to 09:35. The earthquake-related TEC anomalies are not easy to observe using e.g. determining a running median of TEC content to detect a TEC anomaly (Liu *et al.*, 2006). The TEC data of the global region (not dividing the GIM for image processing) in Figure 1(a) are divided into 600 smaller areas 5 and 2.5 degrees in longitude and latitude, respectively. The size of each small area is  $12^\circ$  in longitude and  $9^\circ$  in latitude. The spatial resolution of the TEC data for GDGPS system is 5 and 2.5 degrees in longitude and latitude, respectively (Hernández-Pajares *et al.*, 2009; Chen and Gao 2005; Gao and Chen 2006) (<http://www.gdgps.net/system-desc/references.html>) and therefore 4 TEC data (two-dimensional data) are take in each area. The TEC were anomalies usually spread widely from the epicenters of large earthquakes from the results of Artru, *et al.* (2001) and Lognonné *et al.* (2006) and Hobara Parrot (2005). Therefore earthquake-related TEC anomaly is detectable for such selected size of an area. The 4 TEC data form a matrix  $A$  of Eq. 1 with the dimensions of  $2 \times 2$  as small sample signal size (SSS) in each are of Figure 1 (a). This allows for principal eigenvalues to be computed for each of the 600 smaller areas.

## Results

The respective results are given in Figure 1(b). The representative of large principal eigenvalues in the Figs 1(b) shows the existence of earthquake-related TEC anomaly represented by a large principal eigenvalue at the time 09:30-09:35. Non-earthquake TEC anomalies (e.g. EIA) are therefore suppressed by large principal eigenvalues defining as earthquake-related TEC anomaly. It means that if the largest principal eigenvalue related to the earthquake was taken out, then non-earthquake TEC anomalies would reveal clearly. Therefore the TEC anomaly related to this earthquake should be very large due to its large magnitude ( $M_w = 6.1$ ) and shallow depth (10.0km). The possibility of other factors such

24-May-2014 09:35:00 UTC



**Figure 1(a).** These figures show the GIMs during the time from 09:25 to 09:35 (UT) on 24 May 2014.

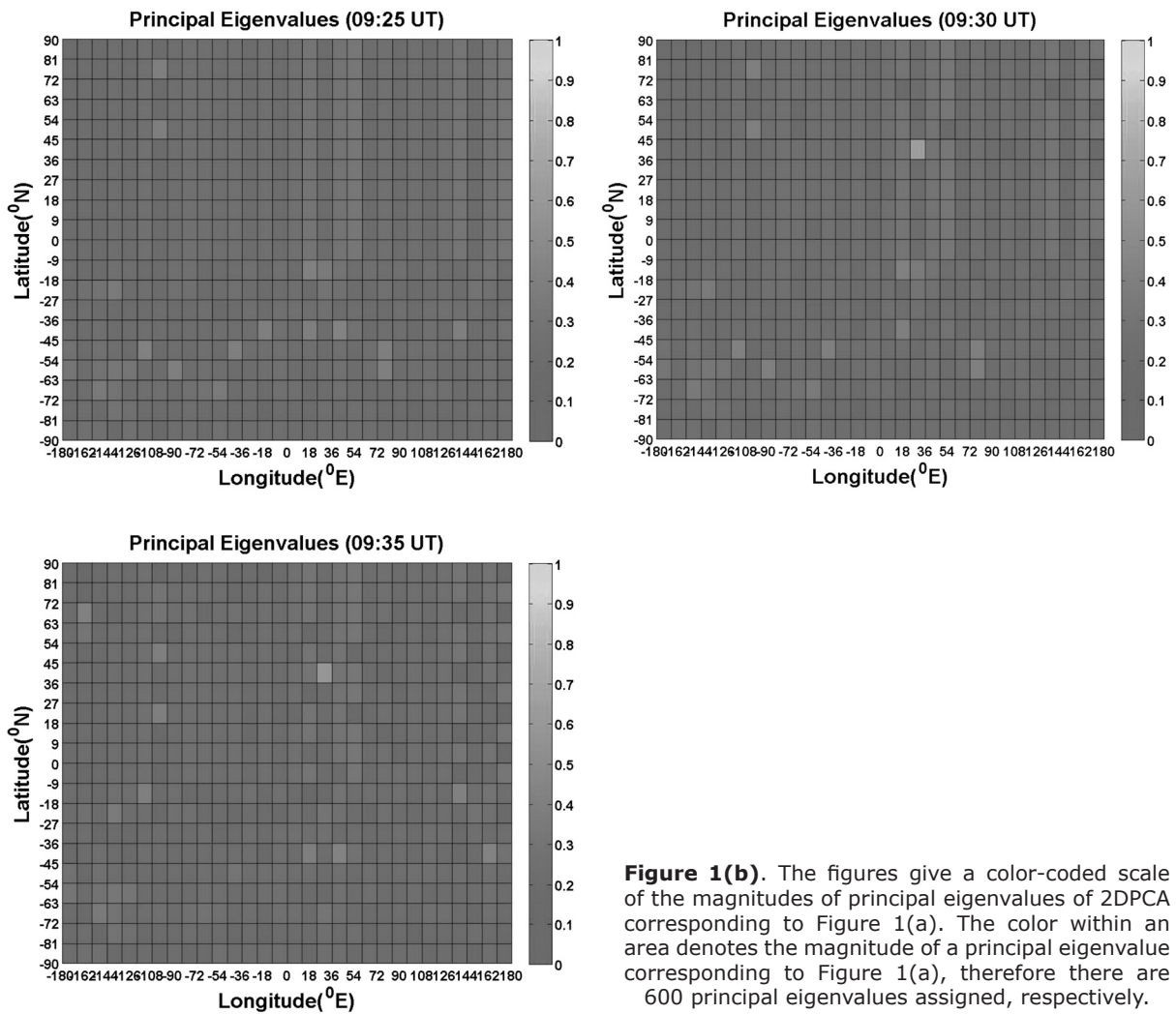


**Figure 1(b).** The figures give a color-coded scale of the magnitudes of principal eigenvalues of 2DPCA corresponding to Figure 1(a). The color within an area denotes the magnitude of a principal eigenvalue corresponding to Figure 1(a), therefore there are 600 principal eigenvalues assigned, respectively.

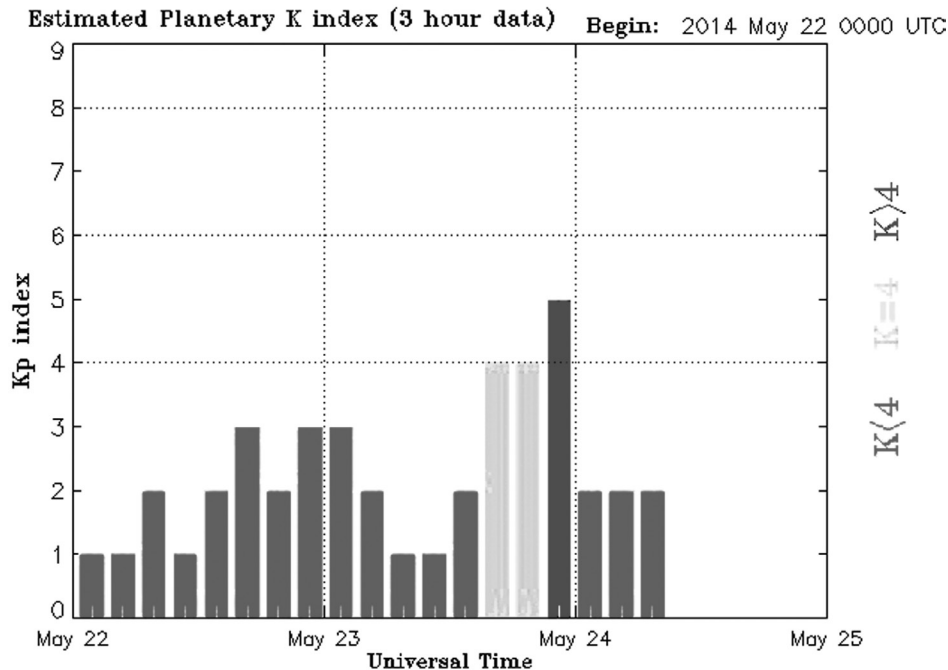


Figure 2. shows the Kp indices from 22 May to 24 May 2014.

as solar flare and geomagnetic effects affecting the results are considered by examining Kp indices (Elsner and Kavlakov, 2001; Hamilton *et al.*, 1986; Mukherjee, 1999). July, 2 was geomagnetic quiet day shown in Figure 3 ( $K_p < 4$ ).

### Discussion

2DPCA was able to detect a TEC anomaly related to this Earthquake at the time 09:30 to 09:35 UT. Identifying precise cause of earthquake related TEC anomalies is not easy. One reason for this is the number of potential causes of earthquake related TEC anomalies that arise during earthquake preparation, the mainshock, and aftershocks. For example during the earthquake preparation phase, Pulinets and Boyarchuk (2004) suggested that radon emanating from active faults and cracks before earthquakes ionize the near ground atmosphere to produce large vertical electric fields. Freund (2000) proposed that mobile positive holes in the earth's crust could be activated by low-energy impact, sound waves, and microfractures, creating charge clouds that could explain electromagnetic activity. Gravity waves arising from fine vibrations in the earth's surface leading to gas release are another possibility. This results in lower atmospheric turbulence and eventual ionospheric perturbations (Molchanov and Hayakawa, 1998). However, once an

earthquake occurred, then the most evident physical mechanism was ground motion and fine surface vibrations. Accordingly, studies of electromagnetic disturbance suggested two possible explanations for earthquake-related anomalies at this altitude. One was acoustic gravity waves caused by Joule heating (Hegai *et al.*, 1997) and the other was the presence of an electric field creating large scale ionospheric density irregularities (Liu *et al.*, 2004; Pulinets and Legen'ka, 2003) coupled with potential drift of the anomaly toward the equator. However, this anomaly resembled what one would expect from rising acoustic gravity waves because of strong motion. As discussed in the introduction earth's atmosphere could act as a natural amplifier due to declining atmospheric density with height. A large earthquake, such as this earthquake, was characterized by many fine vibrations at the earth's surface which could produce a vertical stark acoustic pressure wave of great amplitude by the time it reached the ionosphere. Such a description could possibly represent the stark and concentrated energy of an acoustic shockwave being formed in the lower atmosphere after the earthquake traveling up into the ionosphere (Jin *et al.*, 2010). This was the possibility described in the introduction to this study whereby high speed acoustic shock wave with the speed of at least 1818.18 Km/h. m/s caused by stark strong motion at the earth's surface are amplified through the atmosphere to

affect an anomalous fluctuation e.g., electron density variation in the ionosphere from the earthquake zone. The computing process of the shock wave speed was as follows; the time difference from original time of the earthquake to beginning time of TEC anomaly is 297 sec, and the F-layer is above 150 km, then  $150 \text{ km} \div 297 \text{ sec}$  is about 1818.18 Km/h. The duration time of earthquake-related TEC anomaly was estimated at least 5 minutes. The duration time of TEC anomaly might correlate with the damping of ionospheric plasma. The anomalous fluctuation could be an early warning for far regions when this anomalous fluctuation beginning to propagate. The tsunami arrived at the far regions very slower than such anomalous fluctuation when the tsunami was caused by earthquake with epicenter in the sea (Liu *et al.*, 2011). Afraimovich *et al.* (2001) researched shock acoustic wave due to occurring of the earthquakes to affect ionosphere. They studied the earthquake effects in Turkey on 17 August and 12 November 1999 and in Southern Sumatra on 04 June 2000 and found the ionospheric response related to the earthquakes due to shock acoustic wave is 180-390 s. Compared with the result of this study, 2DPCA has shown its advantage and credibility to estimate the duration time of earthquake-related TEC anomaly.

### Conclusion

2DPCA had the advantage to detect the TEC anomaly related to the 24, May 2014 Aegean-Sea Earthquake. Results have shown that a local ranging TEC anomaly was detectable at the time 09:30 to 09:35 UT. The earthquake-related TEC anomaly could be indicative of a rising high speed acoustic shock wave with the speed of at least 1818.18 Km/h. m/s and might cause a TEC anomalous fluctuation e.g. density variance. The duration time of the TEC anomaly was at least 5 minutes. The anomalous fluctuation could be an early warning for far regions when this anomalous fluctuation propagating.

### Acknowledgements

The author is grateful to: NASA Global Differential GPS system (GDGPS) for their useful references Data.

### References

Afraimovich E.L., Perevalova N.P., Plotnikov A.V., Uralov A.M., 2001, The shock-acoustic waves generated by earthquakes. *Annales Geophysicae*, 19, 395-409.

Artru J., Lognonné P., 2001, Normal modeling of post-seismic ionospheric oscillations. *Geophysical Research Letter*, 28, 4, 697-700.

Chen K., Gao Y., 2005, Real-Time Precise Point Positioning Using Single Frequency Data. ION GNSS 2005, Long Beach, CA, USA, Sept.2005.

Elsner J.B., Kavlakov S.P., 2001, Hurricane intensity changes associated with geomagnetic variation. *Atmospheric Science Letters* (2001). doi:10.1006/asle.2001.0040.

Földiák P., 1989, Adaptive Network for Optimal Linear Feature Extraction, Int. Joint Conf. on Neural Networks, Washington, DC, I, 401.

Freund F., 2000, Time-resolved study of charge generation and propagation in igneous rocks. *Journal of Geophysical Research*, 105, 11001-11019.

Freund F.T., 2003, Rocks That Crackle and Sparkle and Glow Strange Pre-Earthquake Phenomena. *Journal of Scientific Exploration*, 17, 1, 37-71.

Fukunnaga K., 1991, Introduction to statistical pattern recognition. Academic Press 38-40.

Gao Y., Chen K., 2006, Development of a Real-Time Single-Frequency Precise Point Positioning System and Test Results. ION GNSS 19<sup>th</sup> International Technical Meeting of Satellite Division, 26-29 September 2006, Fort Worth, TX.

Garcia R., Crespon F., Ducic V., Lognonné P., 2005, Three-dimensional ionospheric tomography of post-seismic perturbations produced by the Denali earthquake from GPS data. *Geophys. J. Int.* 163, 1049-1064.

Jeong D.H., Ziemkiewicz C., Ribarsky W., Chang R., 2009, Understanding Principal Component Analysis Using a Visual Analytics Tool. Charlotte Visualization Center, UNC Charlotte.

Hamilton D.C., G. Gloeckler, Ipavich F.M., Studemann W., Wilken B., Kremser G., 1986, Ring current development during the great geomagnetic storm of February. *J. Geophys. Res.*, 93, 14343.

Hegai V.V., Kim V.P., Nikiforova L.I., 1997, A possible generation mechanism of acoustic-

- gravity waves in the ionosphere before strong earthquakes. *J. Earthquake Predict. Res.*, 6, 584-589.
- Hegai V.V., Kim V.P., Liu J.Y., 2006, The ionospheric effect of atmospheric gravity waves excited prior to strong earthquake. *Advances in Space Research*, 37, 653-659.
- Hernández-Pajares M., Juan J.M., Sanz J., Orus R., Garcia-Rigo A., Feltens J., Komjathy A., Schaer S.C., Krankowski A., 2009, The IGS VTEC maps: a reliable source of ionospheric information since 1998. *J. Geod.*, 83:263-275. DOI 10.1007/s00190-008-0266-1.
- Hobara Y., Parrot M., 2005, Ionospheric perturbations linked to a very powerful seismic event. *Journal of Atmospheric and Solar-Terrestrial Physics*, 67, 677-685.
- Jin S., Zhu W., Afraimovich E., 2010, Co-seismic ionospheric and deformation signals on the 2008 magnitude 8.0 Wenchuan Earthquake from GPS observations. *International Journal of Remote Sensing*. 31, 13, p. 3535 - 3543.
- Kechine M., O., Tiberius C.C.J.M., van der Marel H., 2004, Real-time Kinematic Positioning with NASA's Global Differential GPS System. GNSS Conference, St. Petersburg, Russia.
- Konga H., Wang L., Teoh E.K., Li X., Wang J.G., Venkateswarlu R., 2005, Generalized 2D principal component analysis for face image representation and recognition. *Neural Networks*, 18, 585-594.
- Kramer M.A., 1991, Nonlinear Principal Component Analysis Using Autoassociative Neural Networks. *AIChe Journal*, 37, 2, 233-243.
- Lin J.W., 2010, Ionospheric total electron content (TEC) anomalies associated with earthquakes through Karhunen-Loève Transform (KLT). *Terrestrial, Atmospheric and Oceanic Sciences*, 21, pp. 253-265.
- Lin J.W., 2011, Use of principal component analysis in the identification of the spatial pattern of an ionospheric total electron content anomalies after China's May 12, 2008, M=7.9 Wenchuan earthquake. *Advances in Space Research*, 47-1983, 10.1016/j.asr.2011.01.013.
- Liperovsky V.A., Pokhotelov O.A., Liperovskaya E.V., Parrot M., Meister C.-V., Alimov O.A., 2000, Modification of sporadic E-layers caused by seismic activity. *Surveys in Geophys*, 21, 449-486.
- Liu J.Y., Chuo Y.J., Shan S.J., Tsai Y.B., Pulnests S.A., Yu S.B., 2004, Pre-earthquake ionospheric anomalies monitored by GPS TEC. *Annales Geophys.*, 22, 1585-1593.
- Liu J.Y., Chen Y.I., Chuo Y.J., Chen C.S., 2006, A statistical investigation of pre-earthquake ionospheric anomaly. *Journal of Geophysical Research*. 111, A05304, 10.1029/2005JA011333.
- Liu J.Y., Chen Y.I., Chen C.H., Liu C.Y., Chen C.Y., Nishihashi M., Li J.Z., Xia Y.Q., Oyama K.I., Hattori K., Lin C.H., 2009, Seismoionospheric GPS total electron content anomalies observed before the 12 May 2008 Mw=7.9 Wenchuan Earthquake. *Journal of Geophysical Research*, 114, doi: 10.1029/2008JA013698.
- Liu J.Y., Chen C.H., Lin C.H., Tsai H.F., Chen C.H., Kamogawa M., 2011, Ionospheric disturbances triggered by the 11 March 2011 M9.0 Tohoku earthquake, *J. Geophys. Res.*, 116, A06319, doi: 10.1029/2011JA016761.
- Lognonné P., Artru J., Garcia R., Crespon F., Ducic V., Jeansou E., Occhipinti G., Helbert J., Moreaux G., Godet P.E., 2006, Ground-based GPS imaging of ionospheric post-seismic signal. *Planetary and Space Science*, 54, 528-540.
- Marchand R., Berthelier J.J., 2008, Simple model for post seismic ionospheric disturbances above an earthquake epicentre and along connecting magnetic field lines. *Nat. Hazards Earth Syst. Sci.*, 8, 1341-1347, 2008.
- Molchanov O.A., Hayakawa M., 1998, Subionospheric VLF signal perturbations possibly related to earthquakes. *Journal of Geophysical Research*, 103, 8, 17489-17504, 1998.
- Mukherjee G.K., 1999, Storm-associated Variations of [OI] 630.0 nm Emissions from Low Latitudes. *Terrestrial. Atmospheric. Oceanic. Sciences*, 10, 1, 265-276.
- Ondoh T., Hayakawa M., 1999, Anomalous Occurrence of Sporadic E-layers before the Hyogoken-Nanbu Earthquake, M 7.2 of January 17, 1995. In: Hayakawa M. (Ed.), *Atmospheric and Ionospheric Electromagnetic Phenomena Associated with Earthquakes*. TERRAPUB, Tokyo, 629-640.

- Ouyang G., Wang J., Wang J., Cole D., 2008, Analysis on Temporal-Spatial Variations of Australian TEC. *International Association of Geodesy Symposia*, 2008, 133, 4, 751-758, DOI: 10.1007/978-3-540-85426-5\_86.
- Pulinets S.A., Khagai V.V., Boyarchuk K.A., Lomonosov A.M., 1998, Atmospheric electric field as a source of ionospheric variability. *Physics-Uspekhi*, 41, 515-522.
- Pulinets S.A., Boyarchuk K.A., Hegai V.V., Kim V.P., Lomonosov A.M., 2000, Quasielectrostatic model of atmosphere-thermosphere-ionosphere coupling, *Advances in Space Research.*, 26, 8, 1209– 1218.
- Pulinets S.A., Legen'ka A.D., 2003, Spatial-temporal characteristics of the large scale disturbances of electron concentration observed in the F-region of the ionosphere before strong earthquakes. *Cosmic Res.*, 41, 221-229.
- Pulinets S., Boyarchuk K., 2004, *Ionospheric Precursors of Earthquakes*. Springer-Verlag, Berlin, Heidelberg.
- Pulinets S.A., 2004, *Ionospheric Precursors of Earthquakes; Recent Advances in Theory and Practical Applications*. *Terrestrial. Atmospheric. Oceanic. Sciences*, 15, 3, 413-435.
- Pulinets S.A., Kotsarenko N., Ciruolo L., Pulinets I.A., 2007, Special case of ionospheric day-to-day variability associated with earthquake preparation. *Advances in Space Research*, 39, 5, 970-977.
- Rumelhart D.E., Hinton G.E., Williams R.J., 1986, "Learning Internal Representations by Error Propagation," *Parallel Distributed Processing*, 1, D. E. Rumelhart and J. L. McClelland, eds., MIT Press, Cambridge, MA.
- Sanguansat P, 2012, *Principal Component Analysis*, Published by InTech, Janeza Trdine 9, 51000 Rijeka, Croatia. 300pp.
- Singh R.P., Mehdi W., Gautam R., Senthil Kumar J., Zlotnick J., Kafatos M., 2010, Precursory signals using satellite and ground data associated with the Wenchuan Earthquake of 12 May 2008. *International Journal of Remote Sensing.*, 31, 13, p.3341-3354.
- Yang J., Zhang D., Frangi A.F., Yang J.Y., 2004, Two-dimensional PCA: a new approach to appearance-based face representation and recognition. *IEEE Transactions on Pattern analysis and Machine Intelligence*, 26, No. 1, pp.131-137.
- Zhao B., Yu T., Wang M., Wan W., Lei J., Liu L., Ning B., 2008, Is an unusual large enhancement of ionospheric electron density linked with the 2008 great Wenchuan earthquake? *Journal of Geophysical Research*, 113, A11304, doi: 10.1029/2008JA013613